EPFL

Thèse n° 8885

Microfabricated nanomotion detectors for rapid cells viability tests

Présentée le 10 décembre 2021

Faculté des sciences et techniques de l'ingénieur
Laboratoire de microsystèmes 1
Programme doctoral en microsystèmes et microélectronique

pour l'obtention du grade de Docteur ès Sciences

par

Anton MALOVICHKO

Acceptée sur proposition du jury

Prof. L. G. Villanueva Torrijo, président du jury
Dr G. Boero, Dr S. Kasas, directeurs de thèse
Prof. T. Zambelli, rapporteur
Prof. R. Willaert, rapporteur
Prof. A. Radenovic, rapporteuse

École
polytechnique
fédérale
de Lausanne

2021

What sense would there be in buying a car so you could drive on pavement? Where there is asphalt, there is nothing of interest, and where it's interesting — there is no asphalt.
— *Arkady and Boris Strugatsky, Russian sci-fi writers.*

To my family and friends...

Acknowledgements

First of all, I would like to express my gratitude to Prof. Giovanni Dietler, Dr. Giovanni Boero and Dr. Sandor Kasas for their kind guidance during all 4 years of my PhD study. They were always open for discussions, and passionate to give me new ideas.
I also would like to acknowledge help and support that I've received from my colleagues and friends, with whom I was lucky to work in the same lab for a long time: Anne-Céline, Kamila, Zeno, Jiangtao, Inés, Sergey, Sasha, Leonardo, Veronika, Petar, Wojtec, Raphael. They've been giving me plenty of precious advises, both in the research and in the personal life. During my PhD studies I had a chance to be a part of two groups: The Laboratory of Physics of Living Matter for first 3 years, and The Laboratory of Biological Electron Microscopy for the last year of my PhD. I would like to thank all the past and current colleagues from both groups for always being friendly and supportive.
I would like also express my gratitude to Mireille for a lot of help in various administrative issues, Prof. Henning Stahlberg for giving me an opportunity to continue my project, creating a nice atmosphere, and providing a great coffee-machine that gave all of us more energy.
Many thanks and appreciation goes to Raymond, Nicolas and other people from the electronic workshop for the help with an amplification board, and Florian, Alain and other members of the mechanical workshop for manufacturing many things for my experimental setup. I also would like to thank Florent and Aubry for the help with computers, and Caroline for the help in preparation medium solutions and agar plates.
I would like to extend my appreciation also to all the CMi clean room staff, in particular to Julien, Cyrille, Joffrey and Kaspar. They helped me a lot during my work on the microfabrication of the chips, by participating in numerous discussions, sharing their expertise and giving me a training on all sorts of the clean room equipment.
Finally, I would like to thank my siblings Vanya and Galya, and my parents for the ultimate support, for giving me the inspiration and believing in me.

Lausanne, August 30, 2021 Anton

Abstract

The widespread use of antibiotics and antifungal drugs has provoked an increasing number of multi-resistant bacteria and fungi. The emergence of multiresistance to antibiotics has been now recognized as a very serious public health issue. In order to target infections with the appropriate antibiotics as soon as possible, there is an urgent need of rapid diagnostic tools. Presently, the conventional antimicrobial testing techniques require between 24 h and one month depending on the replication speed of the microorganism, which leads to the use of broad-spectrum antibiotics treatments and further favors the development of resistant pathogens.

This thesis proposes a rapid nanomechanical sensing-based diagnostic technique for studying the viability of living organisms. This instrument is a nanomechanical sensor borrowed from the Atomic Force Microscopy – based technology that uses a SU-8 lever as an optical fiber. This combination is a promising approach for further integration and miniaturization of the diagnostic apparatus. This thesis shows a first use of the microfabricated optomechanical sensors for monitoring activity of living cells.
Its working principle is the following. The organism of interest is attached onto a cantilever and its nanoscale movements induce the oscillations of the cantilever. To detect the oscillations, a laser light is coupled into the SU-8 structure and travels to the free end of the cantilever. The displacement of the output light spot induced by the oscillations of the cantilever is recorded with a camera or a 4-quadrants photodiode. This allows to monitor the viability of the microorganisms, that were previously attached to the cantilever surface.

The first part of this thesis briefly introduces the basic operating principle of the Atomic Force Microscope, discusses the importance of the problem of the antimicrobial resistance as one of the major health threats, and lists available alternative solutions to fight the resistance. Then the state of the art, working principle, applications of the nanomechanical antimicrobial sensors, and optomechanical mass sensors are discussed.
The second chapter introduces the methods for calculating the mechanical properties of the cantilever beams, as well as discusses the fundamental sources of the noise in nanomotion detectors, that limits their sensitivity. This chapter also includes calculations and finite-elements simulations of the mechanical properties of SU-8 - based cantilevers, as well as estimations of the electronic and thermal noise of the system.
Third chapter explains in details the proposed sensing devices and elaborates on its design and different strategies for the microfabrication of SU-8 - based optomechanical sensors.

It also describes the developed experimental setup for optomechanical measurements, the light-coupling procedure and data acquisition.
The fourth chapter reports the optomechanical measurements conducted by actuating a nanomechanical motion of the cantilever chips, and describes the preparation of the yeast cells and cantilevers for the nanomotion experiments. Subsequently, the results of the viability test are presented, along with a discussion of the mechanical and optical origins of it.
Finally, the thesis ends with a conclusion of this work and outlook of the presented results.

Keywords: antimicrobial resistance, AMR, antimicrobial susceptibility testing, AST, nanomotion, microfabrication, cantilever, SU-8, optomechanical sensing

Résumé

L'utilisation généralisée d'antibiotiques et de médicaments antifongiques a provoqué l'apparition d'un nombre croissant de bactéries et de champignons multirésistants. Cette émergence de variants multirésistants aux antibiotiques est aujourd'hui reconnue comme un problème de santé publique majeur. Une des manières d'en limiter la propagation est l'utilisation d'outils de diagnostic rapide. Actuellement, les techniques conventionnelles de test antimicrobien nécessitent entre 24 h et un mois selon la vitesse de réplication du micro-organisme, ce qui conduit à l'utilisation de traitements antibiotiques à large spectre et favorise le développement de pathogènes résistants.

Cette thèse décrit la fabrication et la mise en service d'un détecteur nanomécanique destiné à l'étude de la viabilité des organismes vivants. Il s'agit d'un instrument basé sur la microscopie à force atomique qui utilise un levier en SU-8 en guise de détecteur et de fibre optique. Cette combinaison est une approche prometteuse pour une intégration et une miniaturisation plus poussées de l'appareil.
Son principe de fonctionnement est le suivant. L'organisme d'intérêt est fixé sur un levier et les mouvements de l'organisme engendrent des oscillations du levier. Pour détecter ces oscillations, une lumière laser est couplée dans la structure SU-8 et quitte cette dernière à l'extrémité libre du levier. Le déplacement du spot lumineux de sortie est enregistré avec une caméra ou une photodiode à 4 quadrants.

La première partie de la thèse présente brièvement le principe de fonctionnement de base du microscope à force atomique, discute l'importance du problème de la résistance aux antimicrobiens comme l'une des menaces majeures pour la santé, et répertorie les solutions alternatives disponibles pour lutter contre elle. Ensuite, l'état de l'art, le principe de fonctionnement, les applications des capteurs antimicrobiens nanomécaniques et des capteurs de masse optomécaniques sont discutés.
Le deuxième chapitre présente les méthodes de calcul des propriétés mécaniques des leviers, ainsi que les sources fondamentales du bruit dans les détecteurs de nanomouvement, qui limitent leur sensibilité. Ce chapitre comprend également des calculs et des simulations par éléments finis des propriétés mécaniques des leviers à base de SU-8, ainsi que des estimations du bruit électronique et thermique du système.
Le troisième chapitre explique en détail les dispositifs de détection et élabore différentes stratégies pour la microfabrication de capteurs optomécaniques à base de SU-8. Il décrit également le montage expérimental développé pour les mesures optomécaniques, la procédure

de couplage de la lumière et l'acquisition de données.
Le quatrième chapitre rapporte les mesures optomécaniques et décrit la préparation des cellules de levure et des leviers pour les expériences de nanomouvement. Par la suite, les résultats des tests de viabilité sont présentés, ainsi qu'une discussion sur les origines mécaniques et optiques de celui-ci.
Enfin, la thèse se termine par une conclusion de ce travail et des perspectives qui en résultent.

Mots-clés : résistance aux antimicrobiens, nanomotion, microfabrication, levier, SU-8, détection optomécanique

Contents

List of Figures

List of abbreviations and definitions

AFM	Atomic Force Microscopy
STM	Scanning Tunnel Microscopy
GA	Glutaraldehyde
ConA	Concanavalin A
APTES	(3-Aminopropyl)triethoxysilane
PBS	Phosphate-buffered saline
YPD	Yeast extract peptone dextrose medium
DI water	Deionized water
LB	Lysogeny broth medium
S. pombe	*Schizosaccharomyces pombe*
E. coli	*Escherichia coli*
FFT	Fast Fourier transform
FEM	Finite element method
PMMA	Poly (methyl methacrylate)
AST	Antibiotic susceptibility testing
AMR	Antimicrobial resistance
RMS	Root mean square
SD	Standard deviation
MAD	Median absolute deviation
PSD	Power spectral density
PGMEA	Propylene glycol methyl ether acetate
HMDS	Hexamethyldisilazane
ICP	Inductive-coupled plasma
SEM	Scanning electron microscopy
CCD camera	Charge-coupled device camera
PCB	Printed circuit board
$\boldsymbol{Re}$	Reynolds number
$\boldsymbol{\Gamma(\omega)}$	Hydrodynamical function

1 State of art of micro-organism nanomechanical biosensors

1.1 Introduction

1.1.1 Atomic Force Microscopy

In 1981, Binning and Rohrer developed the Scanning Tunneling Microscope (STM) at IBM Zurich. The STM allowed the determination of the 3-dimensional topography of the surface of conducting samples with a high lateral and vertical resolution. The principle is based on approaching a conducting sharp tip to the conducting sample's surface and in measuring the tunneling current traversing the vacuum gap (of the order of few Ångström) between tip and sample. Due to the exponential dependence of the tunneling current upon the gap size, it was possible to "image" atoms at the sample's surface. Metals and semiconductors were the first materials studied with this new technique. For scanning the surface, the tip is moved at the same distance from the surface, while recording the tunneling current in each point of the surface. Or by keeping a constant tunneling current in the feedback loop, the tip moved in a way that it reproduces the topography of the sample while in vicinity to it. This technique, however, requires conductive tips and samples.

In 1986, Binning and Rohrer received the Nobel prize for this invention. The Nobel prize actually rewarded the consequences of this invention, namely the STM had shown that now, matter could be studied at the atom level. Moreover, it was shown that atoms could be manipulated with the STM. The STM and the possibility to study and manipulate matter at the atom level has strongly influenced physics, chemistry and biology. Nowadays we talk of nanosciences. In fact, the STM has opened a new window for the study of matter. In 1986, Binning, Gerber and Quate [Binnig et al., 1986] developed what is today known as the Atomic Force Microscope (AFM). Already in their original work in 1986, AFM had a 30 Å lateral resolution and less than 1 Å vertical resolution, with an ability to sense forces as small as 10^{-18} N [Binnig et al., 1986]. The AFM belongs to the family of scanning probe microscopes, and is based on the earlier invented scanning tunnel microscope (STM). Both microscopes are 'blind' instruments, that scan the sample with a fine tip to characterize its topography (similarly to a blind person scanning the surroundings with a cane).

Atomic Force Microscopy similarly to STM is a sample scanning technique, but has the advantage that it can study non-conductive samples. Instead of a sharp conductive needle, it uses a so-called cantilever chip, that consists of a free-standing beam and a sharp tip at its end (see Fig. 1.1). When this flexible beam is driven into oscillation, and it is approached very close to the sample's surface, the van der Waals inter-atomic forces between the cantilever tip and sample surface become strong enough to cause a detectable frequency shift, a change of oscillation amplitude and of phase. Essentially, these forces cause the bending of the beam, that is detected by the optical set-up of the AFM. The optical detection of the cantilever's bending comprises a laser (focused on the metal-coated cantilever surface) and a position-sensitive photodetector that senses the reflected laser beam. Therefore, a bending of the cantilever causes the displacement of the light spot at the photodetector, which is then detected by recording the amplified photodetector currents.

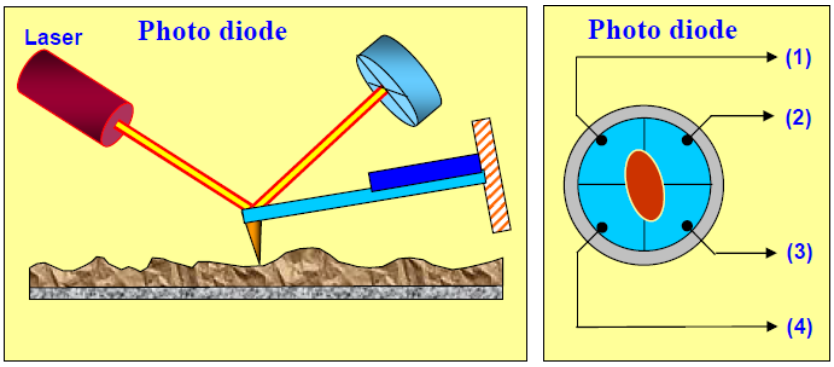

Figure 1.1: Schematic description of the optical system to detect the cantilever's bending [Mironov, 2004].

The vertical displacement of the cantilever position will be proportional to the photocurrent difference of the quadrant detector ([Mironov, 2004], Fig. 1.1):

$$\triangle I_Z = (I_1 + I_2) - (I_3 + I_4), \tag{1.1}$$

where I_i is a differential current of the i segment. Usually $\triangle I_Z$ is normalized over the total photocurrent $I_{tot} = I_1 + I_2 + I_3 + I_4$. In addition to this classical optical lever scheme, there were proposed also other readout methods, such as piezoelectric [Lee et al., 1996] and piezoresistive detection [Tortonese et al., 1993; Giessibl and Trafas, 1994], laser Doppler vibrometry [Nishida et al., 2008], and optical interferometry [Rugar et al., 1989]. Also, many different modes of scanning were developed, that allow to study not only topography, but also electrical, magnetic and mechanical properties of the samples.
However, the application of the cantilever - based devices is not limited to imaging the samples surface or mapping its other properties. Since behavior of the free-standing beams strongly depends from their mechanical properties, they can be used as very sensitive mass sensors and be employed for measurements of forces and nanoscale motion. These applications are discussed in details in the next chapter.

1.1.2 Antimicrobial resistance of micro-organisms and viability testing

Overuse and misuse of the antibiotic and antifungal drugs over the last years led to a dramatic increase of the drug-resistant bacteria and yeast [Wiederhold, 2017; Livermore, 2004; The IACG on Antimicrobial Resistance, 2019; Cassini et al., 2019; Department of Health and Human Services CDC, 2019], including some of the organisms that are resistant to multiple drugs. The appearance of new infectious pathogens, that can not be treated by any of the commonly used drugs [Livermore, 2004] became one of the major health concerns. As an example, according to the reports of CDC and ECDC of 2019, in USA, more than 2.8 million antibiotic-resistant infections occur each year and more than 35,000 people die as a result [Department of Health and Human Services CDC, 2019], and in Europe more than 670,000 infections occur, taking lives of 33,000 people yearly [Cassini et al., 2019; European Centre for Disease Prevention and Control, 2020]. According to the Interagency Coordination Group on Antimicrobial Resistance report, worldwide the drug resistance causes 700,000 deaths yearly, and if no action is taken, the number of death in the world could reach a number of 10 million per year by 2050 [The IACG on Antimicrobial Resistance, 2019].
It was estimated that the use of rapid diagnostic tests, together with enhanced hygiene, and correct use of the antibiotic treatment could prevent up to 27,000 death in Europe per year [European Centre for Disease Prevention and Control, 2020].

A big contribution to the increase of the drug-resistance is due to wide-range antibiotics use, or wrongly selected drugs, when an appropriate antibiotic or antifungal drug could be selected. And as a consequence, the number of the available drugs, that could be used against these micro-organisms is reduced. The development of new drugs can take longer time than the mutation rate of the pathogens [Bassetti et al., 2013], leading to delay between effective and less effective drugs. This is why having a rapid and reliable diagnostic technique is extremely important to fight the antimicrobial resistance.

Let us consider the viability tests for antibiotic screening more in detail. The clinical flow consists of a bacterial identification step and of antibiotic susceptibility testing (AST) [Dinarelli et al., 2017]. During the last 20 years, the bacterial identification has been revolutionized, and it is now a reliable, automated, high-throughput technique. The second step of the flow is the susceptibility test. The commonly used techniques for these tests are simple, reliable and robust, but can be very slow. This is because the conventional techniques rely on the growth of the micro-organisms. Depending on the considered species, it can require days or even weeks to get a result. Meanwhile, novel rapid AST techniques could help to make a correct diagnosis in just few hours [Dinarelli et al., 2017].

The AST techniques can be divided into several types: molecular techniques, phenotypic growth techniques, novel photonic methods, and nanomechanical sensors. Real-time PCR [Didelot et al., 2012] and DNA microarrays [Frye et al., 2006] are promising examples of molecular techniques, that rely on the genetic footprints. They are fast and highly reliable, but relatively expensive and require identification of the specific genetic fragment; also, they are

unable to distinguish dead and alive bacteria. The molecular techniques also require that the resistance mutation is know in advance. The phenotypic methods are the most commonly used in the hospitals. They are based on the growth of the bacteria, and as described earlier, they can be slow. However, there are some advances in using automated phenotypic systems and image recognition [Cantón et al., 2000], that allow to speed-up these tests. There is a big variety of promising novel photonic techniques, that could be used to make miniaturized and automated devices. Some of the examples of such techniques are tracking single bacterial cells with plasmonic imaging with sub-nm precision [Syal et al., 2016], AST of bacterial network on micropillars using intrinsic phase shift spectroscopy [Leonard et al., 2017], and plasmonic nanohole array sensors [Kee et al., 2013]. And finally, nanomechanical sensors are based on monitoring behavior of the free-standing microstructures, such as AFM cantilevers. The bacteria are attached to the cantilever beams, and the change of various characteristics of the cantilever beams can be detected: resonance shift, static deflection, and dynamic oscillation. The latter mode is the most interesting for rapid AST: the observed fluctuations can be attributed to the activity of the living micro-organisms, and the oscillations are reduced when the specific drug is introduced in the system with cantilever (Fig. 1.2). These precise and compact devices can be used for a large variety of the microorganisms, including bacteria [Kasas et al., 2015], yeast [Kasas et al., 2015; Kohler et al., 2020; Longo et al., 2013; Mertens et al., 2019; Lissandrello et al., 2014], bacteria from blood culture pellets [Stupar et al., 2017], cancer cells [Stupar et al., 2021]. Recently a nice combination of the optical light guiding with a

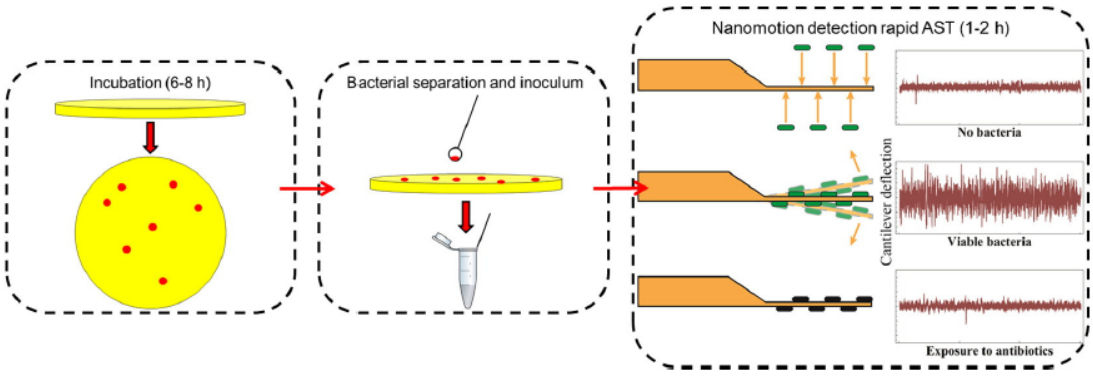

Figure 1.2: Schematics of a typical nanomotion experiment. The protocol starts from the incubation step, left panel, and ends at the AST performed using the cantilever sensor, right panel [Dinarelli et al., 2017].

cantilever devices in a number of works was demonstrated (Fig. 1.3), that is very promising for having a miniaturized, integrated and multiplex devices [Alvarez and Lechuga, 2010; Estevez et al., 2012; Zinoviev et al., 2006a; Nordström et al., 2007; Xu et al., 2005; Zinoviev et al., 2007; Xu et al., 2004]. In these nanomechanical sensors, light travels through the oscillating cantilever beam, and then is collected at the other side. Most of the works till now, however, exploit the mass sensing and detection of the analytes attachment to the cantilever, based on resonance shift or static deflection.

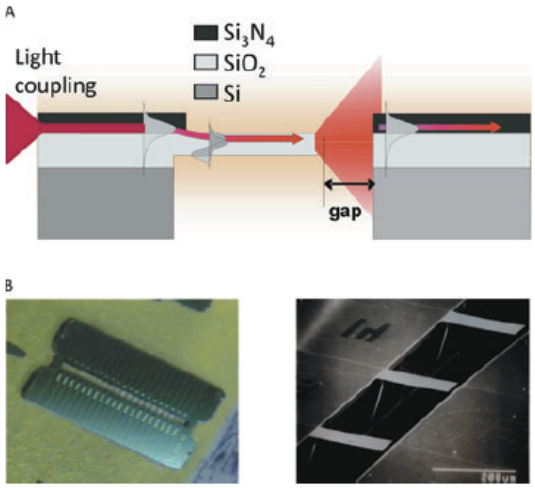

Figure 1.3: (A) Schematics of the optical waveguide cantilever working principle, (B) Photographic image and SEM of a cantilever - waveguide array that consist from 20 cantilevers [Alvarez and Lechuga, 2010; Estevez et al., 2012].

1.1.3 Thesis objectives

This thesis proposes a rapid diagnostic device, that is based on the optical cantilevers, working in the dynamic mode, similar to the conventional AFM nanomotion sensors. A significant part of the thesis is devoted to the designing and fabrication of the micromechanical SU-8 polymer based sensors, and to developing and assembling dedicated experimental setup to make optomechanical measurements. The overview of this setup is presented at the Fig 1.4. Laser light is focused on the entrance of the light guiding part of SU-8, and exits it at the end of the free-standing beam. Then light hits the sensing area of a 4-segment photodetector. Readout signal is then amplified and recorded with a data acquisition board, and undergoes required signal analysis and processing. A number of challenges had to be solved, to optimize the microfabrication process flow, and to assemble a setup that allows to make optomechanical measurements both in air and liquid.

Another important goal of this work was to characterize fabricated sensing chips, compare their mechanical characteristics with the theoretically calculated design values, and to demonstrate the ability of the device to sense oscillations, driven of an amplitude as low as few nm. The final task of this work was to establish an experimental flow for performing antimicrobial sensitivity tests, and to make nanomotion measurements with a test micro-organism. The antimicrobial tests are most relevant for testing susceptibility of the pathogenic bacteria. However, for demonstrating the proof-of-concept of the device, in this thesis *Schizosaccharomyces pombe* (*S. pombe*) yeast was selected as a test micro-organism. *S. pombe*, also called 'fission yeast' is a well-known model organism, used in molecular and cell biology. It is easy to handle, and it is safe to work with it in the standard (P1) biochemical laboratory. *S. pombe* also has a bigger size: 3 to 4 μm in diameter and 7 to 14 μm in length, in comparison to *Escherichia coli*

(*E. coli*) bacteria whose size is 0.5 μm in diameter and 1-2 μ in length. Therefore, it is easier to image *S. pombe* yeast with an optical microscope, and the nanomechanical sensor response is expected to be larger. In the future, the developed diagnostic device can be used for detecting viability of the smaller micro-organisms too. The working principle of nanomotion sensor, its applications and limitations are discussed in more detail further.

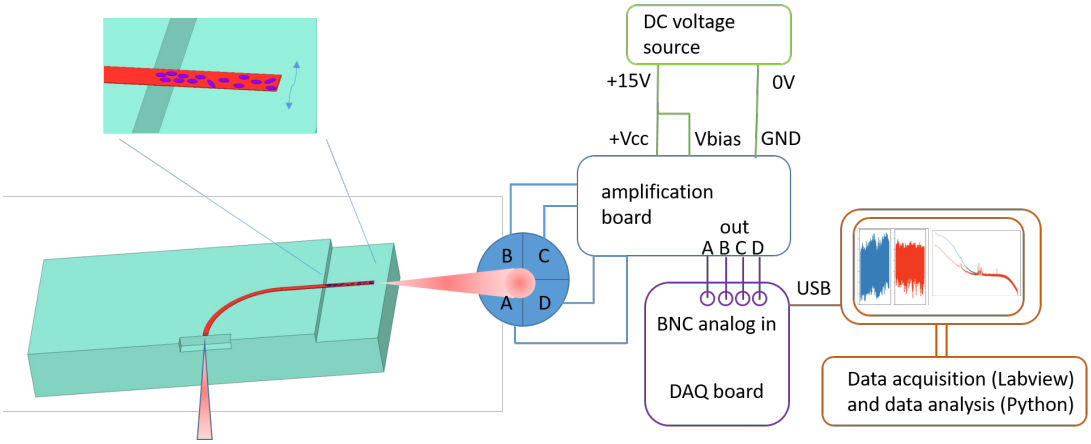

Figure 1.4: Schematics of the proposed optical cantilever diagnostic device. Laser light is focused on the entrance of SU-8 polymer, travels through the curvature and reaches the free-standing end of the SU-8 structure. Displacement of the output light spot can be detected by CCD camera or segment photodetector.

1.2 Cantilever-based nanomechanical biosensors

1.2.1 Mass detection and resonance shift

One of the popular use of cantilever sensors is a precise detection of the attached living organisms, proteins, or other biological species by monitoring the frequency shift of the cantilever's resonance. However, the use of these methods in a liquid medium, that is necessary to keep the living organisms viable, has some challenges. The resonance frequency of the beams immersed into a liquid medium is shifting towards lower value, but due to the damping effects, the quality factor is significantly reduced. During the experimental detection of living organisms by nanomotion detection, the shape of resonance does not change since the properties of the liquid such as density and viscosity are the dominant properties. But the attachment of living organisms to the cantilever surface changes the effective mass of the beam, resulting in a slight shift of the resonance peak. Though, the precise detection of the resonance peak in viscous medium can be difficult due to the low quality factor, a number of authors describe measuring the mass of the attached organisms by detecting the resonance shift of the cantilevers in air (after drying droplets of solutions with organisms such as bacteria or yeast cells in it) [Ilic et al., 2001a; Ramos et al., 2007]. This approach can help to measure mass with such high precision, that even a single *E. coli* bacteria can be detected [Ilic et al., 2001a]. However,

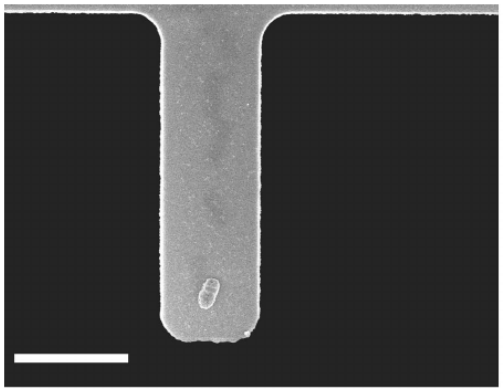

Figure 1.5: Single *E. coli* bacteria attached to the beam surface [Ilic et al., 2001a]

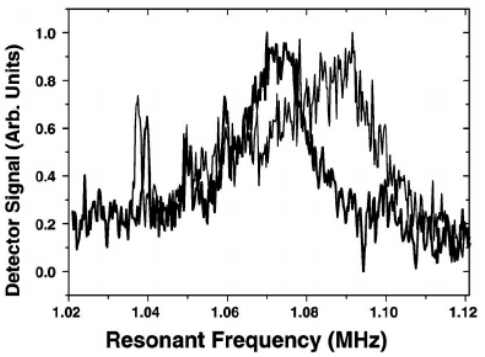

Figure 1.6: Frequency shift of the cantilever with a single bacteria on a beam [Ilic et al., 2001a].

not only the added mass, but also the position, at which the attached organisms are located, can affect the value of the resonance shift. Also the bacteria's position relative to the nodes of the resonance mode matters [Ramos et al., 2007].
The other relevant point is that the position of the resonance peak does not bring any information about the viability of the attached organisms. On the other hand, it can confirm the quality of the surface functionalization, and be used, for example, to compare different protocols of the surface treatment, as an alternative to a simple imaging of the cantilever surface. Since the attachment might not always work in equally successful way, it can be useful to always have an idea of the surface coverage by monitoring the resonance frequency.

1.2.2 Nanomotion sensors

Although mass detection sensors can also give some information about the viability of the cells, since the cell death can be correlated with a damage of the cell walls, and as consequence detaching of the dead cells from the cantilever surface, resulting in resonance frequency shift, the dynamic nanomotion sensors seem much more interesting for the rapid microbial testing application. As it was described in the introduction, the main working principle of these sensors is monitoring the oscillations of the beam, that are affected by the activity of the microorganisms. In contrast to a conventional use of AFM microscope for scanning, or resonance shift techniques, which are focused on higher frequencies, near to the cantilever resonance, the dynamic nanomotion AST method is focused on studying the low frequency noise. The possible origins of it and its contributions to this noise are discussed further.

Noise of measuring system

The main sources of low frequency 1/f noise of the measuring system can be related to 1/f noise of electronics (operational amplifier) and noise of the light source. As it was reported ([Labuda et al., 2012]), in case of traditional AFM cantilevers, beams with metal coating show

significant 1/f noise due to fluctuations of the laser power. Meanwhile silicon beams without any metal coating can show a negligible 1/f noise. The readout system, used in this work is different, though it can also introduce noise caused by the laser: either by unstable intensity of the recorded light spot, or in the form of thermal noise. The heating effect is given by the laser illuminating not the beam surface, but the rigid part of SU-8 light guide.

Noise due to activity of biological organisms adhered to the beam surface and possible explanations of the effect

The noise caused by the bacteria was reported to be of the type $S(f) \propto 1/f^{\alpha}$ and typically is observed in the low frequency region: according to some works [Lissandrello et al., 2014] up to 80 Hz (see Fig. 1.7) , according to other works [Mertens et al., 2019] - up to 1 kHz (see Fig. 1.8). Although it is difficult to untangle 1/f noise sources, subtraction of the Power Spectral Density (PSD) of cantilever before bacteria adhesion from the one after, can remove the experimental 1/f noise related to the measuring setup. It was shown [Lissandrello et al., 2014] that this subtracted noise grows with the increase of the number of bacteria on the beam surface. Probably each bacteria exhibits motion with various time scales and amplitudes, resulting in producing $1/f^{\alpha}$ noise, where α could be given by the interplay between these timescales. However, this is even more complicate due to the random character of positions of the bacterial organisms on the beam surface, and each bacteria can have different contributions on the observed fluctuations. Probably, local micro-patterning of the bacterial cells on a small part of cantilever surface could give more explanation concerning the timescale of the process. But such patterning procedure can be a technological challenge. Lissandrello et. al suggest that reducing the spring constant and hence the resonance frequency that leads to overdamping, could be beneficial for having a stronger signal [Lissandrello et al., 2014]. The scaling exponent α in the $S(f) \propto 1/f^{\alpha}$ spectra of the beam, coated with active bacteria, is reported to have values $2 \leqslant \alpha \leqslant 3$ [Lissandrello et al., 2014] or $1.5 \leqslant \alpha \leqslant 2$ [Mertens et al., 2019], depending of the used setup and experimental protocol. Since $1/f^{\alpha}$ noise is clearly changing its slope due to motion and activity of the attached alive organisms, one of the characterization parameters could be the power α of this noise. It is well known that Atomic Force Microscopy can be used for the precise measurement of mass loading of very small species, such as single cells and proteins on the cantilever. Adsorption of the cells to the beam surface causes a resonance shift that is proportional to the effective mass. However, the low quality factor makes it difficult to monitor this for the cantilever beams immersed in a liquid medium in real time. Instead, the resonance curve can be measured in air or vacuum, when the quality factor is much higher, and comparison of the resonance frequency of bare beam and beam covered with cells, can give precise information about amount of the cells, and also give more understanding about the effect caused by these adsorbed species. Such, it was demonstrated, that the resonance shift can have different sign and value, depending on the position of the attached cells [Ramos et al., 2007; Ilic et al., 2001b]. There is an explanation for this. There are two different effects: added mass, that shifts resonance towards lower frequencies, and change of the effective flexural rigidity of the beam due to the bacteria stiffness, that shifts resonance towards the

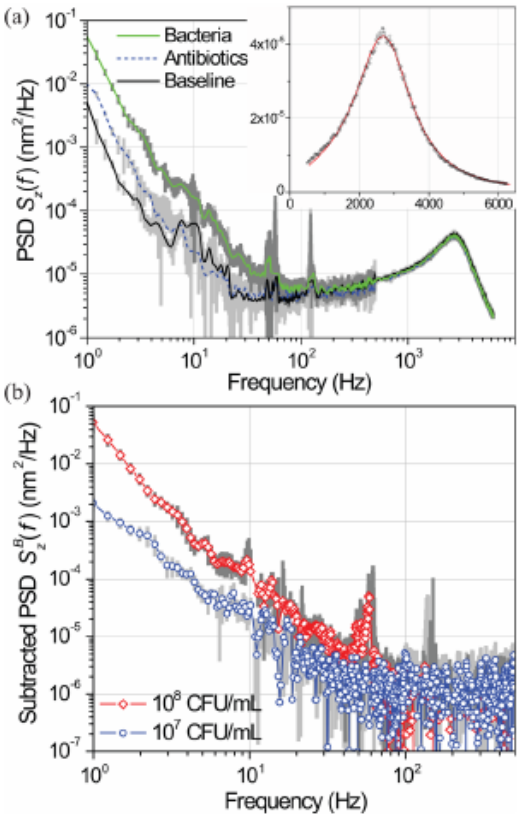

Figure 1.7: Power spectral density of cantilever fluctuations before bacteria attachment, after attachment of viable bacteria cells, and after introducing antibiotics in the system [Lissandrello et al., 2014].

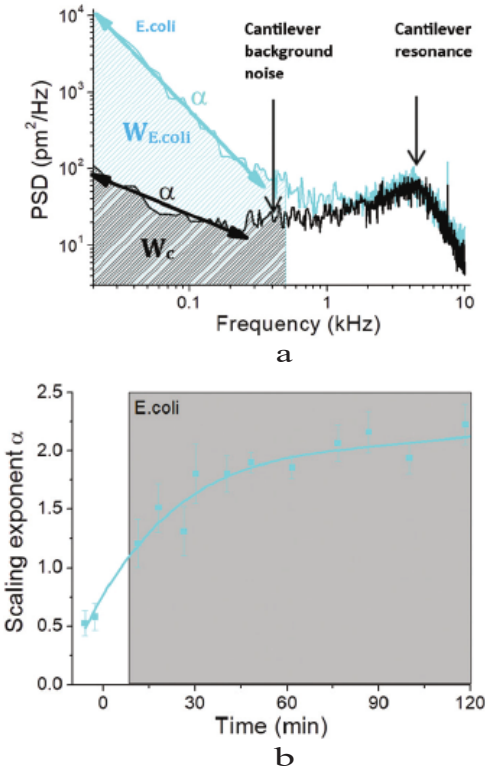

Figure 1.8: (a) Power spectral density of cantilever oscillations before the experiment (black) and after bacteria attachment (sky-blue) [Mertens et al., 2019]. (b) Scaling exponent α for a cantilever functionalized with E.coli at t=0 min [Mertens et al., 2019].

higher frequencies. The interplay between these two effects gives the resulting response to bacteria attachment [Ramos et al., 2007] .
However, there is a workaround of the low quality factor problem: to operate cantilever beam in air, but embed a microfluidic channel inside the beam. This allows monitoring the resonance frequency in real time. And the results of the measurements show that the resonance frequency not only give an idea about amount of organisms in the microfluidic channel, but also helps to distinguish viable and non-viable cells [Etayash et al., 2016]. This is an interesting approach, but requires the application of microfabrication techniques and clean room access to produce such chips with embedded microchannels, and a lot of care in operating the microchannels that should stay clog-free and bubble-free. The static deflection also shows adhesion of the organisms to the beam, if measured in real-time during the attachment step [Mertens et al., 2019; Etayash et al., 2016].

The nanomotion signal of the beams oscillation shows clear drop of the fluctuations, when a

drug is affecting the susceptible bacteria [Longo et al., 2013].
This change is observed mostly in the low-frequency range, up to few hundreds of Hz [Mertens et al., 2019; Lissandrello et al., 2014] , and is explained by the surface stress. However, since in the described experiments the whole beam is covered by bacteria cells, that are located on different spots, have a distribution of their sizes, and act at various characteristic timescales, it is difficult to make a model of the sensor response.
Nevertheless, there are some works that model surface stress caused by cells, using finite elements simulation [Imamura et al., 2016]. The deflection, caused by the activity of the attached cells, depends from the position of the cell on the beam and has higher values for the cells, attached close to the fixed end of the beams. In general deflection increases with the area covered with cells, if the position relatively to the fixed end is kept constant. But the cumulative effect depends from the phase of the cells, that can have positive phase in case of tensile stress, or negative in case of compressive stress. Therefore, some cells can cancel out the caused stress, but other cells, that synchronize their motion, amplify the sensor response. This simulation suggests that resulting response can be considered as a degree of collectiveness of the cell motion. However, only situation with coverage of the top side of the beam was considered and usually both sides are being covered with organisms during the incubation step; it remains unclear, what is the interplay between effect that is caused by cells, attached to the two sides of the beam.

1.3 SU-8 cantilevers: experimental characterization of the beams in the literature

The reported [Nordstrom, 2004] resonance frequency in water is typically several times lower than the resonance frequency in air (that is very close to the resonance in vacuum) (see Fig. 1.10). The resonance shift of SU-8 beams with similar dimensions in the publications is in the agreement with the ones, estimated analytically and with finite element simulations in this thesis. (see Chapter 2)

Length (μm)	Width (μm)	Thickness (μm)	k (N/m)	f_{res}, vacuum (kHz)	f_{res}, air (kHz)	f_{res}, water (kHz)
200	20	1.6	0.013	14.5	14.4	4.3
200	20	2.4	0.043	21.8	21.7	7.8
100	20	1.6	0.101	58.1	57.7	17.3
100	20	2.4	0.342	87.2	86.8	31.0

Figure 1.9: Calculated resonance frequency for SU-8 beams of various dimensions (author used Sader's method in the inviscid approximation [Nordstrom, 2004]).

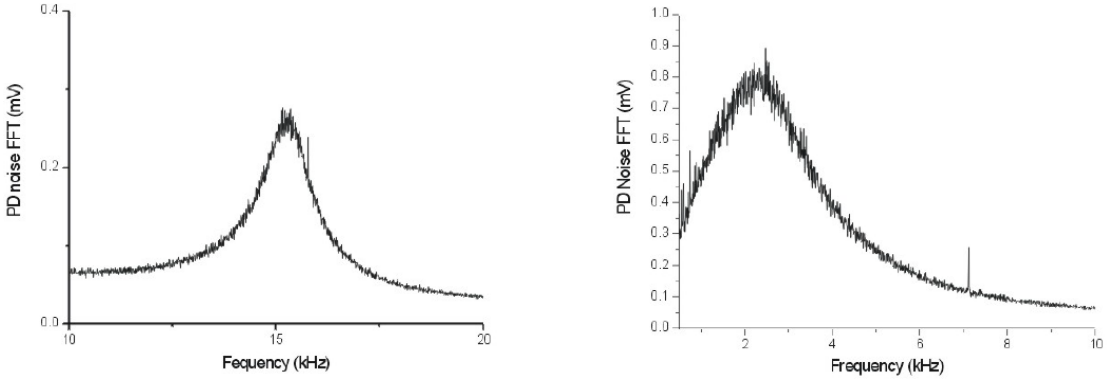

(a) (b)

Figure 1.10: Frequency spectra of SU-8 beam with dimensions $l = 200$ μm, $w = 20$ μm, $h = 1.6$ μm in (a) air: $f_{air} = 15.3$ kHz and (b) in water: $f_{water} = 2.3$ kHz [Nordstrom, 2004].

1.4 Measurement setup of the Atomic Force Microscopy-based nanomotion detectors

Typically, the experimental setup for nanomotion-based antibiotic sensitivity tests consist of Atomic Force Microscope (AFM), a microcantilever, a liquid cell, and a liquid exchange system. The use of an automatic liquid handling system helps to automatize the measurements, but requires additional care about the pumping rate, in order to avoid air bubbles in the tubes, leakage prevention, and other problems. This can be simplified by using a Petri dish as liquid cell, and manually pipetting instead of pumping liquids ([Longo et al., 2013; Stupar et al., 2017]).

Since the working principle of the described sensors is based on measuring cantilever noise without a need of excitation or approaching the sensor to any surface, the piezoscanner of AFM is not required, and a custom-made devices without scanner can be used, that simplifies the application of the technique.

The microfabrication of the custom designed cantilever sensors, instead of using the commercially available, allows to have the desired shape, surface patterning, and even to embed a microfluidic channel inside the cantilever [Etayash et al., 2016]. This interesting approach helps to overcome the limitation of viscous damping, since the cantilever is operated in the air, and the laminar flow with the sample is pumped inside the cantilever. Therefore such microsensor allows to measure the resonance shift due to the absorbed bacteria precisely in a very reproducible way. Also, this approach is a further step towards the miniaturization and integration of the sensing device.

At the same time, one can perform by fluorescent microscopy a test of the organisms viability in the microfluidic channel inside the cantilever [Etayash et al., 2016] , thanks to live/dead stains, that stain with one color all cells, and with another – only the ones with damaged cell membranes, i.e., dead cells. This also helps to estimate the coverage of the beam surface with the bacteria and confirm the efficiency of adhesion [Lissandrello et al., 2014; Mertens et al.,

2019]
Among an interesting additional characterization methods, there is also a combination of nanomechanical sensing with infrared spectroscopy measurements [Etayash et al., 2016]. The infrared radiation causes an additional cantilever deflection, and allows to measure the infrared absorption spectrum of the bacteria. This makes possible to determine different bacteria strains, distinguish injured and intact cells [Etayash et al., 2016]

1.5 Workflow of rapid bacteria viability tests

After culturing the chosen bacteria strains on the agar plate, the bacteria are placed for overnight growth into the liquid Luria–Bertani broth (LB) media at 37 C with shaking. In case of the yeast strains, the cells grow in Yeast Extract–Peptone–Dextrose (YPD) medium instead of LB. Then LB or YPD medium is replaced with Phosphate-buffered saline (PBS), that is washed 3 times with fresh solution. In order to maintain the desired concentration of the cells in the solution, the optical density is measured with a spectrophotometer. Meanwhile, the cantilever's surface is treated in order to improve the adhesion of the bacteria cells. Various ways to improve adhesion were described in the literature, such as using a APTES linker [Longo et al., 2013; Lissandrello et al., 2014; Stupar et al., 2017; Mertens et al., 2019]. The attachment of the bacteria cells to the pre-treated cantilever beam surface is performed by incubating the cantilever chip in a droplet of bacteria suspension typically for 15-30 min. Then the sensor is gently washed in LB solution, such that droplet is removed and only the well-attached cells remain on the surface. The cantilever is now ready for the measurement. Immediately after the cleaning step, the chip is placed in LB medium, so that cells have enough nutrients to stay viable. It is better to avoid having any bacteria that are loosely attached only by one side (dangling bacteria). The washing step is repeated if such cells are observed in the optical microscope.

The nanomechanical motion is typically recorded with an acquisition rate of 20-30 kHz, that is higher than the resonance frequency of the soft cantilevers in liquid, and much higher than frequency range at which there is the most prominent response of the sensor. The signal recording is done for at least 30 min, before introducing the specific drug to kill the susceptible organisms, and to continue the recording. Longer measurements up to few hours help to ensure that there is no slow drift causing a drop of the signal without injection of the drug, and also that the drug effect is complete. These measurements also allow to study if the system is in a stable state.
The optical imaging of the cantilever surface before and after the experiment helps to confirm that similar amount of cells as at the beginning adhere to the surface after the end of measurement.

1.6 Data analysis of the typical nanomotion experiments

To improve the signal-to-noise ratio, some pre-treatment of the signal should be performed. The linear drift can be compensated by a regression flattening. As response is expected in the low-frequency range, the low-pass filter can be useful to suppress effect of higher frequencies, known as aliasing effect. Also, some smoothing, such as moving averaging [Stupar et al., 2017] or Savitzkiy-Golay [Bennett et al., 2020]filter can be applied. The variance of the fluctuation is calculated over a time window, and allows to follow the dynamics of the organisms activity on the cantilever [Stupar et al., 2017]. The Fourier transform of the time-domain signal and power spectral density gives an understanding of the frequency range, at which response of the device is the highest. Considering only that frequency range improves the signal-to-noise ratio. Also, the resonance frequency can be determined from the power spectra and shift of it can be used for estimating the mass load, though it is complex because of low quality factor of the cantilever in the viscous medium.

Some single spikes can be removed from the time domain nanomotion signal, as they can be artifacts, not related to biological activity. Also, 50 Hz and 100 Hz can be filtered out as the ones related to electrical network. This can be important, since spikes, caused by e.g. short acoustic noise or accident touching of the device, can affect variance, and also the power spectra in the whole frequency range. In order to reduce noisiness of the visualization of the power spectra, a moving average filter can be applied to the spectra curve.
To analyze the effect of bacteria activity in the low-frequency range of the cantilever power spectra, and distinguish this from the low-frequency 1/f noise of the cantilever and measurement system itself, the power spectra of the bare cantilever should be subtracted from the power spectra of the cantilever coated with bacteria cells [Lissandrello et al., 2014]

1.7 Cantilevers with direct optical readout

1.7.1 SU-8 - based optical waveguides

SU-8 material has a good optical transmittance in a wide spectral range: higher than 90% in a range from 400 nm to 2500 nm wavelength, low light absorbance, and refractive index of $n \backsim 1.6$. Thank to these optical properties, this material is widely used as a core of optical waveguides. To have efficient confinement of light inside the waveguide by means of total internal reflection effect, a cladding layer with a lower refractive index is required. For the systems with SU-8 core material, various cladding materials can be used, such as SiO_2 [Koev et al., 2009] (n = 1.46 at 630 nm [Malitson, 1965]), SU-8 resist with finely tuned refractive index (having 1.5912 for the SU-8 core, and 1.5841 for SU-8 cladding, [Nordstrom et al., 2007]), or using air around suspended waveguide core as a cladding material [Marinins et al., 2016; Prokop et al., 2017, 2016].

The light coupling of light in and out of the waveguide can be facilitated by means of a specifically designed diffraction grating [Zinoviev et al., 2006b], or using a butt-coupling

technique [Nordström et al., 2007; Zinoviev et al., 2006c,a] by approaching a fiber source close to the waveguide end or simply focusing light on the cross-section of the waveguide end. Especially interesting for the mechanical sensing is the combination of the released free-standing structures (cantilever made out of SU-8 for example) with the light guiding techniques. Such, it was demonstrated that SU-8 material can serve simultaneously as a free-standing micromechanical oscillator, and as a lightguide. In this case, instead of the reflected laser readout scheme of AFM or piezoelectric readout, the oscillations can be monitored by direct recording the displacement of the output light spot of the suspended SU-8 beam, or by coupling light that exits from the cantilever with a static waveguide, and measuring the output power (see Fig. 1.11). It was also proposed a reversed optical readout scheme, where light is being coupled in the opposite direction: exits the static waveguide, and enters the free-standing beam. More details about the different set-up will be given in chapter 3.

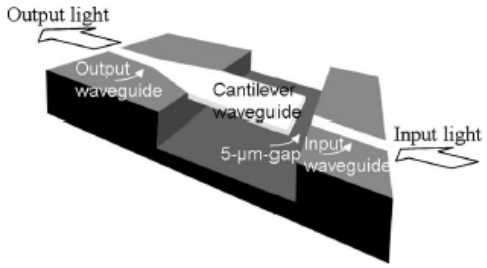

Figure 1.11: SU-8 cantilever sensor with an integrated optical readout of reverse direction: light enters the static waveguide, travel through gap, enters cantilever waveguide, and is collected at the other side of the chip [Nordstrom et al., 2007].

1.7.2 Mechanical sensing with suspended SU-8 light guides

The so-called optical cantilevers, or cantilevers that guide light through the beam, are especially promising for the multiplexed devices. It was demonstrated, that an array of such light guiding cantilever beam can be fabricated on the same chip [Xu et al., 2005; Hu et al., 2009; Zinoviev et al., 2006a; Li et al., 2009; Xu et al., 2004], and simultaneous or subsequent readout from all beams can be then recorded with a camera or photodetector. These novel readout schemes allow to have light-emitting diode and detector of the photonic cantilever integrated in the same device, which is very promising for creating highly integrated and miniaturized devices [Misiakos et al., 2009].
Typically, the device consists from the waveguide with free-standing end, and another, output waveguide (Fig. 1.11, 1.12). The static displacement and dynamic oscillation of the cantilever determines the mismatch between two waveguides, and therefore affects the coupling efficiency between the two waveguides and the output power. Alternatively, the displacement of the output light spot can be recorded directly on a photodiode or camera.

Light guide - cantilever sensors were shown to be promising as sensors of various chemical and biological compounds. Let us consider several interesting applications of theses sensors.

The work principle of most of these sensors is based on monitoring the static deflection of the waveguide - cantilever beam (Fig. 1.12). Highly integrated photonic sensor, that consist from a Si_3N_4 waveguide and stressed PMMA polymer film, was used to detect volatile compound vapors of water and organic solvents [Misiakos et al., 2009]. Another example of the application of static deflection technique is sensing various biological compounds, such as binding of the streptavidin to biotin molecules [Ness et al., 2013; Calleja et al., 2006b], detection of homocysteine amino-acid molecules [Koev et al., 2009] (see Fig. 1.13), and human growth hormone [Farina et al., 2016]. These studies demonstrated the operation of the sensors in liquid environment by integration the optical cantilever systems with microfluidic channels. The work principle of the observed response of these devices can be explained by the surface stress, that is caused by adsorption of the target molecules on the beam surface. One of the

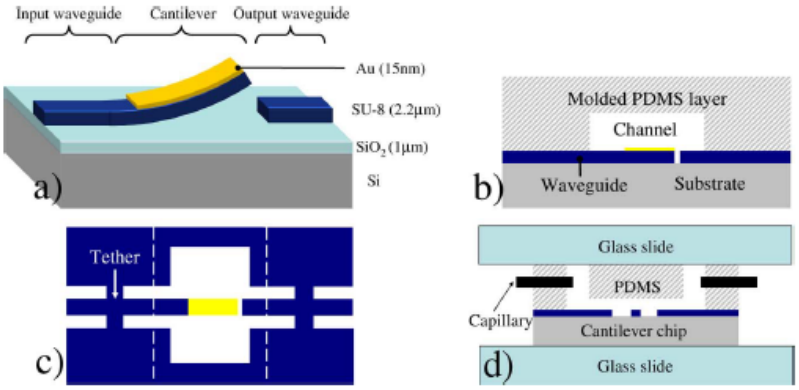

Figure 1.12: SU-8 cantilever sensor with an integrated optical readout [Koev et al., 2009]. (a) Schematic of the optical cantilever. (b) Cross section of the fluidic channel along the waveguide. (c) Top-down view of the SU-8 layer (dashed lines indicate the channel location). (d) Cross section of the assembled package along the fluidic channel. Thin metal layer on the top allows to functionalize the cantilever with thiol groups, and to use interferometric fringes readout as a confirmation of the correct values of the optical waveguide readout. SiO_2 layer under SU-8 is used as an optical cladding.

main sources of the variations in the baseline signal between different devices, and source of noise during measurements is the unstable coupling of the light, due to the drift of the mechanical stage [Koev et al., 2009]. The coupling efficiency of the two - waveguides systems limits the signal-to-noise ratio. Coupling efficiency of these systems is low, resulting in a typical overall losses of the order of 25 dB for some SU-8 cantilevers reported by Koev at. al, [Koev et al., 2009] or 27 dB for hybrid devices that consist of SiO_2 cantilevers and Si_3N_4 waveguides, reported by Zinoviev et al. [Zinoviev et al., 2006a]. These losses can be attributed to propagation losses and coupling losses at the interface between two waveguides, and interface between waveguide and input laser source [Koev et al., 2009]. In some works, the light is transmitted through the input waveguide, that is made from another material than the cantilever beam, and then is coupled inside the free-standing beam [Zinoviev et al., 2006a]; in such cases, there are also some coupling losses at the interface. Hybrid integration of the light source and detectors, good quality of the optical cladding can improve the minimal detectable

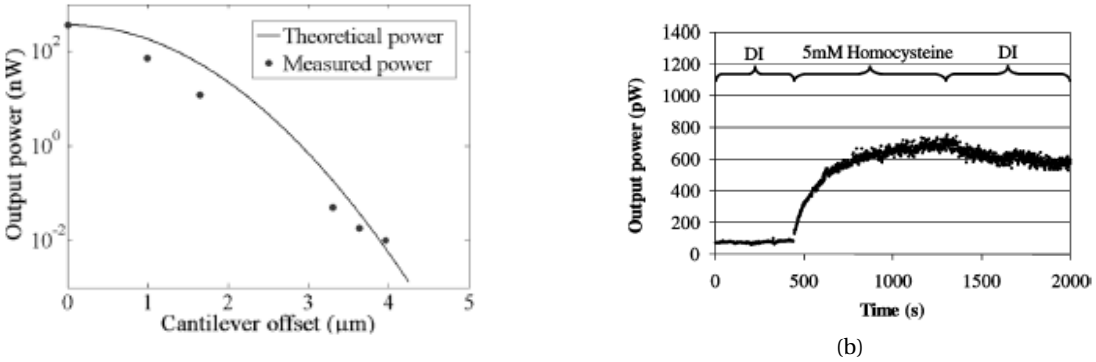

(a) (b)

Figure 1.13: (a) SU-8 cantilever-waveguide working principle: offset between the free-standing cantilever and the output waveguide decreases the coupling efficiency. Therefore changes in the output power are correlated with the beam displacement. Measured and theoretical optical output power versus offset for an unpacked sensor in dry state [Koev et al., 2009]. (b) Real-time response of an optical cantilever to 5-mM solution of homocysteine in DI water [Koev et al., 2009]. Binding of the homocysteine molecules results in compressive stress, static deflection of the beam and therefore change in the coupling efficiency of the waveguides and output power.

deflection [Koev et al., 2009], and further miniaturize the optomechanical sensor. Another challenge of the described waveguide coupling efficiency readout technique is the alignment of the cantilever beam with the static waveguide, and choice of the gap size between them [Zinoviev et al., 2006c,a]. Therefore, stress-free single-layer material is preferable for these kinds of devices, to avoid strong mismatch of the free-standing part of the waveguide with the static waveguide [Zinoviev et al., 2006a] due to the stress of the used fabrication material or bimetallic effect in case of multilayer structures.

As was described earlier, coating of cantilever surface with gold can be beneficial for functionalizing surface with thiol groups to use the sensors for bio-recognition. A metal layer provides the possibility of having an alternative way of signal readout using for example interference fringes or laser reflection optical scheme. However, coating the cantilever with metal has also drawbacks: it can cause deflection of the beam due to (a) mechanical stress, produced by bimetallic effect; (b) become more sensitive to the temperature changes, and (c) metal layer can absorb light, resulting in additional losses [Zinoviev et al., 2007].

In addition to the static deflection readout, also the dynamic operation of the cantilever-waveguide devices was demonstrated. However, this latter mode was mostly implemented to characterize the power spectra by driving cantilever chip with a piezo, and by detection of the cantilever displacement in air, while driven into oscillation at resonance frequency [Zinoviev et al., 2006a]. To our knowledge, the application of the waveguide-cantilevers, working in dynamic mode, for sensing, and especially in liquid environment was never implemented.

1.8 Conclusion

The Atomic Force Microscopy - based nanomotion technique is a promising tool for measuring the viability of the living organisms. It is not limited to one particular type of organisms, and was shown to work with a wide range of targets, including bacteria, yeast cells, bacteria from blood pellets, and human cancer cells. In addition to using it as a tool for screening for antibiotic and antifungal drug, this technique can be also applied for screening for bacteriofage-based drugs [Mertens et al., 2019]. The response of the nanomechanical cantilevers to living organisms is mostly limited to the low frequency range up to few hundreds of Hz. The most commonly used tools for monitoring this response is the calculation of the variance of the deflection in a given time window. But a frequency spectra analysis can be also an interesting approach, that could provide additional information about the frequency range of the response. The exact causes of the nanomotion sensors response is not clear, though it is believed to be correlated with surface stress, caused by organisms that act on different timescales. Nevertheless, this response can be affected not only by mechanical motion, but also by the optical effects, when some microogranisms pass the laser beam [Bennett et al., 2020].

The emerging of the cantilever - waveguides techniques is a promising development facilitating the integration and multiplexing of the nanomechanical sensor devices. Till now, their applications were mostly focused on the static displacement and resonance shift techniques. The typical readout scheme of these devices consists of two waveguides, from which one is completely static and the other has a free-standing end. The coupling efficiency between these waveguides is used as a readout signal. However, there are some challenges regarding the choice of the gap size, and especially the unavoidable position mismatch between the two waveguides that impairs the coupling efficiency. Also, in case of the cell viability sensor, a very small gap could be filled with micro-organisms too, that could strongly affects the light coupling efficiency. In chapter 3, an optical cantilever device for dynamic sensing of cells viability will be presented, that is based on the described techniques, but has only one waveguide-cantilever, with a readout the output light by a photo-diode or a camera.

2 Estimations of the cantilever mechanical properties

2.1 Introduction

In this chapter, different methods for theoretical and experimental estimation of the resonance frequency and spring constant of the cantilever beams are presented. Then, resonance frequency in air and spring constant for the SU-8 cantilevers with chosen dimensions are calculated with a finite element simulation (FEM) and analytically, using a Euler–Bernoulli beam model and Hooke's law. The chapter ends with an explanation of the main noise sources, that fundamentally limit system sensitivity, and gives some estimations of the output voltage noise for the used in this work amplification circuits.

2.2 Estimation of resonance frequency

2.2.1 Resonance shift in vacuum and inviscid medium

The resonance frequency of a rectangular cantilever beam in vacuum can be calculated as:

$$f_{res(vac)-rect} = \frac{1}{2\pi}\sqrt{\frac{E}{\rho_{beam}}}\frac{t}{L^2}, \tag{2.1}$$

where E is the Young's modulus of beam material, ρ_{beam} is the density of beam material, L is the length of the free-standing beam and t is the thickness of the beam.
In case of small dissipative effects, the relation between the resonance frequency in a viscous medium and vacuum, can be described as [Sader, 1998]:

$$\frac{\omega_{medium}}{\omega_{vac}} = (1 + \frac{\pi\rho_{medium}w^2}{4\mu}\Gamma_r(\omega_{R,n}))^{-1/2}, \tag{2.2}$$

where w is the width of the beam, μ is the mass per unit length of the beam, $\Gamma_r(\omega_{R,n})$ is the real component of the hydrodynamical function $\Gamma(\omega)$ for resonance frequency of order n. This hydrodynamical function is determined by the Reynolds number Re (Eq. 2.4), which defines the relation between inertial and viscous flow. If viscosity is negligible, $Re \to \infty$, and the ratio between the resonance frequency in the specific medium and in vacuum depends only from the densities of the beam and the medium, as well as of the width w and the thickness t of the beam [Sader, 1998]:

$$\frac{\omega_{medium}}{\omega_{vac}} = (1 + \frac{\pi \rho_{medium} w}{4 \rho_{beam} t})^{-1/2} \tag{2.3}$$

2.2.2 Estimation of resonance frequency for fabricated SU-8 beams

The SU-8 polymer was assumed to have the density and Young's modulus of $\rho_{SU-8} = 1200\,\mathrm{kg/m^3}$ and $E_{SU-8} = 4$ GPa respectively.
(Note: In literature Young's modulus of SU-8 varies from 2 GPa to 6 GPa [Wouters et al., 2011; Robin et al., 2014; Hopcroft et al., 2005]).
Let us consider the SU-8 beams (I) that were fabricated with the following dimensions: $l = 260\,\mu$m, $w = 20\,\mu$m, $t = 5\,\mu$m. For these cantilevers, the beams resonance frequency in vacuum can be estimated from Eq. 2.1: $f_{I-vac} = 21.5$ kHz.
After the optimization of the design, cantilevers (II) with width of $w = 50\ \mu$m, thickness of $t = 5\ \mu$m, and various length of $l_1 = 400\ \mu$m, $l_2 = 500\ \mu$m, and $l_3 = 650\ \mu$m have been microfabricated as well. Their resonance frequency in vacuum can be estimated as $f_{II-1-vac} = 10.2$ kHz, $f_{II-2-vac} = 6.5$ kHz and $f_{II-3-vac} = 3.8$ kHz.
Further, for the discussion of the resonance shift in air and water, let us consider cantilevers (I) (260 μm x 20 μm x 5 μm) with $f_{I-vac} = 21.5$ kHz. Their resonance frequency in air and water in the approximation of inviscid medium can be estimated from Eq. 2.3 as $f_{I-air} = 21.46$ kHz, $f_{I-water} = 11.3$ kHz respectively.

device 'generation'	thickness (t), μm	width (w), μm	length (l), μm	f_{vac}, kHz
I	5	20	260	21.5
II	5	50	400	10.2
II	5	50	500	6.5
II	5	50	650	3.8

Table 2.1: Resonance frequency of the SU-8 cantilevers of various geometrical dimensions in vacuum (estimated from Eq. 2.1).

2.2.3 Simulation of frequency plots in various medium

The simulations were performed with the *Stuctural - Acoustic Interaction* module of COMSOL. Calculations were performed in two steps: Eigenfrequency study *(1)*, and then Frequency Domain study *(2)* with frequency sweep from 0.1 to 100 kHz. To induce oscillation of the beam, gravity and edge load were applied. Air and water medium were simulated by placing

the cantilever beam inside a rectangular box of 100 μm x 100 μm x 500 μm, filled with a given medium (Fig. 2.1). The calculated resonance frequencies of the beam in various medium were: f_{vac} = 21.9 kHz, f_{air} = 21.8 kHz, f_{water} = 11.1 kHz, which are in agreement within 2 % with the analytically calculated ones from Eq. 2.3. As one can see from the estimated values of

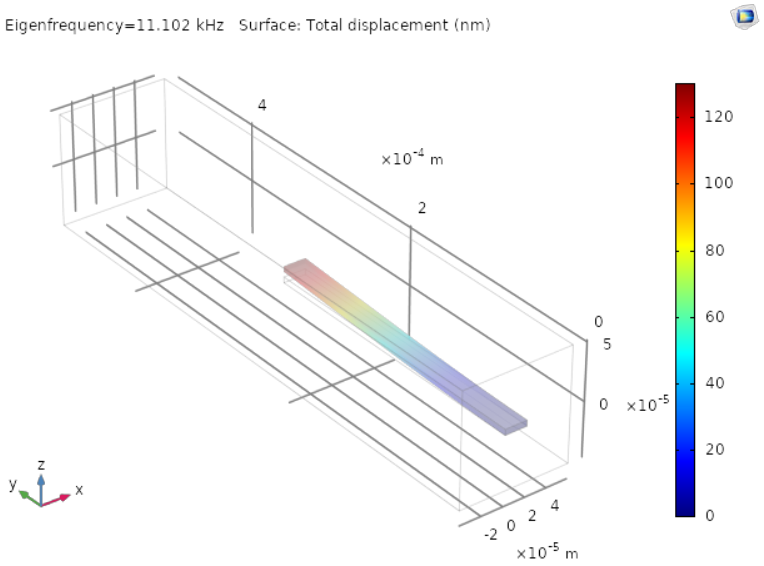

Figure 2.1: Model of SU-8 cantilever beam, immersed inside the volume filled with water medium (COMSOL Multiphysics).

the eigenfrequencies (Fig. 2.2), the resonance shift becomes significant when the beam is immersed in water, in comparison to air and vacuum, in which the resonance frequencies have close values.

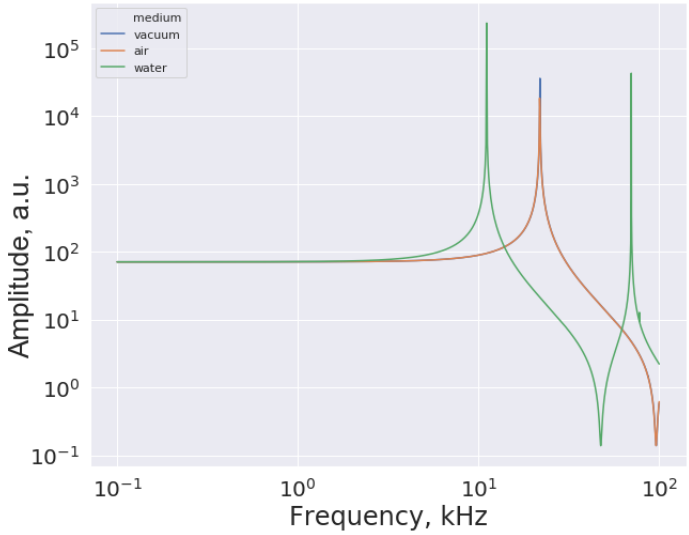

Figure 2.2: Frequency shift of the cantilever beam immersed in water (without taking into account losses) (COMSOL Multiphysics).

2.3 Resonance of the beams in viscous medium

2.3.1 Resonance frequency shift

There are various models that take into account the viscosity of the medium: models for free liquid such as Sader's model in the limit of small dissipative effects [Sader, 1998], Vankura's viscous method, or effective mass replacement model, while certain models consider a cantilever in the vicinity of a surface, such as the Rankl method, and a modal analysis [Korayem et al., 2011]. Let us consider Sader's model in the limit of small dissipative effects as one of commonly used ones. The angular resonance frequency shift can be described by previously introduced Eq. 2.2. The hydrodynamical function from this equation has the following asymptotic form:

$\Gamma(\omega) = 1$: $Re \to \infty$ (negligible viscosity)

$\Gamma(\omega) = \frac{-4i}{Re \ln(-i\sqrt{i\,Re})}$: $Re \to 0$

In the case of a rectangular beam of width w, oscillating at the characteristic angular frequency ω in the medium with density ρ and viscosity η, the Reynolds number Re is given by:

$$Re = \frac{\rho \omega w^2}{4\eta} \tag{2.4}$$

2.3.2 Quality factor

In the limit of small dissipative effects Sader has derived [Sader, 1998] the following expression for the quality factor of the n mode:

$$Q_n = \frac{\frac{4\mu}{\pi \rho_{medium} w^2} + \Gamma_r(\omega_{R,n})}{\Gamma_i(\omega_{R,n})}, \tag{2.5}$$

where $\Gamma_r(\omega_{R,n})$ and $\Gamma_i(\omega_{R,n})$- the real and imaginary components of the hydrodynamical function $\Gamma(f)$ for angular resonance frequency ω of mode n, μ is the mass per unit length of the beam, w is the width of the beam, ρ_{medium} is the density of the medium.

The quality factor in air also can be defined by the following expression [Lübbe et al., 2011]:

$$Q = \left(\frac{4\rho t w f_{res}}{6\eta + 3w\sqrt{\eta(M/RT)\pi f_{res} p}}\right), \tag{2.6}$$

where M is the fluid molecular mass, T - the fluid temperature, R - the universal gas constant, f_{res} - the resonance frequency in liquids, E' and E'' - the cantilever material storage and loss (Young's) modulus, t, w are the beam thickness and width, η and p is the dynamic viscosity and pressure of the medium.

2.3.3 Simulation of frequency plots with included losses. Estimation of the quality factor.

The previously described *Structural-Acoustic Interaction study* could not provide any information on the quality factor of the cantilever beam, since the losses were neglected. One of the methods to take this into account is the as-called *Thermoviscous Acoustic* study, that uses parameters such as the thermal conductivity, the heat capacity, and the viscosity of the medium, to give an estimation of the quality factor and to better estimate the shift of resonance frequency.
The *Thermoviscous Acoustic* study gives the eigenfrequencies that are complex - due to the damping effects. the simulation gives several eigenfrequencies with a very small real component. However, we are interested in the eigenfrequency with non-neglectable real part in the expected values region (some kHz). The first of these modes gives us the value of the resonance frequency of the beam (main harmonic).
The resonance of the cantilever, immersed in water medium, was estimated to be 6.9 kHz. It is ~ 1.6 times lower than the one which was calculated without taking into account losses and therefore, damping effects. The estimated damping ratio is 0.33, and the quality factor of the SU-8 beam in water is $Q = 1.5$.
The estimated resonance frequency of the beam in air with damping effects is 21.8 kHz , with a damping ratio of 0.009, and the quality factor $Q = 54$.

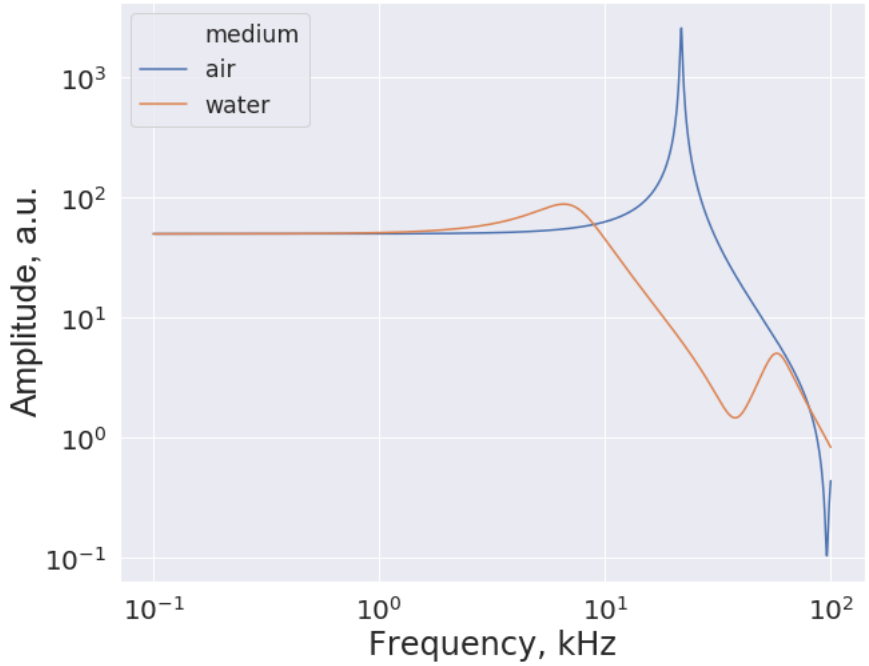

Figure 2.3: Frequency shift of a cantilever beam immersed in water taking into account losses by the *Thermoviscous Acoustic* study (COMSOL Multiphysics).

2.3.4 Simulation of cantilever beams with known resonance frequency

In order to verify the accuracy of the finite-elements COMSOL modeling, these simulations were repeated for cantilever beams with known resonance frequencies. For silicon cantilevers with dimensions $L = 197$ μm, $w = 29$ μm, $t = 2$ μm (*1*), and $L = 397$ μm, $w = 29$ μm, $t = 2$ μm (*2*), known and simulated resonance frequency in kHz in water medium is shown in the table 2.2 [Chon et al., 2000; Korayem et al., 2011]. The results of my COMSOL simulations seem to be in a good agreement with the reported numerical calculations and the experimentally measured data.

cantilever	f_{Rankl}	$f_{Viscous}$	f_{EMR}	$f_{Inviscid}$	$f_{experiment}$	$f_{simulated}(COMSOL)$
1	21.6	24.3	21.9	29.6	25.2	**21.4**
2	4.4	5.0	4.6	7.3	5.04	**4.05**

Table 2.2: Resonance frequencies in kHz of the silicon cantilevers from the literature [Chon et al., 2000; Korayem et al., 2011], and our COMSOL simulation (in bold) of the same cantilevers.

2.4 Spring constant of the cantilever sensors

When a force is applied to the cantilever beam, its displacement is defined by the spring constant, or the normal stiffness of the beam. According to the Hooke's law,

$$F = k\triangle z \tag{2.7}$$

If the beam is too stiff, the microorganisms activity on the beam would not be able to induce detectable vibrations. Too soft beam can be very fragile. However, they key consideration for choosing spring constant of the beam is the frequency region of interest, which determines ω (which in turns depends from k and m). There are various methods for estimating the spring constant of the free-standing rectangular beam, that include Bernoulli model, loaded mass method, thermal calibration, Sander's method and others.

2.4.1 Theoretical estimation of the spring constant

At first, let us consider the model of Euler–Bernoulli beam. The spring constant of the rectangular beam can be described as

$$k = \frac{Ewt^3}{4l^3}, \tag{2.8}$$

where E is the Young's modulus of the cantilever material, w, t, and l is the width, the thickness and the length of the beam respectively.
This equation was used to calculate the theoretical values of the spring constant of designed

cantilevers, and to choose accordingly the length of the SU-8 beams. The Young's modulus of SU-8 can differ (from 2 GPa to 6 GPa), depending on the process parameters, therefore, there can be some variation between the predicted and the experimental values. However, this is a simple and good estimate.
Let us make some estimates with Eq. 2.8 for the beams that were microfabricated (see Chapter 3) in this thesis, assuming $E = 5$ GPa. For the SU-8 cantilever with dimensions of $w = 20$ μm, $t = 5$ μm, $l = 260$ μm spring constant $k_I = 0.18$ N/m. For the SU-8 cantilevers with dimensions of $w = 50$ μm, $t = 5$ μm, and various length of $l_1 = 400$ μm, $l_2 = 500$ μm, $l_1 = 650$ μm, Eq. 2.8 gives $k_{II-1} = 0.12$ N/m, $k_{II-2} = 0.06$ N/m, $k_{II-3} = 0.03$ N/m respectively.
The spring constant of the SU-8 beams can be also predicted by using finite elements simulation (FEM). This simulation is performed by applying a force load on the end of the beam, and then using a Hooke's law (Eq. 2.7) to determine a spring constant from the simulated displacement of the beam (COMSOL Multiphysics, Stationary Study). This simulation is also a subject to the uncertainty of the SU-8 material properties, such as Young's modulus and Poisson ratio. FEM gives the following estimates of the spring constants of the SU-8 cantilevers: $k_{I-FEM} = 0.14$ N/m, $k_{II-1-FEM} = 0.1$ N/m, $k_{II-2-FEM} = 0.05$ N/m, $k_{II-3-FEM} = 0.02$ N/m.

2.4.2 Thermal calibration method (experimental)

The thermal method is one of the most commonly used methods for the calibration of the cantilever spring constant in the commercial atomic force microscopes (AFM). The physical principle of this method is based on measuring the thermal noise of the cantilever and on the use of the equipartition theorem[Hutter and Bechhoefer, 1993]:

$$\langle \frac{1}{2} m\omega^2 z^2 \rangle = \frac{1}{2} k_B T \tag{2.9}$$

where m is the oscillating mass, $\omega = \frac{k}{m}$ is the resonance angular frequency, z is the beam displacement, k_B is the Boltzmann constant, and T is the absolute temperature. Here the cantilever is modelled as an 1-dimensional spring with an attached mass. Therefore

$$k\langle z^2 \rangle = k_B T \tag{2.10}$$

This equation (2.10) can be used to determine the spring constant k from the experimentally measured signal. To suppress all other noise sources, the signal is typically studied in the frequency domain. In such case, background that is created by other sources of noise, can be simply subtracted. The observed resonance peak in the limit of small damping can be fitted to a Lorentz function, and the area under this curve gives the power of the fluctuations[Hutter and Bechhoefer, 1993]. We can use the Parseval's theorem, which states the equality between the total energy calculated in the time domain and the spectral power. From this, and from Eq. (2.10) we obtain:

$$k = \frac{k_B T}{P}, \tag{2.11}$$

where P is the area under the spectral power curve.
The spring constant measurement with the thermal noise method does not require any prior knowledge about the cantilever beam material and dimensions; it is easy and straightforward to perform, as long as there is an available calibration of the power spectra to nanometer-scaled amplitude. This calibration is normally done with use of the dedicated test sample, such as an array of steps with known height. Also, the resonance peak should be clearly distinguishable from the background noise, and not have any artifact peaks near to it.

2.4.3 Sader's method for calculating the spring constant (experimental)

Sader's method considers the behavior of cantilever beams in a viscous medium. This method is based on the computation of the so-called hydrodynamical function of the cantilever, that depends from the geometry of the beam and from the medium properties, such as density and viscosity. This method was originally developed for the cantilevers of rectangular shape, but later was generalized for arbitrary shapes.
The main advantage of the method is its independence of the beam thickness, density and Young's modulus of the cantilever material, which are the sources of uncertainties for the other methods. Instead, the Sader's method requires the resonance frequency and the quality factor of the resonance peak in the medium, as well as the properties of the medium.

$$k = 0.1906 \rho_m w^2 L Q_m \Gamma_i(\omega_m) \omega_m^2, \tag{2.12}$$

where ρ_m is the density of the medium, w and L is the width and length of the beam, Q_m is the quality factor of the resonance peak in the medium, ω_m is the resonance frequency in the medium, and Γ_i is the imaginary component of the hydrodynamical function.
Although the calculation of the imaginary hydrodynamical function can be complex, the authors provided online tool [Sader et al., 2016], where this function is calculated, based on the selected geometrical dimensions of the beam (width and length), as well as medium properties. This simplifies use of the method for the cantilever spring constant calibration.
Another limitation of the model is given by the condition that the damping of the resonance in the viscous medium has to fulfill: the Eq. (2.12) is valid when the quality factor of the resonance of the fundamental mode is $Q_f \gg 1$.

2.4.4 Added mass (Cleveland) method (experimental)

The spring constant calibration method, proposed by Cleveland et al. [Cleveland et al., 1993], is based on measuring the resonance shift, when a sphere with known mass is placed on the cantilever free end. Its advantage is independence not only from Young's modulus, but also from the geometrical dimensions of the beam. However, the experimental procedure of placing the spheres on the free end of the beam, can be complex and time consuming. Moreover, there is a danger to damage the beam during this procedure, and it is difficult to remove the attached spheres for the further use of the beam with unmodified properties.

However, this method is also interesting in conjunction with cantilever beams of known spring constant as precise mass sensors.

$$k = (2\pi)^2 \frac{M}{(\frac{1}{f_1} - \frac{1}{f_0})} \quad \text{[Cleveland et al., 1993]}, \tag{2.13}$$

where M is the added mass, f_0 and f_1 are the resonance frequencies of the beam before and after the adding sphere with known mass.
Cleveland et al. has also proposed a modification of his method, that allows to estimate the resonance frequency of the unloaded beam. For this calculation, no additional manipulations with the beam are needed, except for measuring the power spectra of it. However, this computation relies on the Young's modulus of the beam material, which can be a source of the uncertainty.

$$k = 2\pi^3 L^3 w \sqrt{\frac{\rho^3}{E}} {f_0}^3, \tag{2.14}$$

where L and w are the the length and the width of the beam, ρ and E are the density and the Young's modulus of the cantilever material, f_0 is the free resonance of the cantilever beam.
In addition to the local deposition of sphere, a deposited gold layer on the cantilever surface can serve as an added mass [Gibson et al., 2001]. This can be easier from the practical point of view, than local attaching the spheres to the surface. However, the metal layer should be thin enough, to induce the resonance shift without a significant change of the spring constant.

2.4.5 Indentation method (experimental)

Nanoindentation method is based on the application of load on the studied cantilever beam with an so-called indenter tip. This non-destructive technique allows to measure the spring constant without any prior knowledge about the geometrical dimensions or material properties of the beams [Cumpson et al., 2008; Ying et al., 2007]. To do so, the displacement of the indenter tip is recorded. According to the Hooke's law, the spring constant is extracted from the relation between the applied force and displacement of the calibrated indenter.

$$k = \frac{\triangle F}{\triangle z} \tag{2.15}$$

The main disadvantage of this technique is a complexity of placing an indenter tip in the correct position [Cumpson et al., 2008].

2.5 Fundamental source of noise

2.5.1 Types of the noise in the cantilever sensor measurement system

There are the following types of fundamental noises in the cantilever-based sensing system: flicker noise, shot noise, and Johnson–Nyquist thermal noise. Let us briefly describe each of them.
The ***flicker noise*** is an electronic noise that has typically a 1/f behavior, and hence is also

called 1/f noise. Its physically nature is not exactly understood. This noise is present in the low frequency range of the power spectra, and is often filtered out in the scientific instruments by using high-pass filters. However, in the case when the relevant signal is also located in the low frequency range not much can be done a posteriori to suppress this noise. This phenomenon is observed not only in electronics devices, but also in biology. The low-frequency response of the cantilever beam to the activity of the attached micro-organisms, can be also related to the flicker noise.
The 1/f voltage (in V/$\sqrt{\text{Hz}}$) or current noise (in A/$\sqrt{\text{Hz}}$) spectral density can be described by the following equation [Jung, 2004]:

$$V_n, I_n = k\sqrt{\frac{F_c}{f}}, \tag{2.16}$$

where k is the level of the white current or voltage noise (at the higher frequencies), and F_c is so-called corner frequency, below which the noise starts to rise (see Fig. 2.4a).

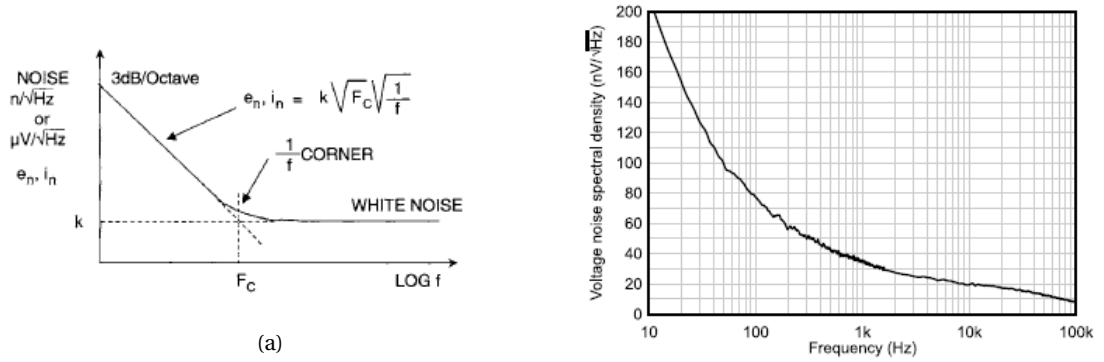

(a) (b)

Figure 2.4: (a) Typical (theoretical) 1/f noise of the operational amplifier, and definition of the corner frequency F_c [Jung, 2004]. (b) Voltage noise spectral density, nV/$\sqrt{}$(Hz) vs frequency, Hz of the operational amplifier (datasheet), that was used in the photodetector signal amplification board [Instruments, 2021].

The ***shot noise*** originates from the particle (discrete) nature of electric charge and of light, and present in electronic and optical devices. The electrons, or photons, come in quantized packets, and amount of the emitted particles is not constant. This variation causes some fluctuation of the brightness (or current), called a shot noise. This type of noise can be dominant, when the total amount of the particles is small. Random amount of the emitted particles per second is described by the Poisson distribution, and the root mean square of the current fluctuations can be described as:

$$\sigma_i = \sqrt{2qI\Delta f}, \tag{2.17}$$

where q is the electron charge, I is the average flowing current, and Δf is the measurement bandwidth.

The photodetector is mounted on the amplification board, whose gain is defined by the feedback resistors. Each of the resistors has a ***Johnson thermal noise*** in the whole frequency range. It is considered to be a 'white noise', i.e., noise that has equal amplitude at different frequencies. According to the equipartition theorem,

$$N = k_B T \triangle f, \tag{2.18}$$

where N is the noise power, k_B is the Boltzmann constant, T is an absolute temperature, and $\triangle f$ is the measurement bandwidth.
An electric circuit with resistance R generates the root mean squared (RMS) voltage noise of

$$v = \sqrt{4k_B T R \Delta f}, \tag{2.19}$$

or a current RMS noise of

$$i = \sqrt{\frac{4k_B T \Delta f}{R}}. \tag{2.20}$$

In addition to resistors, operational amplifiers, that are used for amplification of the photodetector current, as well as exhibit a combination of the 1/f and white noise.

2.5.2 Estimations of the noise

Let us estimate the approximate values of the noise in the experimental system that was developed in this work.

Noise of the resistors and operational amplifiers in the printed circuit board (PCB)

First of all, let us consider the thermal noise of the amplification board. Since the light coupling efficiency was low, and a high amplification gain was used, hence a high feedback resistance, this thermal noise can be dominant. There were two amplification boards that were used for the cantilever readout, with a total gain of 10^8 and 10^7. The amplification was performed using two stages: a transimpedance amplifier with a feedback resistor of $R_{f1} = 1$ MΩ (Fig. 2.5a) that defines a gain of $G_1 = 10^6$ V/A, and second, voltage amplifying stage (Fig. 2.5b) with feedback resistor $R_{f2} = 120$ kΩ and input resistor $R_3 = 1.2$ kΩ, or $R_{f2} = 12$ kΩ and $R_3 = 1.2$ kΩ, for having gain G_2 equal to 100 and 10 on the second stage of amplification respectively. Other resistors in the circuits have resistance that is of order of just ~ 1 kΩ. Eventually, we can consider thermal noise that is generated just by the 1 MΩ resistor of the first amplification stage, as noise that is generated by all other resistors in the circuit is negligible in comparison to it.

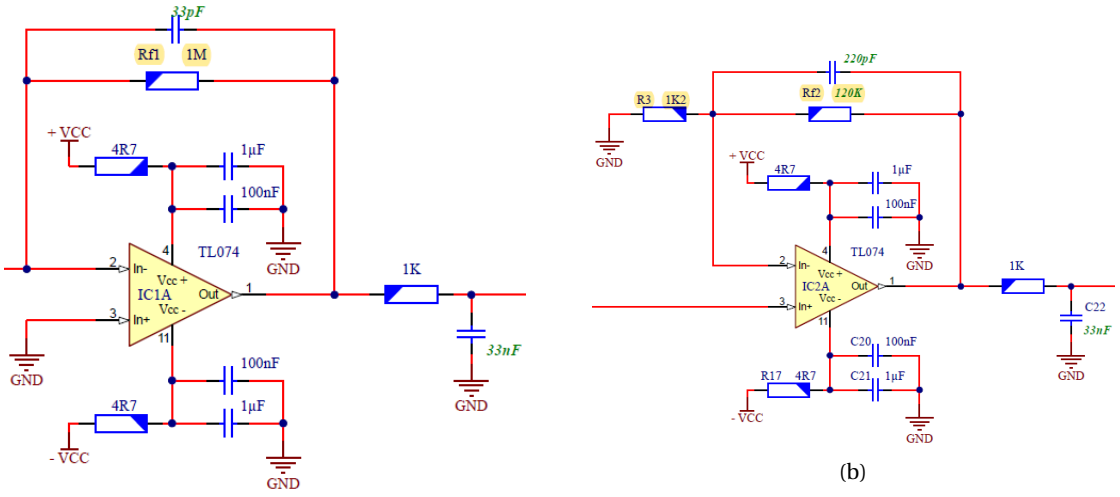

Figure 2.5: (a) Schematics of the transimpedance amplifier (first amplification stage) with a gain of $G = 10^6$ V/A, defined by the resistor $R_{f1} = 1$ MΩ. (b) Schematics of the voltage amplifier (second amplification stage) with a gain of $G = 100$ V/V, defined by $1 + \frac{R_{f2}}{R_3} = 101 \approx 100$.

The source of the signal in the circuit is the photocurrent, which is generated by the photons, hitting the photodetector sensing area. Therefore, it makes sense to talk about current noise density, that is generated by the first amplification stage.

$$I_{n-1} = \sqrt{\frac{4k_B T}{R_{f1}}} = 127 \text{ fA}/\sqrt{(\text{Hz})} \tag{2.21}$$

, which result in RMS current of 22 pA for the bandwidth $\triangle f = 30$ kHz. Then this current is amplified twice and gives the following voltage noise per frequency (spectral density):

$$V_{n1} = \sqrt{4k_B T R_{f1}} G_1 G_2 = \sqrt{4k_B T R_{f1}} G; \tag{2.22}$$

$V_{n1-1} = 12.7\ \mu\text{V}/\sqrt{Hz}$ for $G = 10^8$ and $V_{n1-2} = 1.27\ \mu\text{V}/\sqrt{Hz}$ for $G = 10^7$.
In principle, $V_{n-Johnson} = \sqrt{{V_{n1}}^2 + {V_{n2}}^2}$, where V_{n1} and V_{n2} is the voltage noise, generated by the first and second amplification stage of the circuit. But as the resistance of the second stage is much smaller than the one of the first stage, $V_{n2} \ll V_{n1}$, so we can neglect the noise produced by the second amplification stage. We conclude that the Johnson noise of the circuit is equal to V_{n1}.
The operational amplifiers that were used in the circuit (Quad JFET TL074CDT, Texas Instruments), have an input voltage density equal to $V_{input-n-OP} = 37$ nV/$\sqrt{(\text{Hz})}$ at $f = 1$ kHz, 21 nV/$\sqrt{(\text{Hz})}$ at $f = 10$ kHz (Fig. 2.4b), and input current density of $I_{input-n-OP} = 80$ fA/$\sqrt{(Hz)}$. Let us estimate the current noise power density that is produced by the amplifier in the first

amplification stage in the absence of other sources:

$$I_{1-OP}{}^2 = I_{input-n-OP}{}^2 + (\frac{V_{input-n-OP}}{R_f})^2, \tag{2.23}$$

resulting in the output voltage noise power density of

$$V_{1-OP}^2 = (\sqrt{I_{input-n-OP}{}^2 + (\frac{V_{input-n-OP}}{R_f})^2}\, G_1 G_2)^2, \tag{2.24}$$

where R_f is the feedback resistance, $V_{input-n-OP}$ and $V_{input-n-OP}$ is the current and voltage input noise density of the operational amplifier, G_1 and G_2 is the gain of the first and second amplification stages. Since most of the amplification happens on the first stage, we neglect the noise that is generated by the operational amplifier of the second stage. Using Eq. 2.24, an output voltage noise density, that is generated by the operational amplifier in absence of other noise sources would be $V_{OP-G8} = 8.8\ \mu$V/Hz for the board with $G = 10^8$, and $V_{OP-G8} = 0.88\ \mu$V/Hz for the board with $G = 10^7$.
If we consider 1 kHz as a frequency after which operational amplifier has close to the white noise behaviour (Fig. 2.4b), then flicker noise power at lower frequencies can be defined as

$$V_{n-OP-1/f}^2 = (\sqrt{(I_{OP-1/f})^2 + (V_{OP-1/f}/R_f)^2}\, G_1 G_2)^2 = (\sqrt{(I_0\sqrt{\frac{F_c}{f}})^2 + (V_0\sqrt{\frac{F_c}{f}}/R_f)^2}\, G_1 G_2)^2, \tag{2.25}$$

where F_c is the corner frequency. F_c and $V(f_0)$ can be determined from the power spectra of the operational amplifier (Fig. 2.4b).

Shot noise of the photocurrent

Unlike the estimations of the resistor thermal noise, the shot noise cannot be calculated based on only theoretical values, as it depends from the photodiode current, that is defined by the experimental conditions and light coupling efficiency. Let us consider the amplification board with a total gain of $G = 10^8$. The typical signal level of the single photodiode could be in the range from few hundreds mV to few V, having approximate minimum and maximum values of the order of $V_{min} = 0.1$ V, and $V_{max} = 10$ V, corresponding to current of 1 nA to 100 nA. Therefore, according to the Eq. (2.17), the shot noise density can be estimated to be in the range from 17.9 fA/$\sqrt{\text{Hz}}$ to 179 fA/$\sqrt{\text{Hz}}$. After two stages of amplification, the shot noise results in the voltage noise density in a range 1.79 μV/$\sqrt{\text{Hz}}$ to 17.9 μV/$\sqrt{\text{Hz}}$ for total gain of $G = 10^8$.After comparing these values with the resistor and operational amplifier noise, we can conclude, that at the lower limit of the light coupling efficiency the thermal noise of the resistor is dominating, while at the higher limit, which is a saturation level of $V_{max} = 10$ V, the shot noise of photocurrent exceeds the Johnson noise of the resistors.

Total noise

The output voltage noise that is given by the main fundamental sources: Johnson noise of the feedback resistor, noise of the operational amplifier and shot noise, and can be estimated by the following expression:

$$V_{tot-rms} = V_{tot-density}\sqrt{\Delta f} = \sqrt{{V_{n-Johnson-R_f}}^2 + {V_{n-OP}}^2 + {V_{n-shot}}^2}\sqrt{\Delta f} \tag{2.26}$$

then

$$V_{tot-rms} = \sqrt{\frac{4k_BT\Delta f}{R} + {I_{input-n-OP}}^2 + (\frac{V_{input-n-OP}}{R_f})^2 + 2qI} \quad G_1G_2\sqrt{\Delta f} \tag{2.27}$$

Let us estimate the total voltage noise for the board with am amplification gain of $G = 10^8$ for two situations: high light intensity ($V_{shot} = 17.9\ \mu\text{V}/\sqrt{\text{Hz}}$) and low light intensity ($V_{shot} = 1.79\ \mu\text{V}/\sqrt{\text{Hz}}$). In the first situation, voltage noise density becomes $V_{tot-density-high-I} = \sqrt{(12.7\cdot10^{-6})^2 + (8.8\cdot10^{-6})^2 + (17.9\cdot10^{-6})^2}\cdot10^8 = 23.7\ \mu\text{V}/\sqrt{\text{Hz}}$, and for bandwidth of $\triangle f = 30$ kHz gives a RMS voltage noise of $V_{tot-rms-high-I} = 4.1$ mV. In the second situation, resistor and operational amplifier noise dominate over shot noise, $V_{tot-density-low-I} = \sqrt{(12.7\cdot10^{-6})^2 + (8.8\cdot10^{-6})^2 + (1.79\cdot10^{-6})^2}\cdot10^8 = 15.6\ \mu\text{V}/\sqrt{\text{Hz}}$, and for bandwidth of $\triangle f = 30$ kHz results in a RMS voltage noise of $V_{tot-rms-low-I} = 2.7$ mV.

2.6 Conclusion

Resonance frequency of the SU-8 cantilever beams with a given dimensions was calculated analytically in vacuum, and estimated using a finite elements simulations in vacuum, air, and water. Different methods for estimating spring constant were considered, including the Euler-Bernoulli model, the finite elements simulation of the beam with applied static force, the thermal calibration, Sader's method, the added mass method, and finally the indentation method. These techniques have the following advantages and limitations. Euler-Bernoulli model allows to estimate cantilever spring constant (k) theoretically, and was used to calculate the theoretical value of k of the designed levers. Sader's and added mass methods allow to avoid use of uncertain material properties, such as Young's modulus and thickness of cantilevers. Sader's method allows to calculate the spring constant using the power spectra that is recorded in the viscous medium, and can be extended for a beam of arbitrary shape. However, the damping effects should not be too strong. The computation is rather complex. The added mass method requires a time-consuming experimental procedures of placing a load on the cantilever. Though there is a modification of the method for computing the spring constant of the unloaded beam, it suffers from use of the cantilever material properties. the indentation method also helps to avoid the use of uncertain parameters of the beam, and completely relies on the experiment. It has to be performed with care in order to prevent damage of the cantilever beam. And finally, the thermal method requires a reliable nanometer-scaled

calibration of the power spectra, and a well-defined resonant peak above the background noise.

There are several fundamental sources of the noise in the system: thermal noise, flicker or 1/f noise, and shot noise. Contribution of each of the noise types was estimated, using the parameters of the amplification board, and test results of the system. Depending on the coupling efficiency, the shot noise can exceed the thermal noise of the resistors in the amplification board, or be lower than thermal noise. In the low frequency region of the power spectra, that is a region of interest for biosensing of micro-ogranism activity, the 1/f noise dominates over other types of noise.

3 Microfabricating of the device and developing measuring setup

3.1 Introduction

This chapter describes in details the proposed sensing devices and elaborates on its design, different strategies for the microfabrication of SU-8 - based optomechanical sensors, as well as challenges in the processing of SU-8 polymer. It also describes the developed experimental setup for optomechanical measurements, the light-coupling procedure and data acquisition.

3.2 Device design and working principle

The concept of the sensing device is a chip with a polymer structure, that has a free-standing beam, and a part that is responsible for guiding light towards the beam. The beam is suspended above etched cavity. In principle, the most simple patterning structure would be a straight light guide with a released part at its end. However, to avoid detecting light from the source as part of the readout signal, a structure with curved light guide was implemented.
To have the end of the free-standing beam as close to the chip border as possible, avoid reflections and absorption of light by the substrate surface, the patterned structure was made with the following shape: coupling-in side is located in the middle of long side of the chip, then has curvature, and continued to the end of the chip, such that free standing beams end near the middle of the short side of the chip (see Fig. 3.1). Large length of the light guiding part increases propagation losses, but simplifies the alignment procedure and minimizes the background light illumination.
SU-8 polymer was chosen for patterning the light guiding and free-standing parts of the sensor because SU-8 is a bio-compatible [Chen and Lee, 2021; Nordstrom et al., 2008], well-known use for fabricating both cantilever beams and lightguides Abgrall et al. [2007]; Nordstrom et al. [2008]. Its photoresist properties allow microfabrication using a direct UV patterning.

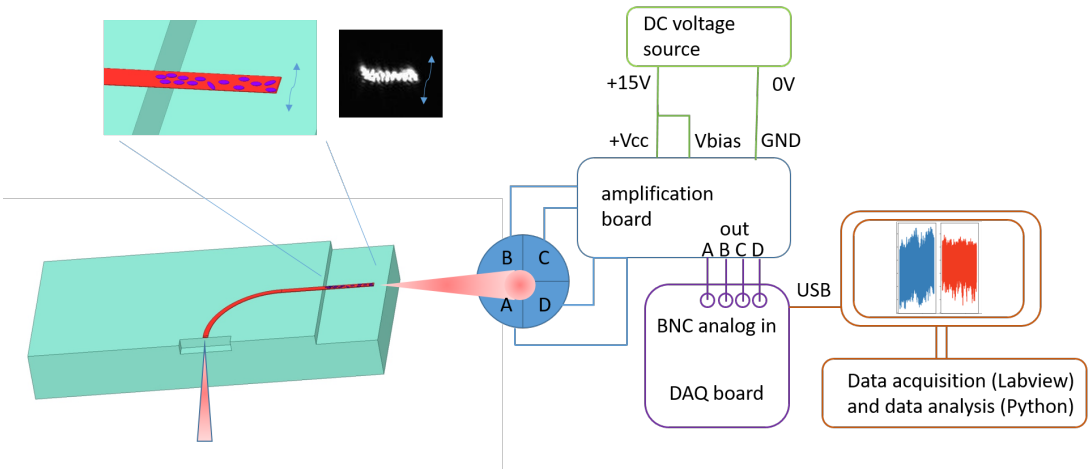

Figure 3.1: Schematics of the measurement setup (not to scale)

3.2.1 Design of the optical part of polymer structure

In the proposed readout scheme, the cantilever does not require any metal coating. Indeed, SU-8 coating with metal represents a challenge due to the weak adhesion and high thermal sensitivity induced by the double layer stress. It is a challenging task to have a good quality cladding in the light guiding part of the device, while not affecting the mechanical properties of the free-standing part of the SU-8 structure. In the final design of the presented device, 2 μm layer of silicon dioxide was proposed as a cladding for the light guiding part of the structure, while free-standing part of the beam has air or liquid medium around, that has lower refractive index than SU-8, and therefore also helps to confine light in the beam. Variation of the process flow without oxide under the SU-8, was tested as well. In future modification of the system, the optical properties of the device could be improved by using a better quality and higher thickness cladding layer, or silica substrate, that posses better light coupling efficiency.
At the beginning of the project, several light coupling schemes were considered. In addition to the direct readout scheme, depicted in Fig. 3.2 A, B, the readout could be performed by coupling cantilever with an output waveguide (Fig. 3.2 C, D). However, the latter approach has challenges of the offset between the cantilever beam (due to its possible bending) and the light guide. In addition the light coupling efficiency could be compromised by a change in the refractive index of the medium or presence of particles in the liquid medium. Therefore, a choice was made in a favor of the direct light readout scheme. In the future implementations, the device could have an array of the microsensors (Fig. 3.2 A, C) on one chip. However, to show proof of concept of this novel device, and simplify the process flow, only chips with a single sensor were implemented.

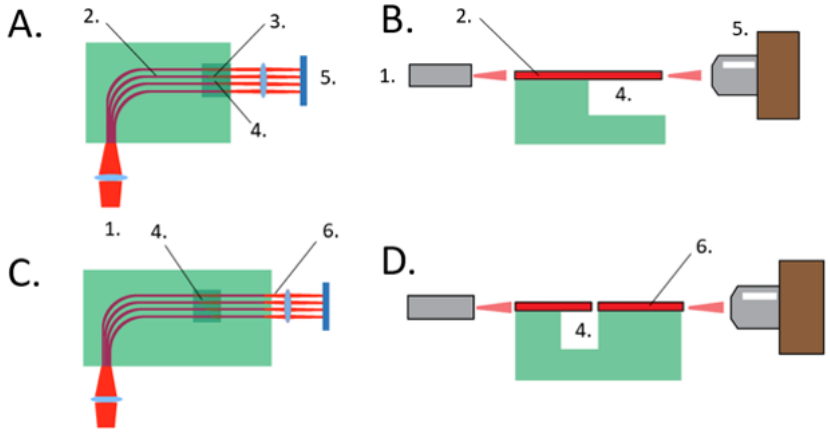

Figure 3.2: Schematics of the direct optical readout (A, B) and light coupling efficiency readout (C, D). 1 - laser light source, 2 - light guiding part of SU-8 polymer, 3 - suspended beam, 4 - cavity under the beam, 5 - readout optics with CCD camera and photodetector, 6 - output light guide for the coupling efficiency readout.

In the first design, the SU-8 thickness was set to 2 μm. Later this thickness was increased up to 5 μm, to enhance the portion of the light hitting the SU-8 structure, since it is particularly difficult to focus light to a spot with a diameter smaller than 5 μm. During the process flow optimization, sides of the SU-8 light guiding structure that were used for coupling light -in and -out of the structure, were placed as close as possible to the edge of the chip.

3.2.2 Design of the etching pattern

The free-standing beam geometry was designed to reach a spring constant close to 0.05 N/m - 0.1 N/m. This choice was motivated by the fact that beams with such a stiffness are typically used for the AFM - based nanomotion viability tests. However, for test purposes, beams with with a design spring constant from 0.02 to 0.25 N/m were fabricated. The thickness of the SU-8 was set to 5 μm, to match the minimum possible diameter of the focused light spot. The width of the beam was set to 20 μm in the first generation of the fabricated devices, and was increased to 50 μm during the optimization process.
In the first generation of the fabricated devices, the etching cavity had a rectangular shape, with beam end at a few hundred of μm from the border of the chip (Fig. 3.8, Fig. 3.7a). In the next generation, the width of the etching cavity was increased to whole width of the chip, and located in such a way that cantilever beam would end approximately just 50 μm from the edge of the chip (Fig. 3.7b). Additionally, or small etching window was designed at the light guide entrance, to facilitate access of the light. For testing purposes, in some of the samples two mirrored structures were patterned on the same chip (Fig. 3.7). This allows to use the same sensor several times. Because the beams release was performed in the isotropic etching process, there was an underetch of the mask. The deigned patterning was corrected accordingly, to have the free-standing beams of the following length: 290 μm, 400 μm, 500 μm, 650 μm. These dimensions correspond to the theoretical spring constant values of 0.25 N/m,

0.1 N/m, 0.06 N/m, and 0.02 N/m, respectively. Cantilevers with a spring constant in a range of 0.02-0.1 N/m were then mechanically characterized, and devices with a beam length of 500 μm were used for the presented biological experiments.
SU-8 polymer structure had the same shape and dimensions on all chips on the wafer, and only the layout of the etching mask was different. It permitted to manufacture chips with various stiffnesses.

3.3 Microfabrication of SU-8 cantilever chips

One of the approaches to fabricate SU-8 cantilever chips is to use multi-layer SU-8 structures, from which one layer is used as a beam, and other(s) layers - as base of the cantilever chip ([Hopcroft et al., 2005; Nordstrom et al., 2008; Abgrall et al., 2007; Martinez et al., 2016a]). In such an approach, each layer is exposed and developed separately. Eventually, the chip made entirely from SU-8 is released from the silicon wafer either by removing a sacrificial layer between the SU-8 and the Si wafer, or by wet etching of Si wafer, that leads to delamination of the multi-layered SU-8. This approach looks straightforward, but is not ideal for the lightguide application, since in this case the whole chip is made out of SU-8. Besides this, it requires a mechanical detachment of the chips from the wafer, that may damage the cantilevers.
However, alternative approaches exist, that allow to avoid any mechanical detaching steps, and to keep SU-8 on the substrate surface. It includes using double-layer (see section 3.3.2) of SU-8 with a buried exposure (without detaching from the surface), wet (section 3.3.3) and dry etch (section 3.3.4). As shown further in this chapter, the dry etch approach was found to be the most suitable for the manufacturing proposed SU-8 optomechanical sensing device.

3.3.1 Processing of SU-8 photoresist

SU-8 photoresist has a broad range of applications, that includes electrical passivation, use as structural material for micro-electromechanical devices (MEMS), microfluidics, biological applications, cantilevers and optical waveguides. Thanks to the photoresist properties of this polymer, direct patterning of the structures by UV photolithography becomes possible. In this work, we used the mask-less lithography technique (Heidelberg MLA 150), that scans the wafer surface, and exposes resist to UV light irradiation according to a pattern design. The same technique was used for exposing general purpose photoresists.
One of the challenges of the SU-8 processing is its adhesion to the surface of Si wafer and SiO_2 oxide layer. To improve the adhesion, the wafers were pre-treated with O_2 plasma for 7 minutes, using a 500 W plasma power. During the optimization of the process, a step of HMDS (hexamethyldisilazane, chemical formula $C_6H_{12}NSi_2$) vapour treatment was added to further improve the adhesion between the wafer surface and the SU-8. Then, the SU-8 resist was gently poured on the wafer surface, avoiding formation of bubbles, and spin-coated with a dedicated ramping speed to get a required SU-8 thickness. Later the SU-8 thickness was assessed by means of various characterization methods, such as optical microscopy, scanning electron microscopy (SEM)(Fig.3.12), mechanical (Fig. 3.3a) and optical profilometry (Fig. 3.3b).

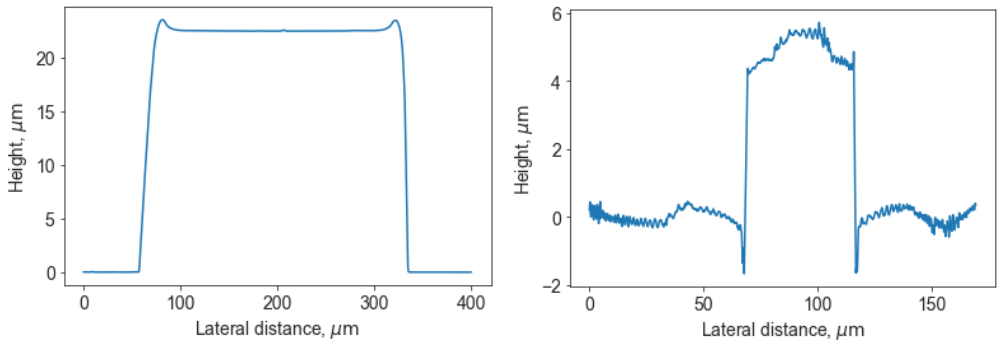

(a) (b)

Figure 3.3: (a) Mechanical profilometer (Bruker Dektak XT surface profiler) measurement of a test SU-8 layer with a target 25 μm thickness, and (b) white light interferometry (Bruker Contour X) measurement of a profile of 5 μm - thick SU-8 structure.

The next steps of SU-8 processing included several thermal baking steps and UV exposure. All these steps affect the SU-8 adhesion, its uniformity, and define the stress in the polymer structure [Keller et al., 2010, 2008]. These processing parameters also affect the mechanical properties of the SU-8, such as its Young's modulus, Poison's ratio [Chung and Park, 2013a; Keller et al., 2008] and its optical parameters, in particular its refractive index [Martham et al., 2014].

The thermal processing includes 3 types of baking: softbake, post-exposure bake (PEB) and hardbake (optional). Softbake is performed after spin-coating the resist film and the relaxation delay. This time delay allows the film to distribute uniformly over the wafer surface, but is more important for thicker SU-8 films; for thin films of few μm, that were used to fabricate SU-8 cantilevers, a relaxation delay of just few minutes is enough. The purpose of softbake is the removal of all the solvent from the resist layer which affects lithography performance, such as: subsequent polymerization, cracks formation and material stiffness [Anhoj et al., 2006]. The SU-8 is sensitive to thermal stress, and it is important to avoid any rapid changes of temperature. Therefore, in all the baking steps heating and cooling was performed with a ramp slope of 2 C/min or slower. In addition, the wafer was left to relax overnight after each thermal baking step, before any next step of the process flow was performed.

The purpose of the post-exposure bake is to accelerate the cross-linking of the exposed parts of the polymer, so that they become insoluble in the developer solution. Finally, the hardbake was an optional baking steps, that was conducted after the SU-8 structures are developed. It helps to improve adhesion, remove cracks in the SU-8 structures thanks to resist reflow during baking, reduce stress. It was also shown that hardbake allows to use fabricated devices at temperatures below the temperature of hardbake ([Chung and Park, 2013b]). The hardbake can also minimize chance of the damage of the SU-8 structures during the further steps of process flow, such as baking of other resist and plasma etching.

The UV exposure dose is an important parameter to guarantee a proper cross-linking of the structures, prevent the delamination of the SU-8 during the development process, and minimize the amount of stress, received during irradiation. The calibration array of the structures

with different exposure doses was performed, to determine the correct dose. The development was performed in a PGMEA (propylene glycol monomethyl ether acetate) solution, for the shortest possible time, since a long development could lead to the delamination of the structures.

3.3.2 Double-layer SU-8 structure for free-standing beams release

Some works describe the fabrication of SU-8 cantilevers using a thin SU-8 layer for creating the beam, and a thicker SU-8 layer, as a base (body) of the cantilever chips [Hopcroft et al., 2005; Nordstrom et al., 2008; Martinez et al., 2016a]. However, typically the second layer is exposed and developed after the first layer is already patterned, and then both structures are detached from the substrate, using sacrificial layers and simple mechanical detachment.
An alternative approach, that does not require a mechanical detachment of the cantilever chip from the silicon (Si) surface, can be proposed (see Fig. 3.5). A thicker, 'body' SU-8 layer can be exposed without being developed, and then work as a sacrificial layer for the subsequently coated thinner SU-8 layer ([Ceyssens and Puers, 2006; Moser et al., 2011]). However, SU-8 photoresist has a very low light absorbance of UV irradiation at a wavelength of 375 nm, that was used for mask-less exposure. Several dose calibration test were performed, but it was not possible to expose only top part of SU-8, without penetration of irradiation in the bottom part of SU-8. There are several solutions for preventing UV irradiation from reaching the bottom SU-8 layer, while exposing the top layer: enhancing absorption properties of the top layer [Moser et al., 2011] and adding a metal layer that blocks UV irradiation[Ceyssens and Puers, 2006].

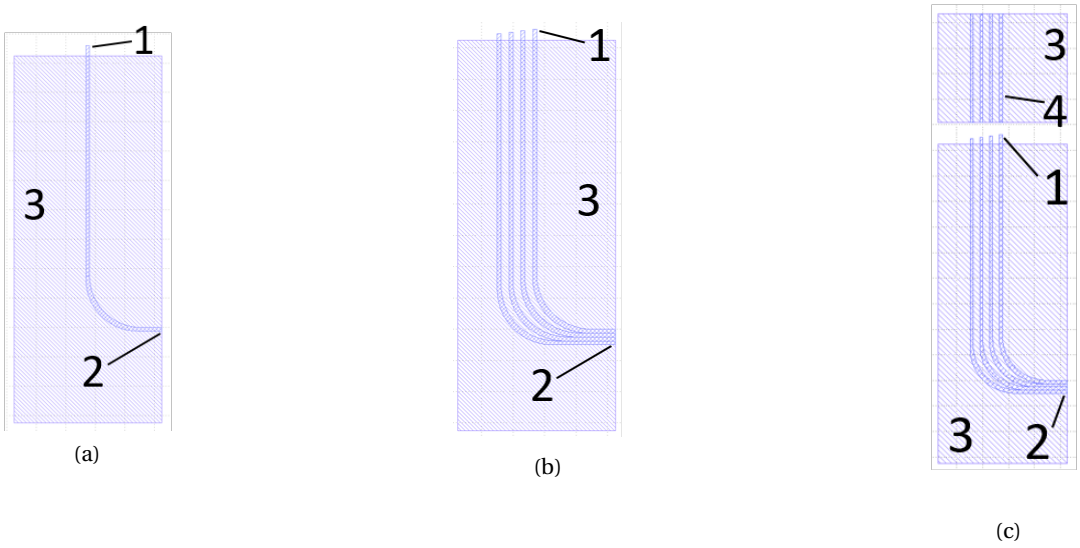

Figure 3.4: Design of the double-layer SU-8 structure: single cantilever device with a direct light readout (a), multi-sensor device with a direct light readout (b), and multi-sensor device with a coupling-efficiency readout (c). 1 - free-standing beam, 2 - spot for coupling light in, 3 - SU-8 body (25 μm thick), 4 - output light guides.

Let us consider the approach with two SU-8 layers and a protective metal film in detail (Fig. 3.5, Fig. 3.4).
A 25 μm-thick SU-8 (GM 1070) layer is spin-coated with a speed of 3000 rpm on the Si surface (Fig. 3.5, step 1), to function as a base of cantilever, and as a sacrificial layer for releasing the free-standing beam. This layer is exposed to UV irradiation, but not developed (Fig. 3.5, step 2), so that film is covering the whole wafer with an equal thickness. Then, a UV-blocking 100 nm - thick aluminium (Al) film is evaporated (Leybold Optics LAB 600H, deposition at room temperature with a rate of 4 Å/s) on the top of first SU-8 layer (Fig. 3.5, step 3). Subsequently, a 1 μm-thick SU-8 layer is spin-coated on the top (Fig. 3.5, step 4), to act as a free-standing beam. Then the top layer is exposed, and both layers are developed in PGMEA, and aluminium film is etched in a standard AZ developer (Fig. 3.5, step 6). As a result, in the area where bottom part of SU-8 was unexposed, upon dissolving in the developing solvent it should act as a a sacrificial layer, and define the dimensions of the free-standing beam.
However, this resulted in wrinkle-like structure of the pattern (see Fig. 3.6). This probably

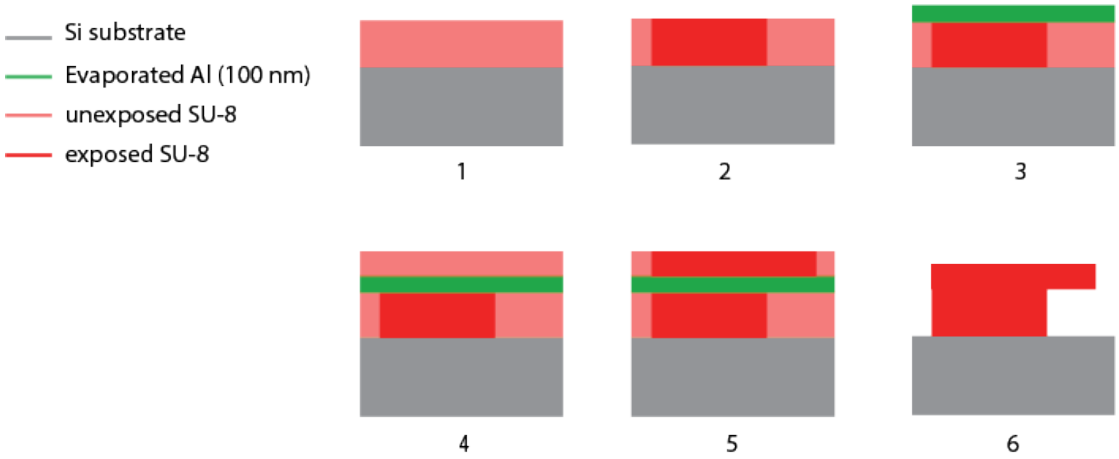

Figure 3.5: Schematics of the process flow of the double SU-8 layer approach. 1 - spin-coating 25 μm - thick SU-8, 2 - UV exposure of SU-8 (without development), 3 - evaporating 100 nm of Al, 4 - spin-coating 5 μm SU-8 - thick SU-8, 5 - UV exposure of the top SU-8 layer, 6 - development of both layers in PGMEA and wet etch of the Al film.

happened because the bottom SU-8 layer can be damaged by process of aluminum evaporation, that causes some heating of the substrate, and by the baking steps of the top SU-8 layer. It is complicated to work with not cross-linked (not yet developed) photoresist, since any heating can induce solvent evaporation. And indeed, it was reported that even evaporation of a very small metal quantity can trigger photoinitiation, cause unwanted cross-linking of the undeveloped bottom SU-8 layer, and wrinkle artifacts on the surface [Ceyssens and Puers, 2006].
This approach still could be interesting, because it does not need etching, but just a release by the developing the photoresist. However, further optimization of the process is required to get reproducible, good quality released SU-8 structures. In addition to that, light coupling is easier to do, when base is made from other material, otherwise coupled light can travel

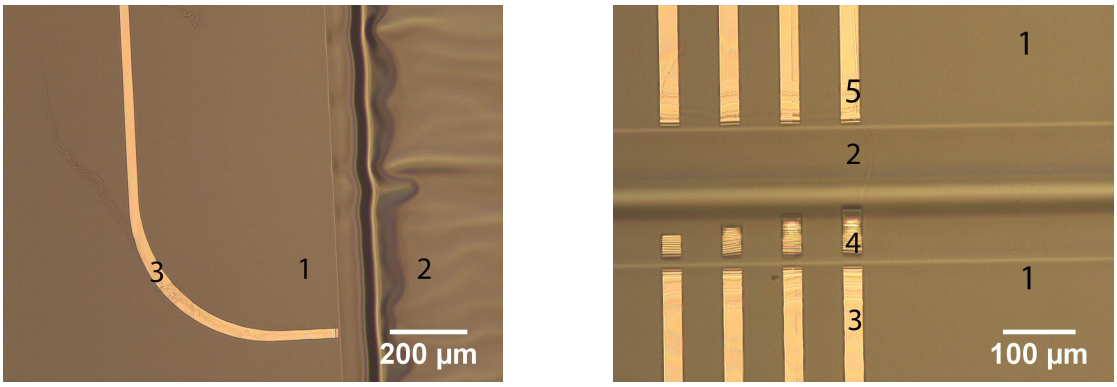

(a) (b)

Figure 3.6: Optical microscopy images of the double-layer SU-8 structures. (a) Single SU-8 structure: 1 - base of SU-8, 2 - wrinkle-like structure of protective aluminium layer, 3 - SU-8. (b) Array of the SU-8 structures for the efficiency coupling readout: 1 - polymer base (bottom layer of SU-8), 2 - gap between two parts of SU-8: the free-standing and non-free standing for coupling efficiency readout, 3 - part of SU-8 for guiding light towards the free-standing beams, 4 - the beams parts, that is to be released, 5 - output light guiding part.

inside SU-8 material in all directions, unless base is made from modified SU-8 with another refractive index. Therefore, the use of just one single SU-8 layer, and etching of the substrate, turned out to be a better solution, though it also has a number of challenges, such as adhesion of SU-8 to the surface, and stress that can be induced in the SU-8 during the etching process.

3.3.3 Wet etching for SU-8 beams release

Wet etching technique requires the use of aggressive solutions such as potassium hydroxide (KOH), and hydrogen chloride (HCl) for its neutralization. It requires a special care and the use of dedicated protective equipment. Similarly, wet processing might delaminate the SU-8 layer, in case of bad adhesion to the silicon and the silicon oxide surface. However, wet etching could allow to produce truly free-standing beams, that is harder to achieve with dry etching techniques. Also, in comparison with plasma etching, the SU-8 polymer should receive less stress.

Although free-standing beam is more fragile, it has a number of advantages: for example, both top and bottom surface can be observed with inverted optical microscope. Also, local attachment of the living organisms onto the free-standing lever is facilitated.

The KOH wet etch procedure is commonly used for the micro-fabrication of SiO_2 cantilever beams, but it also was demonstrated to be a convenient technique for fabricating polymer cantilevers. Normally, SU-8 cantilevers are made fully made from the same resist material. The base (body) and beam part are completely released from the silicon wafer during the KOH wet etch process. In this project, the goal was to fabricate cantilever beams located on the top of oxidized wafer without removing the SU-8 layer from the surface, where the oxidized silicon chip serves as a base for the cantilever.

The process flow includes steps of patterning SU-8 structure on the top of the double-sided oxidized wafer, and patterning an etching mask on the backside. Oxide on the topside should work as a cladding material, thanks to its refractive index, that is lower than refractive index of SU-8, and oxide on the backside of the wafer that works as a mask for the wet etching. To prevent the detachment of the SU-8 from the top side of the wafer, that is due to the underetch of silicon, the top side of the wafer was protected with PMMA chuck. However, the SU-8 does not adhere very well to silicon and silicon oxide surfaces, and therefore wet etching was a not feasible process, since SU-8 was swept during the KOH etching. To overcome these problems, some modifications of the process flow were implemented. One of these modifications consisted in the addition of a sputtered 500 nm - thick SiO_2 layer on the top of SU-8 as a protection. The duration of the wet etch was minimized by developing a hybrid etching strategy, that included both dry and wet etching techniques. At first, vertical dry etch from the backside, using Bosch process was conducted. After this process, only a depth of 50 μm of Si was remaining under the SU-8 beams. Then, these remaining 50 μm of silicon were etched using KOH etch.
A long hardbake of SU-8 prior to all the etching steps as included in the process flow to improve adhesion of the SU-8 to the wafer. Unfortunately, all these changes did not help to solve the adhesion problem of SU-8. Therefore, dry isotropic etch process was considered instead, without use of a wet etch.

3.3.4 Dry etching for the SU-8 beams release

The operating principle of nanomotion sensor devices consist in monitoring the oscillations of a beam with adsorbed living organism. Since there is no need to approach these beams to other surfaces as in traditional Atomic Force Microscopy (AFM), the beams can be suspended above an etched cavity, instead of being completely released. This can partially protect chips from accidental breakage, and also opens the possibility of placing the microfluidic channel on top of the substrate. Etch of the cavities can be conducted by isotropic SF6 (sulfur hexafluoride) inductive-coupled plasma (ICP) etch (Alcatel AMS 200 SE etching machine).
The use of the dry etch processing is safe as does not require handling dangerous acid and base solutions, and minimizes the chances of SU-8 delamination from the surface, that could happen when wet etch process is used. However, it has also disadvantages: cavity geometry does not allow to observe the bottom surface of the beam, there is a risk of having air bubbles in the cavity, if it is not deep enough. Also, the use of the plasma etch inevitably induces stress to the SU-8, that can lead to the bending of the beams, or even their breakage, if the etching is performed for too long time, or with a too high power. This effect can be reduced by using hardbake of the SU-8, prior the etching process, by using a lower power and limited etching time. In particular, in this work the following parameters of the inductive-coupled plasma (ICP) etch process were used : SF6 flow rate of 50 sccm, and ICP source power of 1000 W, that give less aggressive etching than parameters of the standard isotropic etch recipe (SF6 flow rate of 300 sccm, and ICP power of 2000 W). SU-8 beam can be protected by additional SiO_2 layer. However, bending can not be completely avoided, since SU-8 is a material with a very

low thermal conductivity, and is sensitive to the thermal stress. The optimized process flow, that was used for fabricating the final version of the devices, is presented at Fig. 3.10.

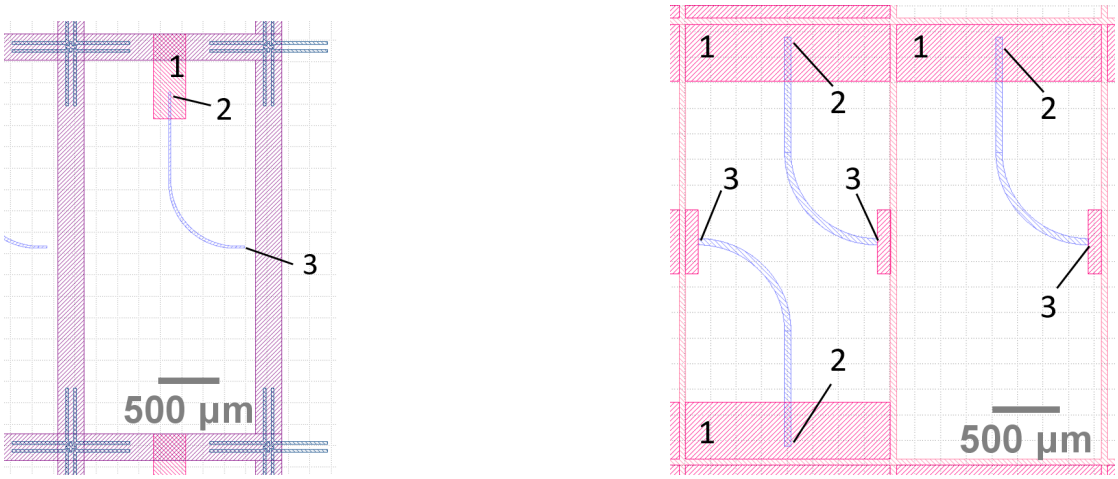

(a) (b)

Figure 3.7: Designs of the optical cantilever devices for the dry etch approach: (a) with a rectangular etching window for cantilever beam release, and (b) an optimized version of the device design with an etching window of whole chip width for cantilever beam release, and additional, 500 μm wide etch window to facilitate light coupling. 1 - etching window for cantilever release, 2 - end of the beam to be released, 3 - light entrance.

Cantilever sensors were fabricated on a 4-inch 525 μm - thick Si wafer with a wet grown 2 μm - thick oxide. To improve the adhesion of the SU-8 layer, we carried out oxide plasma treatment (Tepla 300) for 7 minutes at power 500 W, O_2 flow 400 ml/min and HMDS (hexamethyldisilazane) vapour treatment before the spin-coating step. SU-8 polymer was spin-coated on the pre-treated Si wafer at 1307 rpm for 40 seconds (Sawatec LSM 250), to have 5 μm-thick film of SU-8 (SU-8 GM 1050 photoresist, Gersteltec Engineering Solutions, Pully, Switzerland) on the wafer surface (Figure 3.10, step 2). The SU-8 layer thickness was later confirmed by optical microscopy and white light interferometry (Bruker Contour X) (Fig. 3.3b). After the spin-coating step, the SU-8 was softbaked at 90 C°, and eventually exposed to UV using maskless lithography (Heidelberg MLA-150). All patterning masks were designed with KLayout Editor open source software. SU-8 was exposed with UV light of wavelength 375 nm, dose 390 mJ/cm^2. After exposure, it was baked at 120 C°, and developed in propylene glycol methyl ether acetate (PGMEA) solvent, then hardbaked at 150 C° (Figure 3.10, step 3) to reduce stress in the SU-8 material, improve adhesion and uniformity of the SU-8 layer [Li, 2018; Keller et al., 2010]. All baking steps were done with a ramp slower than 2 C°/min to minimize the thermal stress, and followed by at least an overnight relaxation before the subsequent exposure or development steps.
An 500 nm thick SiO_2 layer was sputtered on the wafer using a deposition tool (Pfeiffer SPYDER 600) with a source power of 1000 W, at a deposition rate of 58 nm/min (Figure 3.10, step 4). This oxide layer was used as a mask for the dry etching step of Si. To pattern this etching

mask, 1 μm - thick resist layer was spin-coated (AZ ECI 3007, Merck) at automatic coater Süss Microtech ACS200 Gen3 with ramp speed 850 rpm, and 2 min softbake at 100 C° on top of the SiO_2 (Figure 3.10, step 5). The resist layer was then exposed to UV light using a mask-less lithography aligner (Heidelberg MLA 150) at a dose of 210 mJ/cm_2, and a wavelength of 405 nm (h-line), and developed in ACS 200 machine, with a post-exposure bake at 110 C° (Figure 3.10, step 6).
The SiO_2 was etched using inductively coupled plasma (ICP) -based etching machine (SPTS APS), that permitted to open windows for isotropic dry etching of the Si surface (Figure 3.10, step 7). After the AZ ECI resist stripping (Figure 3.10, step 8), the wafer was coated with a thick

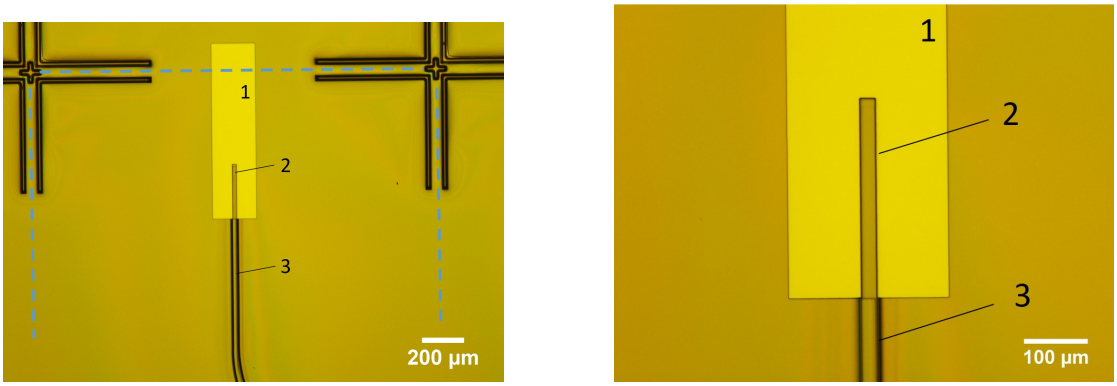

(a) (b)

Figure 3.8: Optical microscopy images of the SU-8 structure on the Si substrate and SiO_2 etch mask, that determines the length of the free-standing beams. 1 - etch mask window, 2 - part of the SU-8 structure to be released, 3 - light guiding part of SU-8. Position of the subsequent dicing cut is shown as a blue dotted line.

protective resist (AZ 40XT, Merck) layer (Figure 3.10, step 9) and diced with a 50 μm - wide cut (Disco DAD321 dicing saw machine). The dimensions of the obtained chips were 3.4 x 1.6 mm. Eventually, the chips were mounted on a dummy oxidized wafer ((Figure 3.10, step 10a) and loaded inside an Inductive Coupling Plasma dry etching machine (Alcatel AMS 200 SE). Isotropic fluorine plasma etch was performed with the following parameters: SF_6 gas flow of 50 sccm and ICP power of 1000 W. During this process, the two free-standing SU 8 beams were released (the mechano-sensor (see Fig. 3.9) and the light-coupling end) by etching two 100 μm deep cavities underneath the SU 8 layer (Figure 3.10, step 11).
The single chips were dismounted from the wafer and cleaned in acetone, 2-propanol, and DI water. Finally, to remove the residues of SiO_2 under the free-standing beam, the chips were loaded in the HF vapor isotropic etch machine (SPTS μEtch, used pressure of 125 Torr).
To confirm the release of the SU-8 cantilevers from the chip, as well as to confirm quality of the beam surface, chips were studies with Scanning Electron Microscopy (SEM). To avoid charging effects, chips were coated with a 5 nm/ 20 nm of Cr/Au, prior to the loading in the SEM. The 30 ° tilt of the stage permitted to confirm that the beam was successfully released from the surface (see Fig. 3.12). Study of the SEM images showed that SU-8 beams had vertical walls. Small artifacts, that were observed in the some spots on the beam surface (Fig. 3.12b),

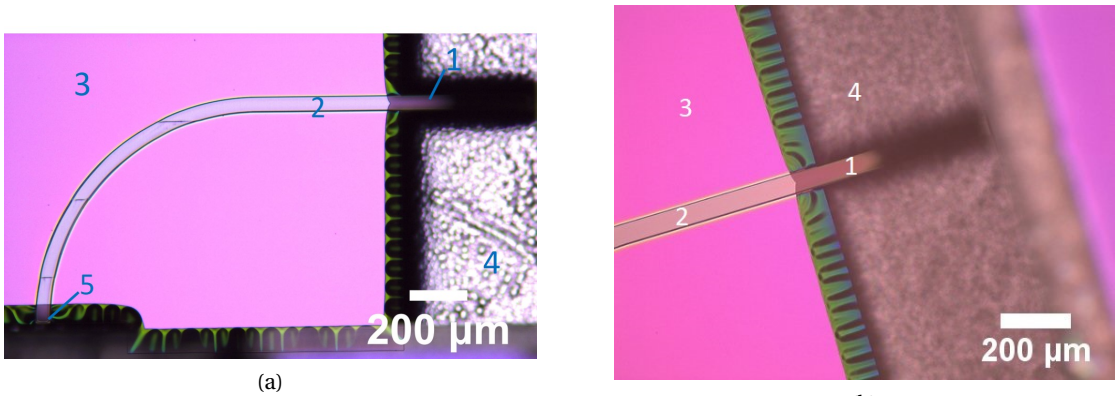

(a) (b)

Figure 3.9: (a) Chip with SU-8 light guiding structure and (b) released beam after dry etch (optical microscopy). 1: suspended beam (partially out of focus due to the bending), 2: light guiding part of SU-8 (not released), 3: SiO_2 mask, 4: etched Si cavity, 5: spot for coupling light in.

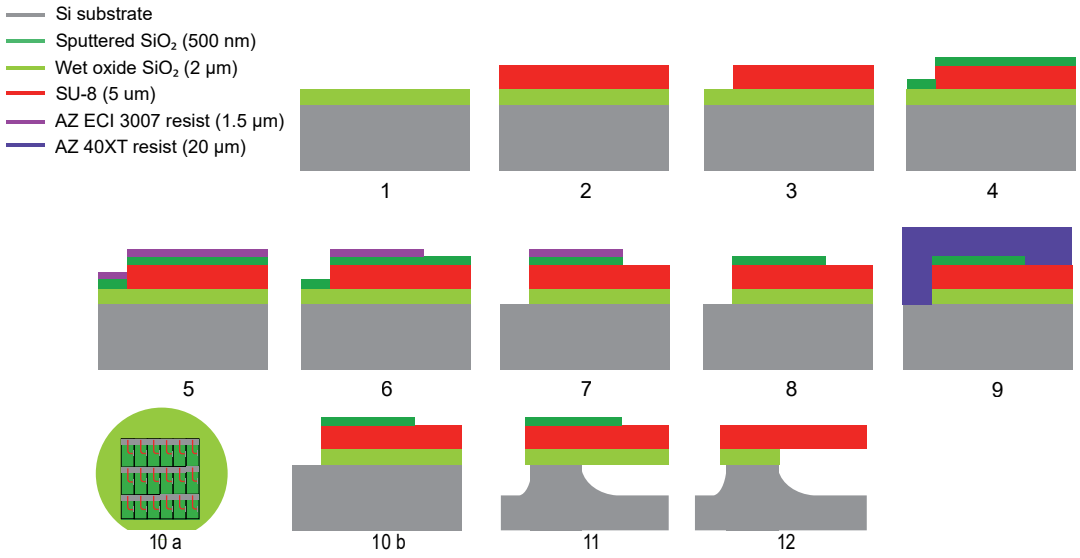

Figure 3.10: Process flow for fabricating suspended SU-8 levers: 1. Si wafer with 2 μm SiO_2 Wet oxide, 2. spin-coating of 5 μm-thick SU-8 layer, 3. Exposure and development of SU-8 structures, 4. Sputtering 500 nm thick SiO_2, 5. Spin-coating 1.5 μm thick $AZECI3007$ resist, 6. Exposure and development of resist, 7. Plasma Etch of SiO_2, 8. Removing resist, 9. Spin-coating protective resist for dicing, 10. Dicing, removing protective resist, and attachment of diced chips to the dummy oxidized wafer (a: top view of the chips attached to the dummy wafer, b: side view of single chip), 11. Dry isotropic etch of the Si substrate, 12. HF vapour isotropic etch of silicon dioxide.

were most likely caused by the bubbles during resist coating.

One of the drawback of the proposed process flow is the bending of the beam, that can have positive (upwards) or negative (downwards) sign, depending on some steps of the process flow:

we have observed a downwards bending for the chips with 2 μm thermal oxide (see Fig. 3.11a), and an upwards bending (see Fig. 3.11b, Fig. 3.12) for the similar process flow, in which the silicon wafer did not have a thermal oxide. This bending is likely related to the intrinsic stress in SU-8 polymer, and is affected by the following heating steps: softbake, post-exposure bake (PEB), hardbake, as well as by the UV exposure dose [Li, 2018; Keller et al., 2010] and the plasma etching of the SiO_2 film and the Si substrate. Difference in the bending between two process flows can be explained by a bi-material effect of the SU-8 and the SiO_2 that exists in case of the wafer with a thermal oxide: in this process SU-8 beam is being release with an oxide layer under it (Fig. 3.10 (11)). Another phenomenon that can induce a stress in the structure is a duration of the SiO_2 etch: in case of the process flow with Si wafer without an oxide, only a 500 nm - thick mask has to be etched to open the mask windows, but in case of the process flow with 2 μm thick oxide, the total thickness of oxide is bigger, and therefore there is a higher amount of energy that is received by SU-8. This bending can be reduced by further optimizing the process flow, for example, by protecting beam with an additional oxide layer from the plasma ions during etch. However, in spite of these bending effects, cell attachment, light coupling and optomechanical measurements were performed successfully (see Chapter 4).

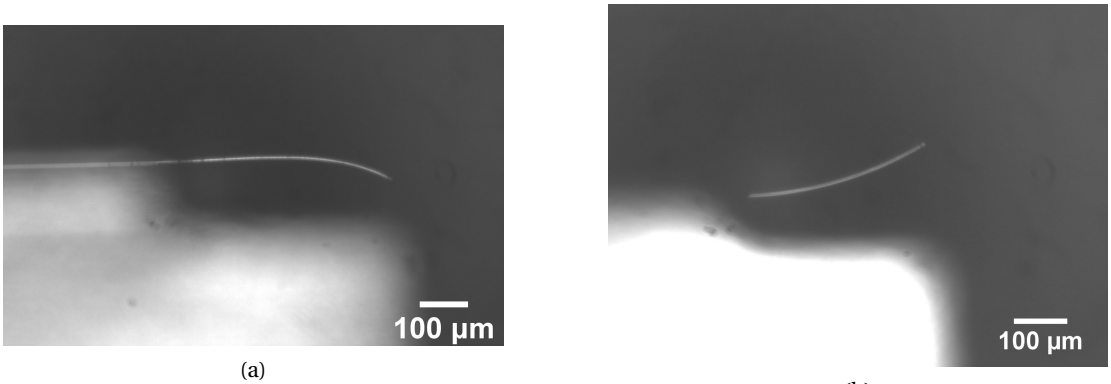

(a) (b)

Figure 3.11: Bending of the released cantilevers beam (optical microscopy, imaged from the side).

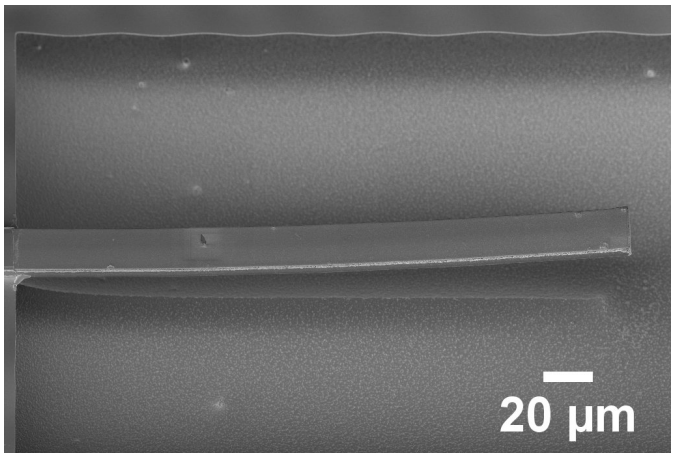

(a)

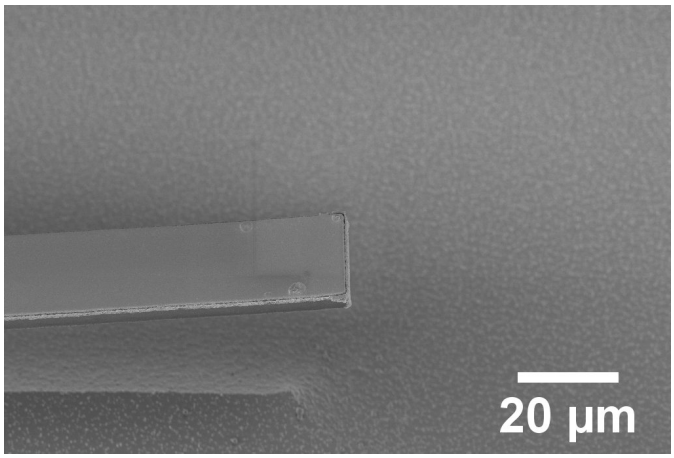

(b)

Figure 3.12: Scanning electron microscopy (SEM) image of the released SU-8 beam, patterned on the Si chip. Image was obtained using 3 kV voltage, with a tilt of the stage 30 °.

3.4 Developing the measurement setup. Light coupling and signal recording

3.4.1 Setup for optomechanical measurements and tests

An experimental optomechanical setup was assembled on an optical table. It consists in vertical and horizontal optical microscopes, micromechanical manual stages, a laser source and a measurement chamber (liquid cell) (Fig. 3.16). Two micromechanical stages move the measurement chamber and the laser source together, without de-coupling light from the setup. They also allow to focus vertical observational microscope, move horizontal readout optical microscope (Fig. 3.13b) in XYZ directions, and perform alignment and focusing of the laser source (Fig. 3.16). The vertical microscope serves for the observation of the surface of the chips, alignment, and to confirm the presence of the living organisms on the cantilever.

The horizontal readout microscope records output signal, and permits to further verify light coupling and alignment. Both microscopes are equipped with high-speed CCD camera. In addition to that, the readout optics consists in a beam-splitter, and an attached 4-segment photodetector with an amplification board (Fig. 3.13a, Fig. 3.13b). This allows to control the coupling and to record the signal with the CCD camera and the photodetector simultaneously. The use of the CCD camera is opening the opportunity for using multi-sensor array devices in the future. However, the camera was mostly used for alignment purposes, and all the recordings were made with the photodetector, since it allows the recording of the signal at a much higher frequency.

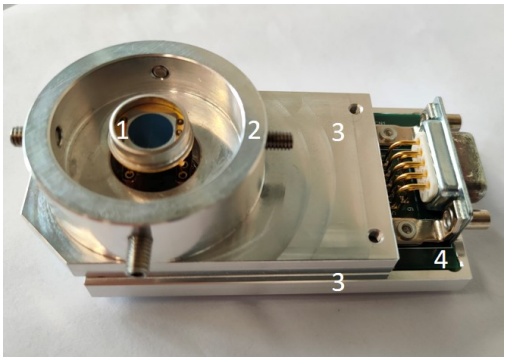

(a)

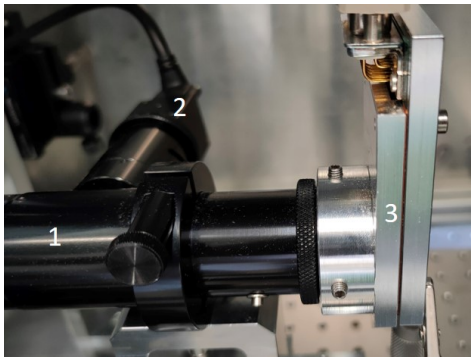

(b)

Figure 3.13: (a) Photodetector on the amplification board: 1 - 4-segments photodetector, 2 - mounting ring for the attachment to the optical tube, 3 - shielding metal plates, attached from both sides to the amplification board, 4 - amplification board. (b) Readout optics: 1 - Optical tube with the beam splitter, 2 - CCD camera, 3 - photodetector board in the shielding metal cage.

To permit an easy alignment of the light source onto the chip, and perform reliable recordings, it is important to mechanically stabilize the chip in the system. For this purpose, a special measurement chamber was designed. This chamber was made from the stainless steel with thin glass windows to couple the light from the laser source to the SU-8 structure, and record the output light spot with the readout optics. The metal holder for the cantilever chip (Fig. 3.14) is magnetically attached inside this metal chamber (Fig. 3.17), and centered using special alignment balls. This ensures that both light entering and exiting ends of SU-8 are located approximately in the middle of the glass windows. The measurement chamber is also magnetically attached, on the top of a rigid fixture with an integrated piezo-actuator. These magnetic attachments help to position the chip in almost the same place, and therefore only slight adjustments of the micromechanical stages are required for the light alignment.

A piezo-actuator, that is located under the measurement chamber, helps to drive the whole chamber in oscillation with a chosen amplitude and frequency, in order to assess the cantilever displacement. The piezo-actuator was used at the low amplitudes of its working range, a domain where its response is approximately linear. Its calibration was performed using an

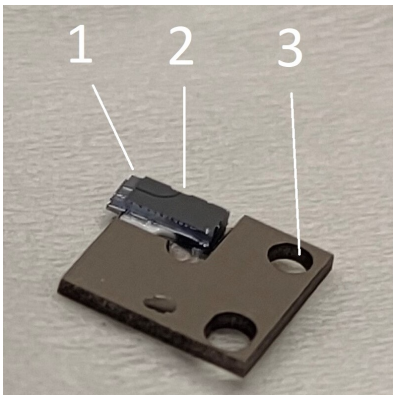

Figure 3.14: The cantilever chip, manually glued to the metal holder, that can be magnetically attached to the measurement chamber. 1: etched cavity with suspended beam, 2: spot for coupling the light in the chip (in the middle of the right side of the chip), 3:holes that are later placed on the alignment balls for centering the position of the holder in the chamber.

Atomic Force Microscope (AFM). For this calibration, the AFM cantilever was approached to the piezo-actuator, that was excited using a wave generator. Scans were recorded without moving the AFM cantilever beam in the lateral direction, but by just following the vertical oscillations of the piezo, so that the XY directions of the scan represented oscillation in time (see Fig. 3.15). This test was later confirmed by alternative calibration, that was made using a laser Doppler vibrometer device. The piezo-actuator was used to test sensitivity of the developed setup to nanometer-scaled oscillations at low frequencies, and to calibrate its response.

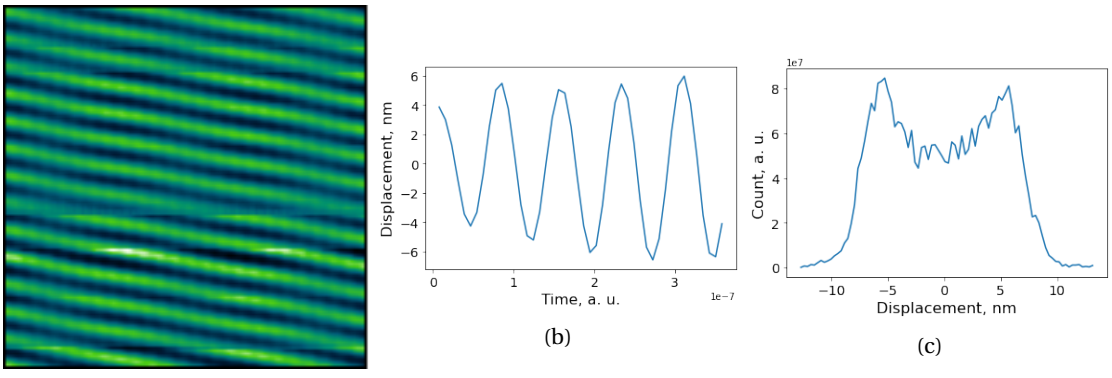

(a) (b) (c)

Figure 3.15: Calibration of piezo with AFM: (a) AFM image that is performed by keeping the AFM cantilever in the same spot. Periodic stripes represent oscillations of the piezo-actuator. (b) Profile of the cantilever motion that follows low-frequency oscillations of the piezo, and (c) Histogram of the height distributions of the AFM scan. Positions of the peaks can be used to determine amplitude of the oscillations: here ~ 5 nm.

One also have to keep in mind, that since the whole chip is driven into oscillations, there is an effect of changing the light coupling efficiency, in addition to displacement of the light spot.

But this effect can be taken into account by normalizing differential signal of the photodetector over the total signal, defined by the intensity of the light spot.

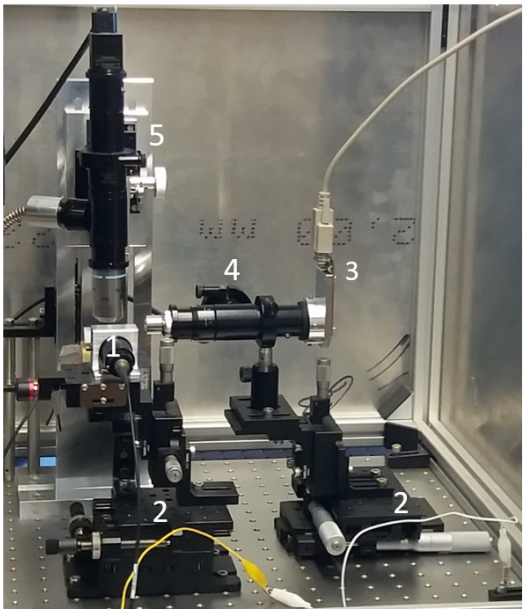

Figure 3.16: Measurement setup for the optomechanical measurement, assembled on the optical table: 1 - Laser fiber-coupled low coherence beam source of 636 nm wavelength and 2.5 mW power, 2 - micromechanical stages for the light alignment, 3 - photodetector with amplification board, 4 - readout optics with beam splitter, CCD camera (behind), 5 - observation optics with CCD camera.

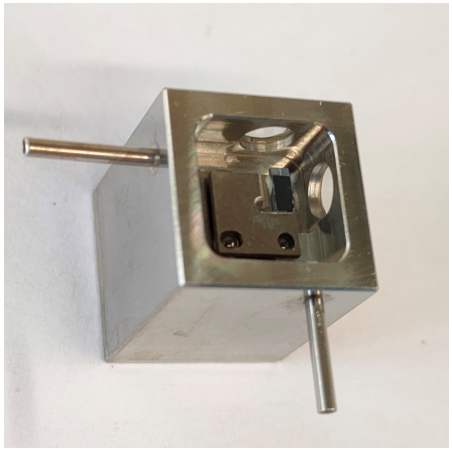

Figure 3.17: Measurement chamber with cantilever chip fixed on magnetically attached holder. Thin glass windows allow to couple light -in and -outside of the chip. Metal tubes can allow automatic liquid handling.

3.4.2 Light coupling procedure

The light coupling procedure consists in observing the chip with a microscope, and in moving the light spot in a position where it hits the end of the SU-8 structure (Fig. 3.18a), and focusing light into smaller possible spot. The fiber-coupled low coherence beam source of 636 nm wavelength and 2.5 mW power (51nanoFCM, Schäfter + Kirchhoff GmbH, Germany) had an integrated micro-focus generator with working distance of 54 mm. An alignment and focusing of the light were performed by using the XYZ micromechanical stage, on which the laser source with a focusing optic was firmly attached (Fig. 3.16, 1).
The readout optics is aligned to focus on the edge of the cantilever beam that is suspended in the middle of the etched cavity. When the laser light is on, the light is coming out the end of the cantilever (Fig. 3.18c, Fig. 3.18b). The position of the laser source can again be slightly adjusted, until the light spot, coming from the beam reaches its highest intensity. This is assessed by maximizing the SUM signal of the 4-segment photodetector.

Finally, the position of the readout optics has to be slightly re-adjusted in order to obtain a laser light spot, that is centered between the 4 photodetector segments. Because the CCD camera field of view, and photodetector have some offset, and also do not have the same sensitive area, this readjustment is crucial to position the light beam in the middle of the photodetector, in a way that each segment has an equal signal. However, because the plane of the photodetector is not perfectly vertical, and the chip is also not perfectly aligned relatively to the optical path of the readout microscope, there is some slight variation between the single segment signals.
Alignment stages have some mechanical drift, that can be visible during long lasting recordings. Therefore, it is important to control the level of the signals, and to correct the alignment in between the recordings, if necessary.

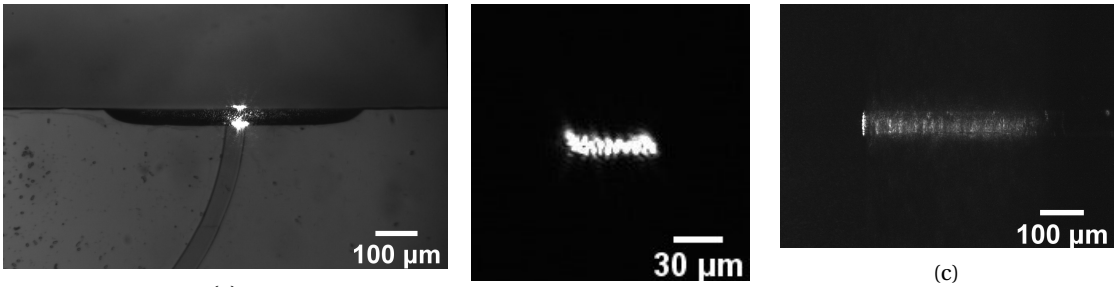

(a) (b) (c)

Figure 3.18: Optical microscopy images of the light that travels through the SU-8 microstructure. (a) Coupling the light into the chip: the laser spot is focused at the inlet of the light guide (top view), (b) light spot that comes out of the free-standing beam (side view), and (c) light that travels through the free-standing beam (top view).

3.5 Signal amplification and data acquisition system

The photodetector amplification board consists in a transimpendance amplification, and a voltage amplification stage (see details in section 2.5.2 and Fig. 2.5a, Fig. 2.5b). To minimize the noise, that depends on the feedback resistors of the amplification scheme, most of the gain is given by the transimpendance amplification stage, that has a noise $\sim \sqrt{R_f}$, where R_f is the value of the feedback resistor. An amplification board that was used for initial optomechanical measurements and resonance frequency measurement, had gains of $G_1 = 10^6$ V/A, and $G_2 = 10$ on its amplification stages, resulting in total gain of $G = 10^7$, and bandwidth of 100 kHz. This frequency bandwidth was enough to cover the resonance frequency range of the fabricated SU-8 beams. Second board had gains of $G_1 = 10^6$ V/A and $G_2 = 100$, resulting in total gain of $G = 10^8$, and bandwidth of $f = 5$ kHz respectively, and was used to perform viability cell tests. The signal that is relevant in the biological experiments, is confined to the low-frequency region, below few hundreds of Hz. Therefore, to improve the signal-to-noise ratio and avoid aliasing effects (effect of the higher frequency region on the frequencies inside the acquisition frequency band), a low-pass RC filter, that cuts the signal at a frequency above 5 kHz, was

included in the board with $G = 10^8$. The gains were chosen to have high enough signal without saturation. The amplifiers gain is defined by the values of the feedback resistors. Their value is a compromise between the desired gain and the value of the Johnson-Nyquist noise. There was no DC (high-pass) filter used, to avoid cutting relevant low-frequency signal. In addition to this, DC level of the signal was required to perform light alignment, that was achieved by maximizing the DC signal of the photodiodes.
The amplification board and the data acquisition system were developed to permit an access to the signal of each photodetector segment, called as A, B, C and D (see Fig. 3.1). These signals were recorded by the NI acquisition board, with the use of NI Labview software, with a 30 kHz acquisition frequency. The acquisition board allows recordings up to 102.5 kHz, but a lower rate was chosen for the sake of data storing and analysis , since the relevant biological signal lies in the frequency region below 1 kHz.
The photodetector board is covered with a metal shield (see Fig. 3.13a), to minimize the effects of electromagnetic fields. To minimize the ground loop, as well as for safety reasons, the shield of the amplifier board, as well as the vibration isolation table, are connected to the ground of a power supply. A DC voltage of 15 V is supplied to the amplifier board as power supply and as a reverse bias voltage of the photodiodes. Applying reverse bias voltage allows to decrease the photodetector the photodetector capacitance and hence to increase the photodiode frequency width. However, this was crucial mostly for the measurement of the resonance frequency in air, when a high acquisition bandwidth was required.
As in conventional AFM detectors, the vertical oscillations of the cantilever was extracted from the difference between signals, provided by the top and bottom part of the photodetector, normalized over the total signal:

$$V_{diff-norm} = (V_{TOP} - V_{BOTTOM}) / V_{SUM} = \frac{(V_B + V_C) - (V_A + V_D)}{V_A + V_B + V_C + V_D} \tag{3.1}$$

A dedicated data acquisition Labview software records independently the signal of each photodetector segment, with a chosen data acquisition rate, and plots each signal in real time, as well as the SUM, TOP-BOTTOM, and LEFT-RIGHT signals, and the spectra curve of the TOP-BOTTOM signal. At the beginning of each measurement, the signal that is recorded in the 'dark state', when laser is off, is subtracted from the signal. This permits to asses the correct level of the signals. It is especially important when signal level is low. In addition to this subtraction, that is made before starting the measurement with turned on light, a short recording is also carried on upon switching the laser light off and on (see Fig. 3.19). This is an additional check, that permits to asses that dark state offset is corrected, the received laser light is stable, and the light spot is located approximately in the center of the 4-quadrant photodetector .
After two stages of amplification, the photocurrents of the diodes result in negative voltages (Fig. 3.19). The higher light intensity results in a higher absolute value of voltage signal (i.e., more negative voltage).
For a given displacement, the response of the sensor $V_{TOP} - V_{BOTTOM}$ is proportional not only to the value of displacement, but also to the total light intensity. The goal of the signal

normalization over its sum (Eq. 3.1) is to take into account the variation of the total light intensity. Most of the data analysis and visualization was conducted with help of the Python

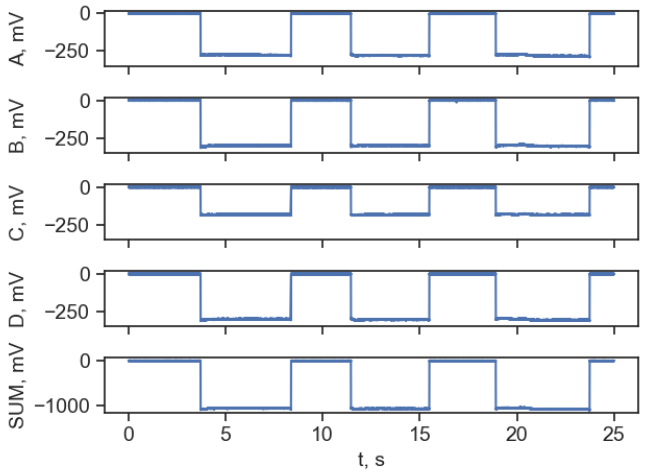

Figure 3.19: Typical photodiode signals and their sum, when light source is switched -off and -on. Dark photodetector represents 0 level of the signal, and laser illumination gives a negative voltage for each of the segments. The total gain is 10^8 V/A (10^6 V/A $\cdot$ 10^2 V/V).

scripts that were developed by me during the work on this thesis. The data processing and interpretation of the results will be discussed in details in the Chapter 4

3.6 Conclusion

In this chapter, the design of the optomechanical diagnostic device for the live cell viability test was presented. It consists of a SU-8 light guide that has a free-standing end, a light coupling system, a 4-quadrant photodiode with an amplification board, and a data acquisition system. Three approaches for the release of the SU-8 cantilever beam have been considered: using a second layer of SU-8 as a sacrificial layer, wet etching, and dry etching. Among all of them, the dry etching approach was the easiest to implement. The assembled experimental setup allows to couple light in the chip, and perform optomechanical measurement in air and liquid medium. Further characterization of the microfabricated sensors and their use for live cells viability tests will be presented in the chapter 4.

4 Experimental results

4.1 Introduction

This chapter starts with the description of the light coupling procedure, and initial tests of the fabricated chips, the readout of the oscillation driven with piezo-actuator, the measurement of the power spectra and resonance peak of the cantilever beams in air, and the comparison of the experimentally measured and design values. The spring constant of the cantilever is estimated using experimentally measured spectra.
Next, the cultivation of the *S. pombe* yeast cells, that were used as a test organism for the viability test is described. After the explanation of the cells attachment to the cantilever surface, the results of the nanomotion measurements are presented. Finally, the processing of the data, and various effects that contribute to the sensor response are discussed.

4.2 Light coupling and beam response tests

A good light coupling is a crucial step to obtain a stable and reliable signal readout. Since the coupling efficiency of the fabricated SU-8 structures was low (having total losses of about 30 dB to 50 dB with respect to the power of light source) it was important to optimize the light coupling procedure. However, the light coupling is also affected by the slow drift of the micromechanical stages, and the acoustic noise that can not be completely suppressed by the vibration isolation table. Those effects can be visible in the raw signal, such as the slow drift of the signals and spikes. Both effects can be partially corrected during the post-processing step. In addition, the levels of the signals are checked in between of the recordings, and if needed, a slight correction of the alignment is performed.
After assessing a good light coupling in air, water, and YPD medium for yeast cell measurements, the cantilever chip was driven into oscillations. The main goal of these actuation tests was to demonstrate the ability of the system to detect nm-scale displacement. The results of these tests were as well used for the conversion of the photodetector's signals to nm, which is about 0.1 mV/nm per 1 V of total signal at the amplification gain of 10^8 V/A.
During this procedure the whole chamber was driven to oscillations with amplitudes from few nm to few tens of nm and frequencies from few Hz to few hundreds of Hz. The oscillations were assessed by the photodetector signal in time domain (see Fig. 4.1), as well as by the

power spectral density (PSD) curve (see Fig. 4.2). The described method to drive the cantilever into oscillations, has to be used with care, because it causes whole chip to oscillate, and this might cause a change in the coupling efficiency. A possible change in the coupling efficiency is taken into account by scaling the differential signal over the sum of. The piezo actuator was operated up to few tens of nm (i. e., well within its linear region) and at frequency up to 300 Hz (i. e., well within its flat frequency response).

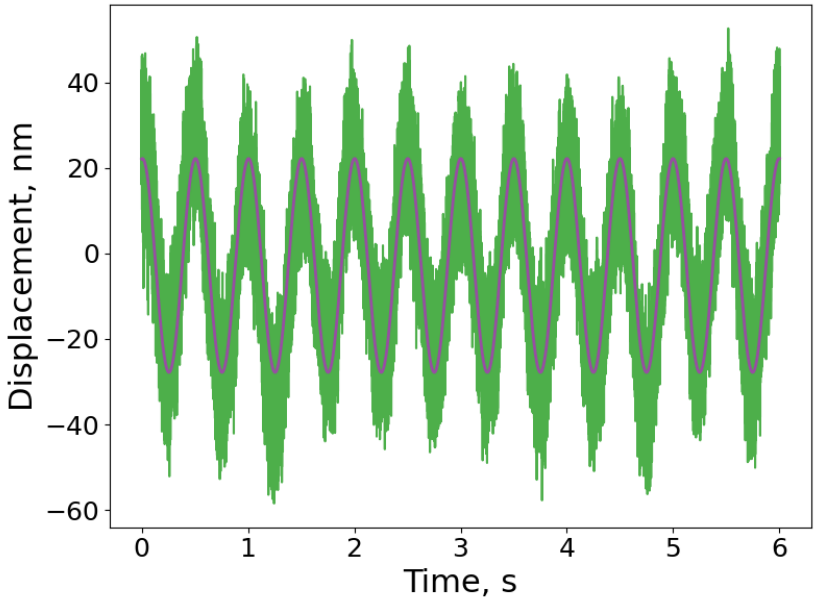

Figure 4.1: Displacement signal (green) of the cantilever chip immersed in the YPD medium, driven into oscillations with a piezo-actuator at amplitude of 25 nm, 2 Hz frequency, and the sine fit (violet) of this signal.

In addition to driving oscillations of the chip, displacement tests were performed by moving the readout optics (see Fig. 4.3). These tests have the advantage of not influencing the coupling at all, and confirming that in such case the sum of the segments signal remains constant. However, since the readout optics was bulky, there was no automatic driver implemented, and this displacement test was made by simply moving the optical tube with the micromechanical stage. Because of this, the value of displacement is few micrometers, as the stages hardly allow to have smaller displacement than 1 μm. This motion is a simple displacement, i.e., linear translation, instead of periodic oscillation that was made in case of the use of the piezo-actuator.

The noise provided by a system with a free-standing beam in air and immersed in YPD medium, was well recorded, and scaled to nm using a previously obtained calibration of the measuring system (Fig. 4.4). This scaling is permits to estimate a change in the oscillation amplitude during nanomotion viability tests that are described in the section 4.6. However, the noise that is measured for the non-actuated beams represents not only mechanical fluctuation of the beam, but is also an electronic noise coming from the amplification circuit. According to the previously made estimates (see section 2.5.2 and Eq. 2.27) and conversion factor of

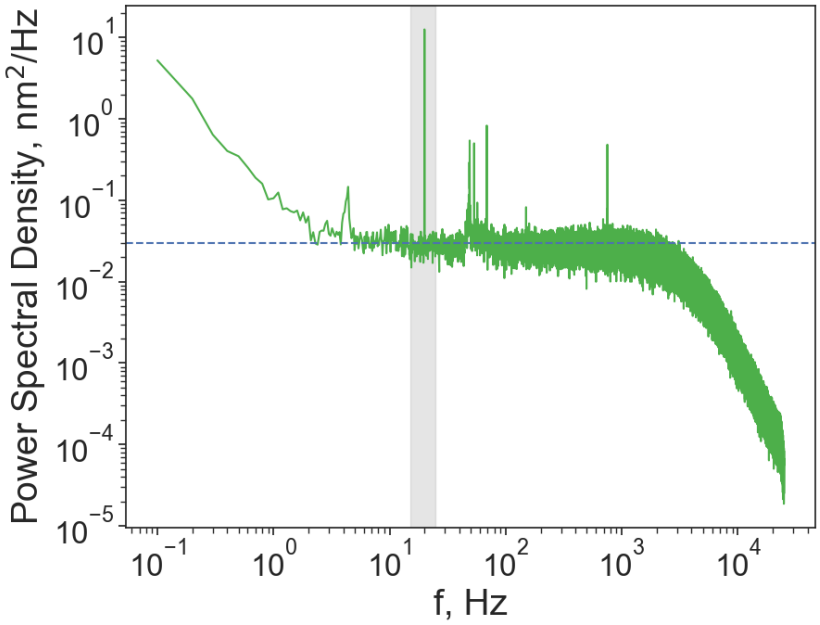

Figure 4.2: Power spectral density of the cantilever, driven into oscillations with a piezo-actuator at amplitude of 5 nm, 20 Hz frequency. The peak position that corresponds to this oscillation is highlighted in gray. The white noise region corresponds to a power spectral density of about 0.03 nm^2/Hz (blue dotted line).

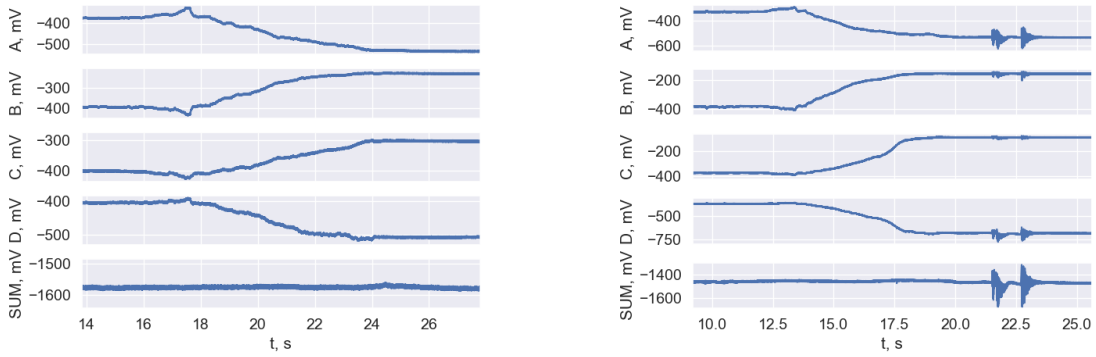

(a) 3.5μm vertical shift

(b) 6μm vertical shift

Figure 4.3: Response of photodetector segments signal to manual vertical translation of the readout optics of 3.5 μm (a) and 6 μm (b). Translation is made with graduated micromechanical stage.

0.1 mV/nm, electronic noise can give at least $\frac{2.7\,\text{mV}}{0.1\,\text{mV/nm}} = 27$ nm of rms noise, which agrees with recorded signal (Fig. 4.4).

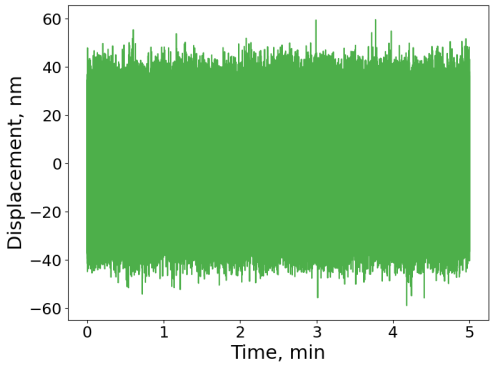

Figure 4.4: Noise that comes from the non-actuated cantilever beam, scaled to nm displacement.

4.3 Resonance spectra of the fabricated beams in air

The theoretical spring constant and resonance frequency of the SU-8 cantilevers was calculated and presented earlier (see Chapter 2). Although the application of the fabricated beams is based on the activity of the beams at low frequencies (i. e. well below their resonance), it was important to verify that the stiffness of the beams corresponds to the expected values. To maximize the signal that is received by the readout optics, a 40x objective with a 0.6 mm working distance was used. As in all other experiments, the light spot was aligned in a way to receive a similar response on all the 4 photodetector segments, and to maximize their sum. The recording was done at a 50 kHz acquisition rate, to cover the range of predicted resonance frequencies of the SU-8 beams.
A 5 minute long recording was then split into 1 second long chunks, the Power Spectra Density estimate was calculated and averaged for each of them. The position of the resonance peaks, that was measured using NI data acquisition board (Fig. 4.5a), was as well validated (Fig. 4.5b) with analog FFT spectrum analyzer (SR760).
The experimentally estimated position of the resonance peaks (Fig. 4.5a, Fig. 4.6) is in good agreement with the theoretical values (Fig. 4.7), calculated assuming a Young's modulus of 5 GPa for SU-8.
To determine the position of the resonance peak and its quality factor, the observed resonance peak was fitted (Fig. 4.6) with a Lorentz curve (Origin Pro, OriginLab). For the 400 μm , 500 μm and 650 μm - long beams of 5 μm thickness and 50 μm width this fitting gives a resonance peak at $f_{res-exp-air-400} = 11.2$ kHz, $f_{res-exp-air-500} = 6.4$ kHz and $f_{res-exp-air-600} = 3.5$ kHz respectively, and similar quality factor of $Q = \frac{f_{res-exp-air}}{\triangle f} \sim 18$. The experimentally measured power spectra can be used to verify the spring constant of the fabricated cantilever beams. The most common methods to do so include the thermal calibration method, the Sander's method, and using the Hook's law. Let's us consider at first the latter one.
$\omega = \sqrt{\frac{k}{m_{eff}}}$, and $\omega = 2\pi f$, so the spring constant is $k = 4\pi^2 f^2 m_{eff}$, where m_{eff} is the effective mass of the beam that can be defined as $m_{eff} = 0.24 t w L \rho$, l is the length of the beam, w is its width, t is its thickness, and $\rho = 1200$ kg/m^3 is the density of SU-8. The experimentally

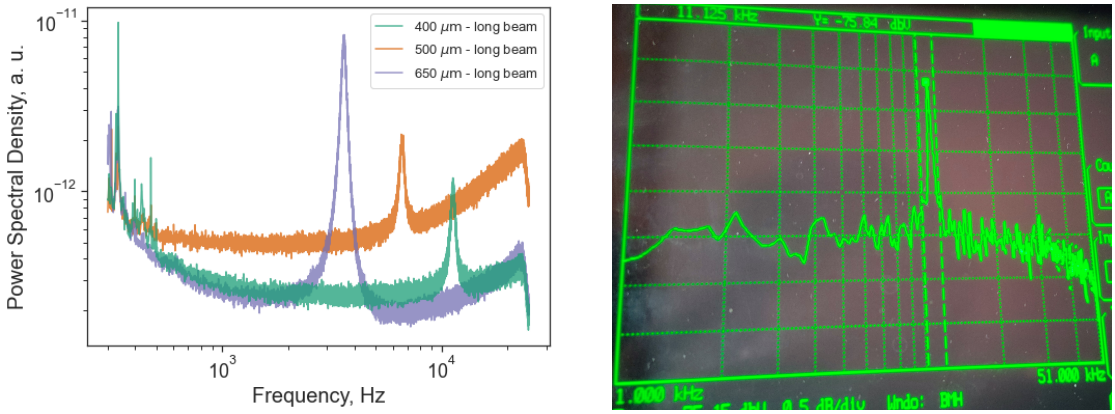

(a) (b)

Figure 4.5: (a) Power spectral density (PSD) of the 5 μm thick, 50 μm wide SU-8 beams with lengths of 400 μm, 500 μm and 650 μm, and (b) spectra of the 400 μm long beam, measured with FFT analyzer with resonance peak at 11.1 kHz.

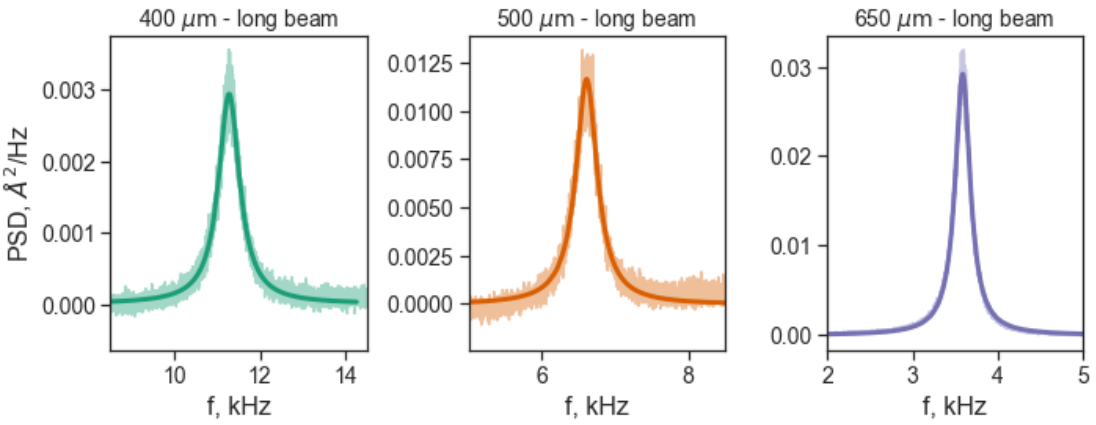

Figure 4.6: Resonance peak and Lorentz fit of it for beams with a length of 400 μm, 500 μm and 650 μm.

measured resonance frequencies gives the following spring constants: $k_{400\mu m} = 0.14$, $k_{500\mu m} = 0.06$, $k_{650\mu m} = 0.02$. These values fit well with the theoretically calculated ones (Fig. 4.7). The thermal calibration method needs an accurate calibration of the power spectra in nanometers, using an experimentally measured conversion factor. In the commercial AFM this procedure is typically performed by scanning the calibration microarray sample.In this work, the calibration of the system was conducted by exciting the cantilever with a piezo linear actuator (PL 088.3, PI Ceramic, Germany) at low frequency (far from resonance). Although it is not as precise as the calibration of the AFM system, due tothe mechanical coupling between piezo and cantilever chip and the high electronic noise in the low frequency range, this calibration nevertheless gives a good estimation of order of magnitude of the measured oscillations. The performed scaling allowed to confirm, that the measured oscillation indeed are excited by thermal noise, and not by some external noise of the system that could have contributed to the oscillation

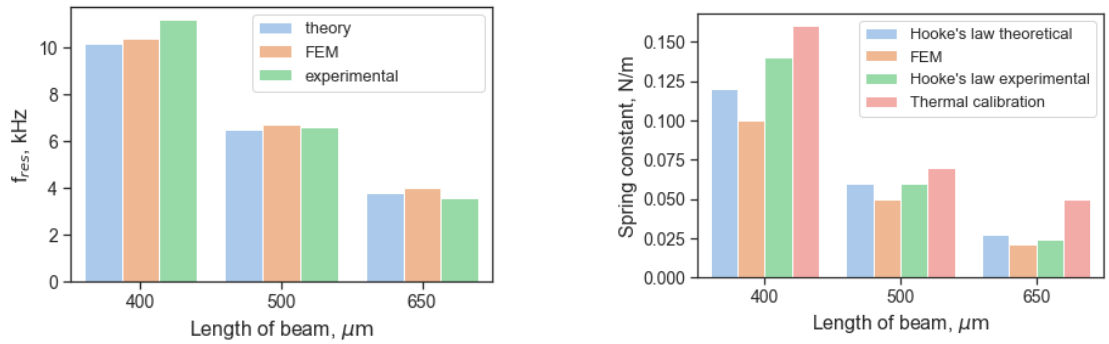

(a) (b)

Figure 4.7: (a) Comparison of the resonance frequency that was calculated theoretically (Eq. 2.1), finite element method simulations (FEM), and experimentally measured. (b) Comparison of the spring constant that was calculated theoretically with Hook's law, using a Euler - Bernoulli theory $f_{res-theor}$ and using the experimental $f_{res-exp}$, as well as FEM and thermal calibration.

of the system in the whole frequency range. This confirmation follows from the estimation of the spring constant (see comparison with other methods at Fig. 4.7b) with $k = \frac{k_B T}{\langle z^2 \rangle}$, where $\langle z^2 \rangle$ was calculated as the area under the peak. The spectrum was scaled using the empirically determined factor to nm^2/Hz, and the power baseline was subtracted from the plot, prior to this calculation (Fig. 4.6).
The Sader's method allows to estimate the spring constant without using properties of the cantilever material and instead, uses the properties of the medium such as density and viscosity. It has a number of other advantages, it can be used in various media, and applied for arbitrary shaped beams. However this method requires the calculation of the imaginary hydrodynamic function, which is a complex computational task. However, an available online calculator, provided by the author [Sader et al., 2016], allows to estimate the spring constant for the desired cantilever dimensions.

4.4 Cultivation of the yeast

4.4.1 Preparation of the medium solutions and agar plates

Yeast Extract-Peptone-Dextrose (YPD) medium was used for cultivating yeast cells in a Petri dish with agar and to grow cells in the liquid medium. A phosphate-buffered saline (PBS) buffer was used to attach the cells to the cantilever surface, as is described further. These mediums were prepared using the following protocols.
The YPD medium solution consist of 950 ml of ultra-pure water (UPW), 20 g of peptone, 20 g of yeast extract 10 g. For the preparation of the agar plates, 24 g of agar was added to this solution. After mixing, the solution was sterilized by autoclaving. 50 mL of sterile 40% weight/volume d-glucose (dextrose) was added to obtain 20 g/L concentration the d-glucose.
Empty Petri dish plates were filled with the mixture of the YPD medium with agar. The YPD

medium solution was filtered with a sterile syringe membrane filter with 0.2 μm pores.
The PBS buffer was prepared using 800 ml of UPW, 8 g of NaCl (0.137 M), 200 mg of KCl (0.0027 M), 1.44 g of Na_2HPO_4 (0.01 M), 245 mg of KH_2PO_4 (0.0018 M). The pH of the PBS solution was adjusted to a value of 7.4, and the mixture was completed with UPW to 1 L of total volume and sterilized in an autoclave.

4.4.2 *S. pombe* cultivation

S. pombe yeast colonies were aliquoted with glycerol, and were frozen at -80 °C. To cultivate the yeast cells on an agar plate, the frozen colonies were placed on a plate of agar with YPD medium, and left in the incubator at 30 °C for 48 hours. Then several colonies were picked up from the plate (Fig. 4.8a), and placed inside a falcon tube with 5 ml of YPD medium (Fig. 4.8b). All operations with the microorganisms and medium were performed in the biosafety cabinet. The *S. pombe* cells were grown then overnight at 30 °C with shaking the falcon tube at 160 rpm.

(a)

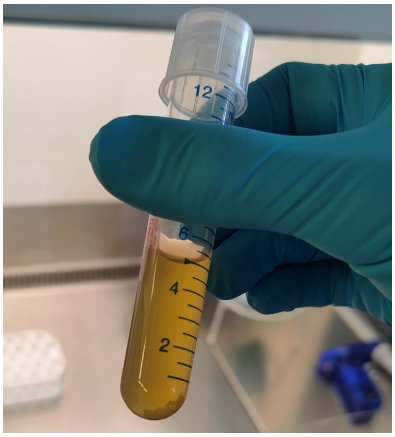

(b)

Figure 4.8: Culturing *S. pombe* yeast: (a) on an agar plate, (b) in the falcon tube with liquid YPD medium.

4.5 Attachment of the living organisms to the cantilever beam

Before any surface treatment, SU-8 chips were cleaned with ethanol. In principle, the attachment of the cell could be performed even without additional treatment, as some of the cells could always adsorb to the surface. However, the SU-8 hydrophobicity can result in a poor attachment of the cells on its surface [Wang et al., 2007; Xue et al., 2014]. The surface functionalization can improve the cells adhesion. For example, the surface functionalization of SU-8 with gluteraldehyde (GA) and various proteins such as fibronectine and collagen is known to make surface of the SU-8 resist hydrophilic [Xue et al., 2014]. Gluteraladehyde is widely used as cells fixative, however it is known that when used at low concentrations, it is harmless for the cells. It also makes SU-8 surface more hydrophilic. Concanavaline A is a

protein, that is commonly used for attaching various yeast cells [Fung et al., 2004; Kohler et al., 2020]. A combination of these two surface treatments was used to improve the adhesion of the *S. pombe* cells, using the following protocol.
Before the attachment of the *S. pombe* yeast cells, the cantilever beams were functionalized with gluteraldehyde (GA) for 10 min, and then with concanavalineA (conA) for 20 min. GA was used at a concentration of 0.5 %, and conA at concentration 2.5 mg/ml. Each of these treatments was followed by a wash of the excess of the solution in the ultra-pure water. *S. pombe* grown in the YPD medium was centrifuged at 5.6 krpm, and transferred to PBS medium. After repeating this procedure, and replacing the medium with fresh PBS at least 3 times, the cantilever beam was incubated with the suspension of *S. pombe* cells for 35 min (Fig. 4.9a). Then the chip was gently washed in YPD medium, transferred to the measurement chamber and filled with YPD. From the optical images of the cantilever (Fig. 4.9b) we estimate that the total number of attached yeast cells is about 200 (assuming that similar amount of the cells is attached at the backside of the cantilever).
To monitor the change in the cells viability, caspofungin drug was used with concentration of 100 μg/ml.

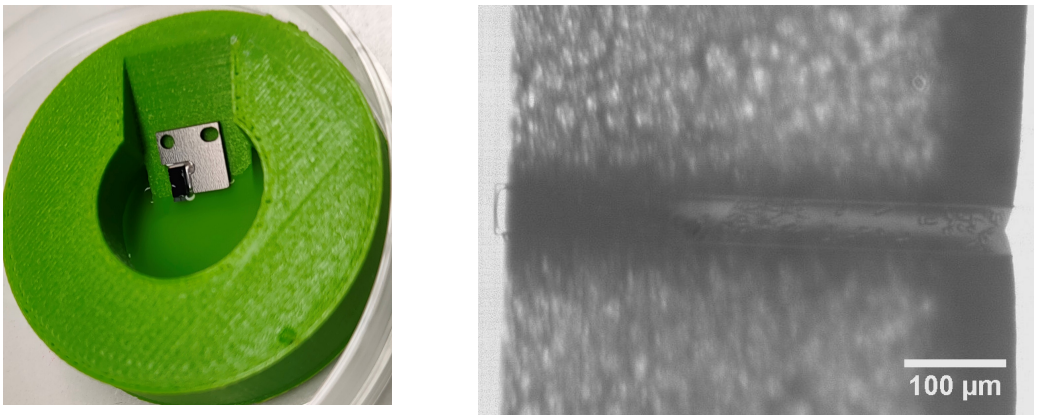

(a) (b)

Figure 4.9: (a) 3D printed incubation cell designed with a slope to attach yeast cells only onto the cantilever. (b) Optical microscopy image of the yeast cells attached to the cantilever.

4.6 Nanomotion of the beams with attached *S. pombe* yeast

4.6.1 Cell viability test

The viability test was performed by the following procedure: the chips were fixed on the metal holder and placed inside the liquid cell that was filled with YPD medium (Fig. 4.10). The successful attachment of cells on the beam surface was confirmed with an optical microscope (Fig. 4.9 (b)). The laser light alignment was assessed with the CCD camera and the photodetector. After the photodetector alignment, the recordings of the oscillations of the beam with attached viable organism is performed. Each recording was made with an acquisition frequency of 30 kHz and had a duration of 20 min, to avoid storage of very large

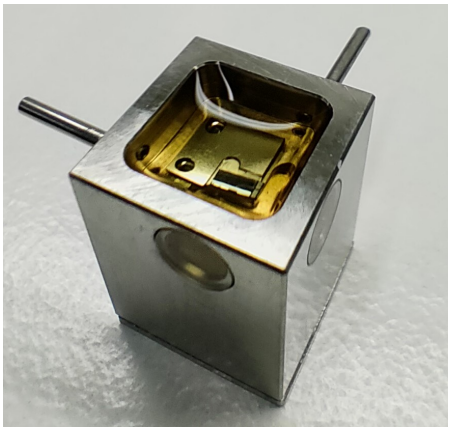

(a)

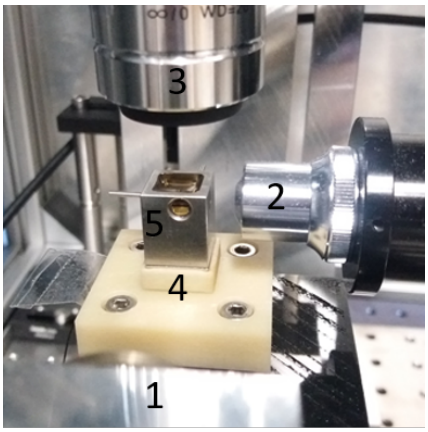

(b)

Figure 4.10: (a) The chip with attached *S. pombe* cells is placed into the metallic chamber that is filled with YPD medium, and (b) placed in the measurement setup: 1 - mounted laser source, 2 - readout optics, 3 - observation optics, 4 - stage with an integrated piezo-actuator and strong magnet for fixing the chamber, 5 - measurement chamber with the cantilever chip.

files and performance issues during data analysis. Typically, the signal was recorded for 40 min, then drug was gently introduced with a micro-pipette into the liquid cell, and the signal was recorded for 40 more min. However, also control experiments have been conducted, and some of them lasted longer (see section 4.6.2 and Fig. 4.16a).

The first step of the data processing consists in as-called flattening of the signal. It is aimed to correct for any slow and long lasting drift of the raw signal, that could be caused by a mechanical drift of the stages, a temperature change, or an electronic drift. This correction is made by splitting the raw data to 200 s long chunks, by performing a linear regression on each of the chunks, and by subtracting it from the raw data (Fig. 4.11). The flattening window size was chosen empirically, to obtain a flat signal after this treatment, but at the same time to avoid to affect the sensor response at frequencies higher than 0.005 Hz. The simplest way to analyse the oscillations consists to look at the evolution of the differential signal (see Fig. 4.12b). However, as it was shown, calculating the cantilever displacement variance with 10 s long windows can give a better representation of the response of the nanomechanical sensor in the viability tests [Longo et al., 2013; Stupar et al., 2017; Kohler et al., 2020]. In these tests, it is expected to observe a reduction of the oscillations after the cells on the cantilever loose their viability. This change in the cantilever oscillation is detected by a decrease of the amplitude of the differential signal (Fig. 4.12b), and by a decrease in the variance (Fig 4.14). Further in this work the scaled variance is used as a main estimate of the changes in the photodetector signal (Fig. 4.14, Fig. 4.16, Fig. 4.17).

Let us consider the variance of the flattened signal.In the typical cell viability tests two effects can be observed: a decrease of the peaks of variance plot, and a decrease of the level of its baseline. Some of the peaks can be attributed to the non biologically relevant phenomena (such as external acoustic noise), since they also can be observed after killing organisms

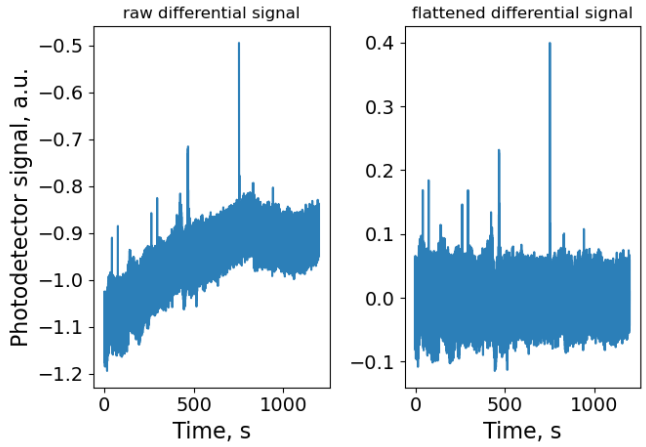

Figure 4.11: Typical evolution of the differential normalized photodetector signal during a single recording: raw signal (left) and after flattening within 200 s - long windows (right). This pre-processing subtracts the long-lasting drifts, and centers the signal.

(Fig. 4.12b), as well as on signals recorded with empty cantilevers (i. e., without cells) (Fig. 4.17). However, other peaks are presumed to be related to the cells activity, since their number is much higher for the signal of the cantilever with viable organisms, than for cantilever without. The reduction of the variance and the appearance of the peaks can be partially explained by nanomechanical motion of the cantilever, but also by the events such as cells passing in front of the light beam [Bennett et al., 2020].

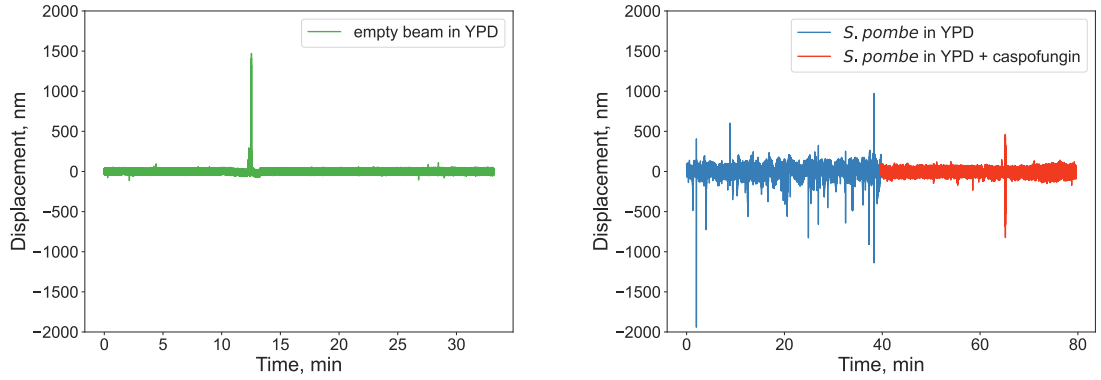

(a) (b)

Figure 4.12: Oscillation signal of the photodetector: (a) typical recording of the signal of a cantilever immersed into the YPD medium without cells, as compared with a typical signal recorded during a viability test and (b) with attached *S. pombe* cells before (blue), and after (red) injection of caspofungine drug at a concentration of 100 μg/ml.

Figure 4.13 depicts at a higher magnification the changes of the oscillation signal before and after the attachment of *S. pombe* onto the cantilever, as well as the drop in the signal amplitude following the injection of the antifungal drug caspofungin, a drug capable to kill *S. pombe*

[Formosa et al., 2013; Perez-Cantero et al., 2019].

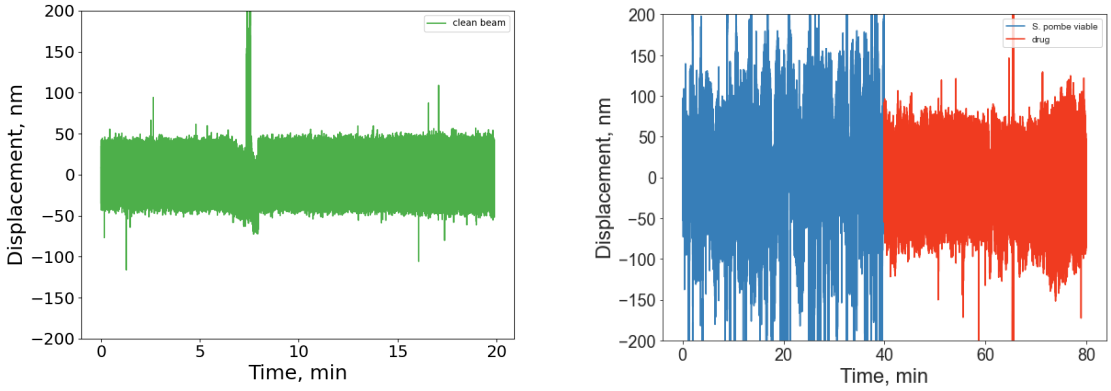

(a) (b)

Figure 4.13: Oscillation signal of the cantilever (scaled to nm) (a) before (green) and (b) after (blue) attachment of *S. pombe* onto the cantilever. Right panel (b): effect of 100 μg/ml concentration antifungal drug (caspofungin) on the oscillation pattern: before (blue) and after (red) the injection. All the recordings were made in YPD.

The calculation of the windowed variance of the signal is a commonly used procedure ([Kasas et al., 2015; Kohler et al., 2020; Longo et al., 2013; Lissandrello et al., 2014; Stupar et al., 2017, 2021]) to asses the results of antimicrobial test. Such a processing of our data sets shows a clear reduction of the oscillations of the cantilever after the injection of the antifungal drug in the measurement system as depicted in Fig. 4.14. The mechanism that defines the change of the variance is complex, and includes not only the nanomechanical motion of the beam, but can also be a result of some optical effects, as was discussed above.Scaling the variance over the median of the recording with viable organisms is used to highlight the relative change of the variance values.[Kohler et al., 2020].

4.6.2 Further tests and control experiments

Figure 4.15a shows a boxplot representation of the viability test to display the response of the mechanical sensors. It shows the difference in the median of the variance signal, as well as the spread of the values. This statistical metrics was chosen as more appropriate estimate, than the mean with standard deviation error bar, since those estimates can be heavily influenced by the spikes present in the original datasets. The boxplot that is represented below (Fig. 4.15a), is calculated using data of 5 independent nanomotion experiments, each of which was scaled to estimate a relative response of the sensor with respect to the oscillations of the cantilever with living cells. Non-parametric Mann–Whitney U test has been performed for these 5 replicates, and resulted in p-value $p \ll 0.01$. The result of the statistical test therefore confirmed the significant difference between median of the signal variance before and after drug exposure. Another way to represent the results of multiple replicate experiments of this type is to plot barplot of the median with a median absolute deviation (MAD) as an error bar (Fig. 4.15b). The latter estimate is a robust statistic estimate, that is similar to standard deviation deviation,

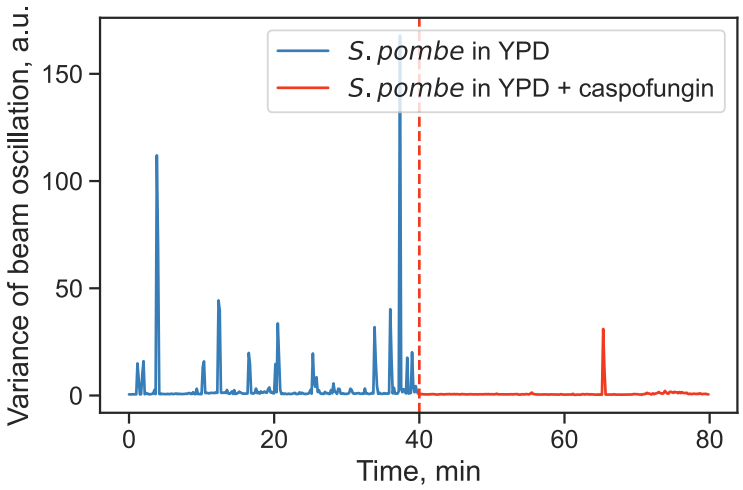

Figure 4.14: Typical viability test. Variance of the recorded signal, calculated within 10 s - long windows. In this experiment *S. pombe* cells were attached onto the cantilever and exposed to caspofungin at a concentration of 100 μg/ml (red). The moment when drug was introduced into the chamber is shown as red dotted line.

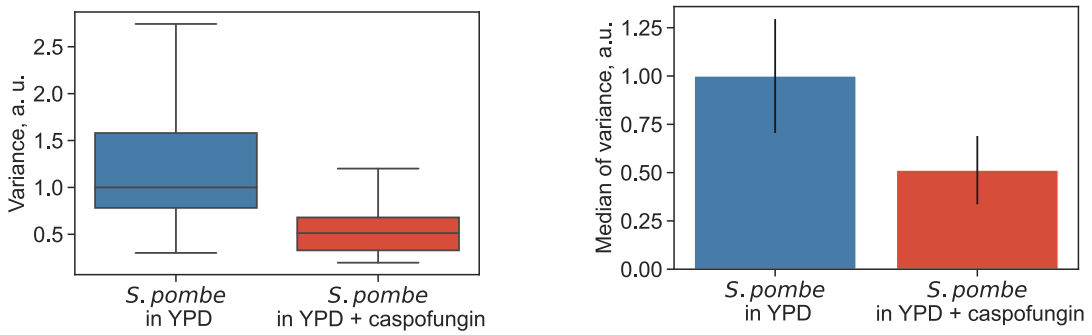

(a) (b)

Figure 4.15: (a) Boxplot representation of the variance of the normalized oscillation signal during the viability test of *S. pombe*, based on 5 independent replicates. Statistical analysis was performed using Mann–Whitney U test, resulting in $p \ll 0.01$. (b) Normalized median of the 10 s windowed variance of oscillation signal measured during the viability test *S. pombe*, based on 5 independent replicates. Median absolute deviation is used as an estimate for error bar.

but is less sensitive to extremely high peaks and data outliers [Gorard, 2005].
In order to confirm the observed response of the sensors, in addition to standard viability tests that were described in the section 4.6.1, several other types of control experiments were conducted. In one type of these tests, the signal was recorded for 80 min, without any action, and then caspofungin drug was introduced into the chamber (Fig. 4.16a). In another type of control experiment, YPD medium (instead of the drug) was added in the chamber during the data acquisition and followed by the injection of the drug solution (Fig. 4.16b). Finally, the third

type of control experiments consisted in following a standard sensitivity test procedure but with no cells attached onto the cantilever. These tests confirmed that the observed response of the beam is neither related to the detachment of the cells from it (Fig. 4.16a) nor related to liquid perturbation, that can be induced by pipetting (Fig. 4.16b), and finally that the drug does not influence the oscillations of the empty cantilevers (Fig. 4.17).

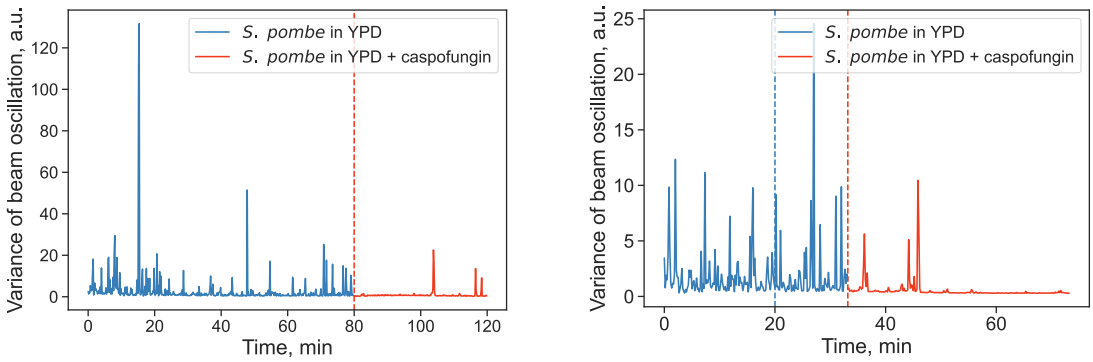

(a) (b)

Figure 4.16: Control experiments: (a) - 80 min long recording of the oscillations of the beam with living yeast cells, and introduction of caspofongine into the analysis chamber (red line) at 80 min, (b) - introducing into the analysis chamber of YPD medium (blue dotted line), followed by the injection of the drug (red dotted line). Time evolution of the variance of the normalized differential photodetector signal, calculated in 10 s windows.

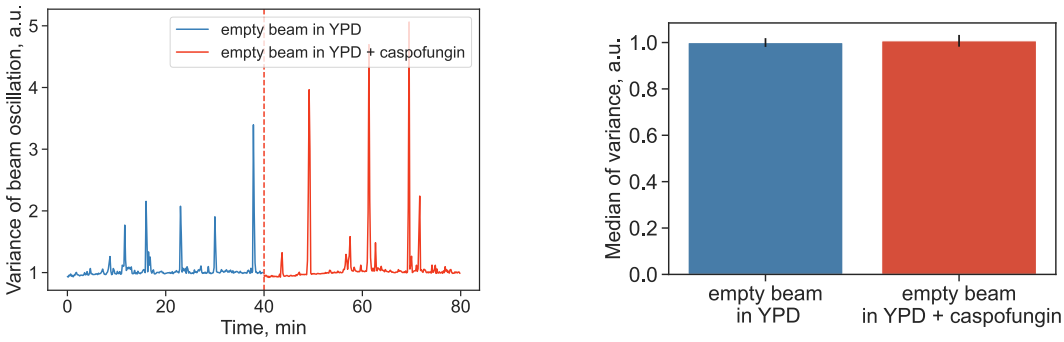

(a) (b)

Figure 4.17: Control experiment: recording oscillations of the empty cantilever (with no cells attached onto its surface) and introduction of the drug (caspofungin) in the chamber after 40 min. (a) Time evolution of the variance of the normalized differential photodetector signal, calculated with 10 s large windows. (b) Median of the normalized variance before (blue) and after (red) introducing the caspofungin drug. Statistical analysis was performed using Mann–Whitney U test. It resulted in $p \gg 0.01$, which indicated no significant difference between variance of the signal before and after drug exposure.

4.6.3 Alternative readout method: power spectral density

In the previous sections of this chapter, the windowed variance analysis was used to process viability tests. However, in other works ([Lissandrello et al., 2014; Mertens et al., 2019]) it was shown, that looking not only at the variance of the signal in the time domain, but also at the power spectra of the signal can also provide valuable information about the life/dead state of the organism. Essentially, both types of analysis should be equivalent according to the Parseval–Plancherel identity. The energy in the time domain should correspond to the energy in the frequency domain, i.e. the area under the power spectra. The same property is used in the thermal calibration of the beam, in which the rms value of the thermal fluctuation is estimated by calculating an area under the peak in the frequency spectra.
I also applied this approach to process viability test data obtained with my prototype. The Power Spectral Density (PSD) was calculated by performing Fast Fourier Transform (FFT) for each of the 10 s long chunks of the differential photodetector signal for the cantilever with living, and antifungal treated cells. The resulting PSD estimate for a single recording was calculated by averaging the PSD of all these chunks. Its 0.1 Hz spectral resolution is defined by the choice of the chunk length. This alternative data processing method also demonstrated a clear difference between living and dead cells as depicted in Figure 4.18. Similarly to other previously published results, my data also highlight a dramatic drop of the power spectra magnitude in the low frequency range in dead cells ([Lissandrello et al., 2014; Mertens et al., 2019]). The rms value of the oscillations in frequency range from 0.1 Hz till 100 Hz, calculated as an area under the curve, or the slope of this low-frequency noise can be as well used as an alternative readout method for making a conclusion about a behaviour of the oscillating beam with attached microorganisms [Mertens et al., 2019].

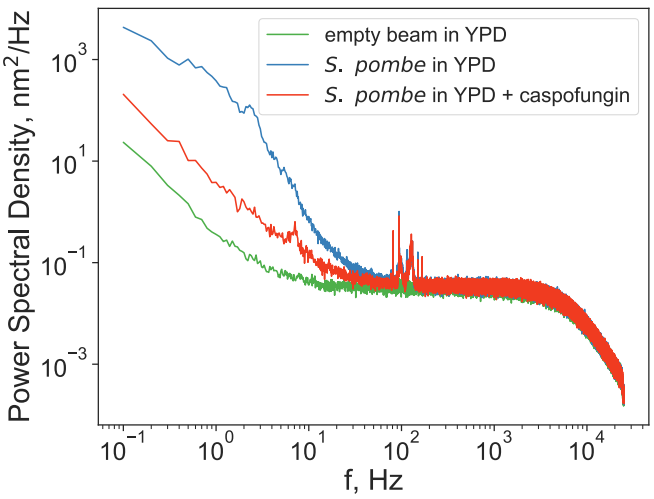

Figure 4.18: Power spectral density of a SU-8 cantilever beam with attached *S. pombe* yeast viable cells (blue), and after introducing caspofungin drug (red) at a concentration of 100 μg/ml.

4.7 Conclusion

Successful light coupling in and out of the cantilever beam was demonstrated. Because of very low light coupling efficiency (total optical losses of order of 30 dB to 50 dB), an amplification board with high gain had to be used, and level of the signal had to be carefully controlled. Optimization of the fabrication process flow, for obtaining the better cladding that would minimize light loss, can help to solve these problems.
The ability of the system to sense the displacement of the light output, was demonstrated by periodic actuation of the measurement chamber with a piezoelectric actuator, as well as by moving the readout system.
Both timeseries signal and Power Spectral Density characteristics were used for the periodic oscillation tests and for biological experiments. The ability to sense cantilever oscillations with amplitudes of order of few tens of nm, at frequencies below 300 Hz, was demonstrated. The measurement displacement resolution is about $\sqrt{0.03\ \mathrm{nm}^2/\mathrm{Hz}} \approx 0.17\ \mathrm{nm}/\sqrt{\mathrm{Hz}} \approx 0.2\ \mathrm{nm}/\sqrt{\mathrm{Hz}}$ above the 1/f corner frequency of 5 Hz.Sensing of the changing in the viability of the *S. pombe* cell, attached to the beam, was demonstrated by monitoring oscillations of the beam in the YPD medium, and upon the action of the caspofungin. This effect was confirmed by tests on 5 independent replicates. Negative control experiments were also performed, showing no significant reaction upon introducing more YPD medium in the chamber, or performing no action at all, and as well no significant response to the drug of the clean beam (without cells).
Median of variance of photodetector signal was used as a main estimate of the signal response for the performed viability test. Results, based on 5 independent replicates are presented a boxplot, and as a median with absolute median deviation error estimate. Power Spectral Density estimate showed that observed nanomotion sensor response is mainly the frequency range below 100 Hz.

Optomechnical SU-8 cantilever - based sensors have demonstrated results that are compatible with those obtained with “traditional” AFM based devices [Longo et al., 2013; Kohler et al., 2020; Lissandrello et al., 2014]. The proof-of-principle was demonstrated using *S. pombe* yeast cells as test microorganism, that is nonpathogenic. However, similarly to the AFM-based nanomotion detectors, application of the developed optomechanical sensors can be easily extrapolated to the pathogenic yeast microorganisms, such as *Candida albicans* [Kohler et al., 2020], and to smaller microorganisms, such as *E. coli* bacteria [Stupar et al., 2017]. The experimental protocols require only slight modification. Nevertheless, additional tests are needed to confirm whether developed optomechanical device is sensitive enough to detect oscillations of bacteria.
The proposed readout scheme permits a simple readout set up and opens the possibility to create miniaturized and integrated sensing systems [Li et al., 2009; Xu et al., 2004], with all elements embedded on a single chip. Importantly, in the future, such sensing platforms can be designed with several cantilevers on the same chip, and the displacement of each of them could be recorded simultaneously with a CCD camera or a photodetector array. Imple-

mentation of the multi-sensor devices would allow to have more statistics of the cantilevers response to the same drug, test effect of the cantilever spring constant on the magnitude of the response (if cantilevers on the same chip would be fabricated with different stiffness), or have antimicrobial testing to several different drug on the same time. For the latter application, an integrated microfluidic system would be required.
However, similarly to the AFM-based nanomotion detectors, a reliable and consistent attachment of the cells on the cantilever surface is needed. Unlike optical nanomotion techniques that detect displacement and oscillation of the cells by imaging the single cells and performing image analysis [Syal et al., 2017; Willaert et al., 2020], cantilever-based nanomotion detectors response can not be directly attributed to the oscillation of single cells. Instead, it is a cumulative effect of the change in the activity of multiple cells attached to the cantilever . This effect is complex, and could have various causes, such as optical effect (when some cells are crossing the laser path), vertical motion of the attached cells, local change of pH and of temperature [Chomicki, 2019].
In order to implement sensor in the device that could be used in the clinic, the measurement setup should be further optimized and miniaturized, the light coupling procedures have to be automatized with some motorized micromechanical stages. This would allow simplified use of the device by the medical personnel.

5 Conclusion and outlook

Bacterial and fungal resistance to existing antibiotics and antifungals is one of the major public health problems nowadays. To prevent the spread of resistant strains, rapid ASTs seems a very promising solution. In the introduction of this thesis it was demonstrated, that there are various techniques that propose fast antimicrobial tests that are based on - molecular, optical or nanomechanical principles. The last one was successfully applied to a very broad range of species such as bacteria, yeast, vegetal and human cells. In this thesis, this technique was modified by integrating in the mechanical sensor a light guide and by detecting the lever displacements by monitoring the output of the light spot. More precisely, the sensing chip consist of a light guiding structure and a suspended beam at its end. The output light is focused on the sensing area of a photodetector, without the need to couple it to another waveguide. It avoids technical difficulties, related to the mismatch between two waveguides, and the accumulation of the microorganisms in the small gap between the two waveguides. The detection is made in the so-called dynamic mode that allows to attribute the readout signal to changes in the viability of the attached cells.

The functional part of the sensing devices is an SU-8 polymer beam, that was designed with the following dimensions: 5 μm - thick, 50 μm - wide, and a length varying from 400 μm to 650 μm. It resulted in cantilevers with spring constants ranging from 0.1 to 0.02 N/m. The spring constant was estimated using the Euler–Bernoulli beam model, the Hooke's law, and finite element method (FEM). It was also measured experimentally by using a thermal fluctuations based calibration. The measurements were in good agreement with the mathematical models.

The main noise sources of the system were found to be thermal, flicker or 1/f, and shot noises. The contribution of each of the noise types was quantified. It has been found that in the low frequency region of the power spectra the 1/f noise dominates over other types. This frequency domain corresponds to the where the nanomechanical motion of the cantilever is affected by the attached yeast cells studied in this work.

Several strategies to micro-fabricate SU-8 light guiding structures with a free-standing beam were explored. They consisted in setting up an SU-8 double-layer (in which the bottom one works as a sacrificial layer for the beam release), in wet etching, and in isotropic dry etching techniques.

The dry etch process flow gave good results: the fabricated SU-8 devices were successfully used as optomechanical sensors, and had the mechanical parameters that were very close to the designed values. However, two main disadvantages in the microfabrication flow have been observed. The total optical losses were high, order of 30 dB to 50 dB (improved optical cladding layer probably could reduce propagation losses, and optimization of the experimental set-up - reduce coupling losses). The second problem is related to the bending of the SU-8 cantilevers. It is probably caused by the dry plasma etching and hotplate baking steps. This could be further optimized by, for example, protecting the SU-8 from plasma ions with an additional oxide layer, that could be removed afterwards. However, both of these issues were not critical. In spite of these problems, the light was successfully coupled in- and -out of the SU-8 structures, and these chips were used for optomechanical sensing.

The experimental setup for performing optomechanical measurements was assembled onto a vibration isolating table. It consists of micromechanical stages, a laser source with an integrated optics, a stage with an integrated piezo-actuator, and optical microscopes to observe the surface of the chip, to control the laser alignment, and to record the output signal. A dedicated measurement cell was built, to hold the microfabricated chip, to couple the light through glass windows and to perform measurements, both in air and in liquids. This setup also permitted to drive the whole chamber into oscillations, with a chosen amplitude and frequency.

The final setup was sensitive enough to detect cantilever oscillations in the nanometer-scaled displacement range (the equivalent displacement resolution is about 0.2 nm/$\sqrt{\text{Hz}}$).
Finally, the capacity of the device to monitor life – dead transitions was assessed with the yeast *S. pombe*. The effect of caspofongin on *S. pombe*, attached to the beam, was demonstrated by monitoring the oscillations of the beam in the YPD medium, before and after addition of the drug in the analysis chamber. This effect was confirmed by tests on several independent replicates.
The cantilever oscillations variance signal as well its power spectral density (PSD) were used to estimate the attached organism viability. The measurements demonstrated that the nanomotion sensor response is mainly in the frequency range below 100 Hz.

This work is a contribution into the development of rapid antimicrobial testing tools to fight the microorganism resistance problem. Additional research efforts should be done to unveil the nature the physiological phenomena that result in cellular nanomotion.
Further efforts should also be focused on the improvement of the microfabrication process, as well of the measurement setup, to obtain more sensitive and stable sensing devices which could be used to measure biological entities producing smaller forces on the cantilever. The concept of the device seems promising since it permits further miniaturization, and integration of all the elements, i.e. the light source, the detector, the sensing device, and the microfluidic channels on the same chip. Finally, multiplexing several sensors should permit test multiple species or drugs simultaneously. The readout of multiplexed signals could be performed by means of fast CCD cameras or by array photodetector.

A An appendix

This section contains 3D image of the measurement chamber, and whole schematics of the amplification board that was used for amplifying photodetector currents.

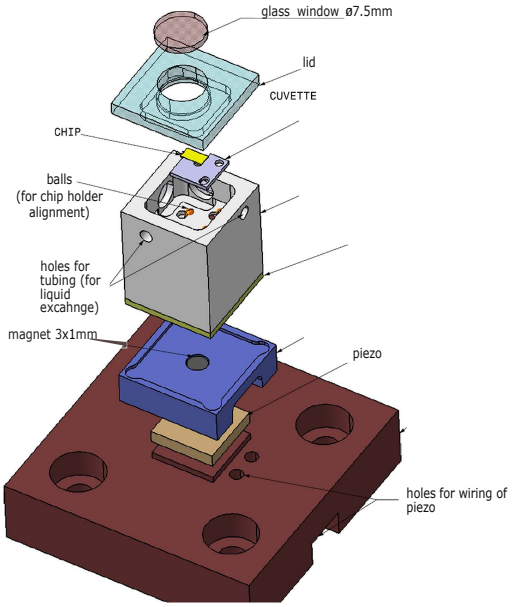

Figure A.1: Design of the measurement chamber (gray) with a cantilever holder (light violet), piezo-actuator (orange), and rigid metal stage (red).

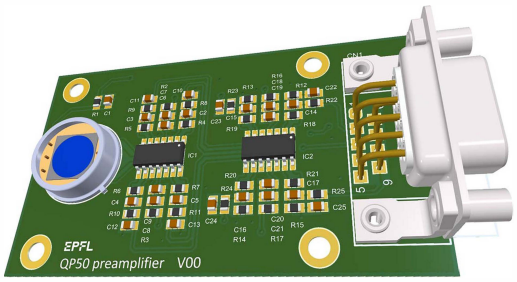

Figure A.2: Implementation of the amplification board with all elements on the board.

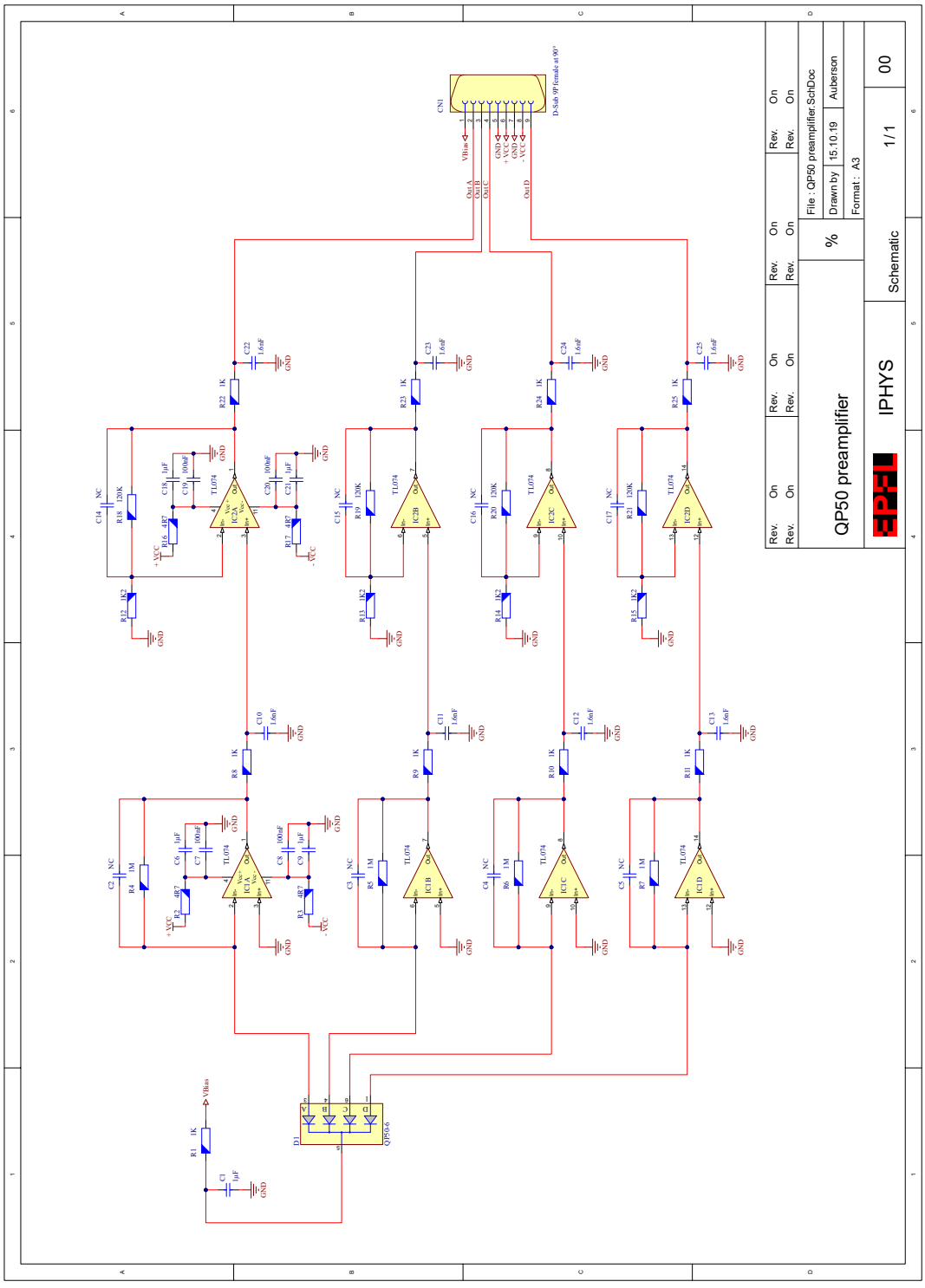

Figure A.3: Schematics of the amplification board with gains of the stages $G_1 = 10^6$ V/A, and $G_2 = 10^2$ V/V, resulting in a total gain of $G = G_1 \cdot G_2 = 10^8$ V/A.

Bibliography

Łabędź, B., Wańczyk, A., and Rajfur, Z. (2017). Precise mass determination of single cell with cantilever-based microbiosensor system. *PLOS ONE*, 12(11):1–14. Publisher: Public Library of Science.

Abgrall, P., Conedera, V., Camon, H., Gue, A.-M., and Nguyen, N.-T. (2007). SU-8 as a structural material for labs-on-chips and microelectromechanical systems. *Electrophoresis*, 28(24):4539–4551.

Alvarez, M. and Lechuga, L. M. (2010). Microcantilever-based platforms as biosensing tools. *Analyst*, 135(5):827–836.

Anhoj, T. A., Jorgensen, A. M., Zauner, D. A., and Hübner, J. (2006). The effect of soft bake temperature on the polymerization of SU-8 photoresist. *Journal of Micromechanics and Microengineering*, 16(9):1819–1824.

Bassetti, M., Merelli, M., Temperoni, C., and Astilean, A. (2013). New antibiotics for bad bugs: where are we? *Annals of Clinical Microbiology and Antimicrobials*, 12(1):22.

Bennett, I., Pyne, A. L. B., and McKendry, R. A. (2020). Cantilever sensors for rapid optical antimicrobial sensitivity testing. *ACS Sensors*, 5(10):3133–3139. PMID: 32900182.

Binnig, G., Quate, C. F., and Gerber, C. (1986). Atomic force microscope. *Phys. Rev. Lett.*, 56:930–933.

Calleja, M., Tamayo, J., Nordström, M., and Boisen, A. (2006a). Low-noise polymeric nanomechanical biosensors. *Applied Physics Letters*, 88(11):113901. _eprint: https://doi.org/10.1063/1.2187437.

Calleja, M., Tamayo, J., Nordstrom, M., and Boisen, A. (2006b). Low-noise polymeric nanomechanical biosensors. *Applied Physics Letters*, 88(11).

Cantón, R., Pérez-Vázquez, M., Oliver, A., Saz, B. S. D., Gutiérrez, M. O., Martínez-Ferrer, M., and Baquero, F. (2000). Evaluation of the wider system, a new computer-assisted image-processing device for bacterial identification and susceptibility testing. *Journal of Clinical Microbiology*, 38(4):1339–1346.

Cassini, A., Hogberg, L. D., Plachouras, ..., S., and Grp, B. A. C. (2019). Attributable deaths and disability-adjusted life-years caused by infections with antibiotic-resistant bacteria in the

EU and the European Economic Area in 2015: a population-level modelling analysis. *Lancet Infectious Diseases*, 19(1):56–66.

Ceyssens, F. and Puers, R. (2006). Creating multi-layered structures with freestanding parts in SU-8. *Journal of Micromechanics and Microengineering*, 16(6):S19–S23.

Chen, Q., Fang, J., Ji, H.-F., and Varahramyan, K. (2007). Fabrication of SiO_2 Microcantilever Using Isotropic Etching With ICP. *IEEE Sensors Journal*, 7(12):1632–1638. Conference Name: IEEE Sensors Journal.

Chen, Z. and Lee, J.-B. (2021). Biocompatibility of su-8 and its biomedical device applications. *Micromachines*, 12(7).

Chomicki, W. (2019). Development of an afm-based nanomotion detection device for microbiological samples. page 188.

Chon, J. W. M., Mulvaney, P., and Sader, J. E. (2000). Experimental validation of theoretical models for the frequency response of atomic force microscope cantilever beams immersed in fluids. *Journal of Applied Physics*, 87(8):3978–3988.

Chung, S. and Park, S. (2013a). Effects of temperature on mechanical properties of su-8 photoresist material. *Journal of Mechanical Science and Technology*, 27(9):2701–2707.

Chung, S. and Park, S. (2013b). Effects of temperature on mechanical properties of su-8 photoresist material. *Journal of Mechanical Science and Technology*, 27(9):2701–2707.

Cleveland, J. P., Manne, S., Bocek, D., and Hansma, P. K. (1993). A nondestructive method for determining the spring constant of cantilevers for scanning force microscopy. *Review of Scientific Instruments*, 64(2):403–405.

Cumpson, P., Clifford, C., Portoles, J., Johnstone, J., and Munz, M. (2008). Cantilever spring-constant calibration in atomic force microscopy. *NanoScience and Technology*.

Department of Health and Human Services CDC (2019). Antibiotic resistance threats in the united states.

Didelot, X., Bowden, R., Wilson, D. J., Peto, T. E. A., and Crook, D. W. (2012). Transforming clinical microbiology with bacterial genome sequencing. *Nature Reviews Genetics*, 13(9):601–612.

Dinarelli, S., Girasole, M., Kasas, S., and Longo, G. (2017). Nanotools and molecular techniques to rapidly identify and fight bacterial infections. *Journal of Microbiological Methods*, 138(SI):72–81.

Estevez, M.-C., Alvarez, M., and Lechuga, L. M. (2012). Integrated optical devices for lab-on-a-chip biosensing applications. *Laser & Photonics Reviews*, 6(4):463–487.

Etayash, H., Khan, M. F., Kaur, K., and Thundat, T. (2016). Microfluidic cantilever detects bacteria and measures their susceptibility to antibiotics in small confined volumes. *Nature Communications*, 7(1):12947.

European Centre for Disease Prevention and Control (2020). Antimicrobial resistance in the eu/eea (ears-net) -annual epidemiological report 2019. Technical report.

Ezkerra, A., Fernández, L. J., Mayora, K., and Ruano-López, J. M. (2007). Fabrication of SU-8 free-standing structures embedded in microchannels for microfluidic control. *Journal of Micromechanics and Microengineering*, 17(11):2264–2271. Publisher: IOP Publishing.

Farina, D., Alvarez, M., Marquez, S., Dominguez, C., and Lechuga, L. M. (2016). Out-of-plane single-mode photonic microcantilevers for integrated nanomechanical sensing platform. *Sensors and Actuators B-Chemical*, 232:60–67.

Formosa, C., Schiavone, M., Martin-Yken, H., Francois, J. M., Duval, R. E., and Dague, E. (2013). Nanoscale Effects of Caspofungin against Two Yeast Species, Saccharomyces cerevisiae and Candida albicans. *Antimicrobial Agents and Chemotherapy*, 57(8):3498–3506.

Frye, J. G., Jesse, T., Long, F., Rondeau, G., Porwollik, S., McClelland, M., Jackson, C. R., Englen, M., and Fedorka-Cray, P. J. (2006). Dna microarray detection of antimicrobial resistance genes in diverse bacteria. *International Journal of Antimicrobial Agents*, 27(2):138–151.

Fung, T. H., Ball, G. I., McQuaide, S. C., Chao, S.-H., Coleman-Lerner, A., Holl, M. R., and Meldrum, D. R. (2004). Microprinting of On-Chip Cultures: Patterning of Yeast Cell Microarrays Using Concanavalin-A Adhesion. Advances in Bioengineering:373–374.

Gibson, C. T., Weeks, B. L., Lee, J. R. I., Abell, C., and Rayment, T. (2001). A nondestructive technique for determining the spring constant of atomic force microscope cantilevers. *Review of Scientific Instruments*, 72(5):2340–2343.

Giessibl, F. J. and Trafas, B. M. (1994). Piezoresistive cantilevers utilized for scanning tunneling and scanning force microscope in ultrahigh vacuum. *Review of Scientific Instruments*, 65(6):1923–1929.

Gorard, S. (2005). Revisiting a 90-year-old debate: The advantages of the mean deviation. *British Journal of Educational Studies*, 53(4):417–430.

Guan, Y., Shan, X., Wang, S., Zhang, P., and Tao, N. (2014). Detection of molecular binding via charge-induced mechanical response of optical fibers. *Chemical Science*, 5(11):4375–4381.

Hopcroft, M., Kramer, T., Kim, G., Takashima, K., Higo, Y., Moore, D., and Brugger, J. (2005). Micromechanical testing of SU-8 cantilevers. *Fatigue & Fracture of Engineering Materials & Structures*, 28(8):735–742.

Hu, W., Anderson, R., Qian, Y., Song, J., Noh, J. W., Kim, S., and Nordin, G. P. (2009). Demonstration of microcantilever array with simultaneous readout using an in-plane photonic transduction method. *Review Of Scientific Instruments*, 80(8).

Hutter, J. L. and Bechhoefer, J. (1993). Calibration of atomic-force microscope tips. *Review of Scientific Instruments*, 64(7):1868–1873.

Ilic, B., Czaplewski, D., Zalalutdinov, M., Craighead, H. G., Neuzil, P., Campagnolo, C., and Batt, C. (2001a). Single cell detection with micromechanical oscillators. *Journal of Vacuum Science & Technology B: Microelectronics and Nanometer Structures Processing, Measurement, and Phenomena*, 19(6):2825–2828.

Ilic, B., Czaplewski, D., Zalalutdinov, M., Craighead, H. G., Neuzil, P., Campagnolo, C., and Batt, C. (2001b). Single cell detection with micromechanical oscillators. *Journal of Vacuum Science & Technology B: Microelectronics and Nanometer Structures Processing, Measurement, and Phenomena*, 19(6):2825–2828.

Imamura, G., Shiba, K., Yoshikawa, and Finite, G. (2016). Element analysis on nanomechanical sensing of cellular forces. *Analytical Sciences*, 32(11):1189–1194.

Instruments, T. (2021). *TL07xx Low-Noise FET-Input Operational Amplifiers*.

Jung, W. (2004). *Op Amp Applications Handbook*. Analog Devices series. Elsevier Science & Technology, Oxford.

Kasas, S., Ruggeri, F. S., Benadiba, C., Maillard, C., Stupar, P., Tournu, H., Dietler, G., and Longo, G. (2015). Detecting nanoscale vibrations as signature of life. *Proceedings of the National Academy of Sciences*, 112(2):378–381.

Kee, J. S., Lim, S. Y., Perera, A. P., Zhang, Y., and Park, M. K. (2013). Plasmonic nanohole arrays for monitoring growth of bacteria and antibiotic susceptibility test. *Sensors and Actuators B: Chemical*, 182:576–583.

Keller, S., Blagoi, G., Lillemose, M., Haefliger, D., and Boisen, A. (2008). Processing of thin SU-8 films. *Journal of Micromechanics and Microengineering*, 18(12):125020.

Keller, S., Haefliger, D., and Boisen, A. (2010). Fabrication of thin SU-8 cantilevers: initial bending, release and time stability. *Journal of Micromechanics and Microengineering*, 20(4):045024. Publisher: IOP Publishing.

Koev, S., Fernandes, R., Bentley, W., and Ghodssi, R. (2009). A Cantilever Sensor With an Integrated Optical Readout for Detection of Enzymatically Produced Homocysteine. *IEEE Transactions on Biomedical Circuits and Systems*, 3:415–423.

Kohler, A.-C., Venturelli, L., Kannan, A., Sanglard, D., Dietler, G., Willaert, R., and Kasas, S. (2020). Yeast Nanometric Scale Oscillations Highlights Fibronectin Induced Changes in C. albicans. *Fermentation*, 6(1).

Korayem, M., Ebrahimi, N., and Sotoudegan, M. (2011). Frequency response of atomic force microscopy microcantilevers oscillating in a viscous liquid: A comparison of various methods. *Scientia Iranica*, 18(5):1116 – 1125.

Labuda, A., Bates, J., and Grutter, P. (2012). The noise of coated cantilevers. *Nanotechnology*, 23:025503.

Lübbe, J., Temmen, M., Schnieder, H., and Reichling, M. (2011). Measurement and modelling of non-contact atomic force microscope cantilever properties from ultra-high vacuum to normal pressure conditions. *Measurement Science and Technology*, 22(5):055501.

Lee, C., Itoh, T., Chu, J., Ohashi, T., Maeda, R., Schroth, A., and Suga, T. (1996). Smart piezoelectric pzt microcantilevers with inherent sensing and actuating abilities for afm and lfm. *MRS Online Proceedings Library*, 459(1):35–40.

Leonard, H., Halachmi, S., Ben-Dov, N., Nativ, O., and Segal, E. (2017). Unraveling Antimicrobial Susceptibility of Bacterial Networks on Micropillar Architectures Using Intrinsic Phase-Shift Spectroscopy. *ACS NANO*, 11(6):6167–6177.

Li, M., Pernice, W. H. P., and Tang, H. X. (2009). Broadband all-photonic transduction of nanocantilevers. *Nature Nanotechnology*, 4(6):377–382.

Li, Y. (2018). Challenges and Issues of Using Polymers as Structural Materials in MEMS: A Review. *Journal of Microelectromechanical Systems*, 27(4):581–598.

Lim, Y. C., Kouzani, A. Z., Kaynak, A., Dai, X. J., Littlefair, G., and Duan, W. (2015). A protocol for improving fabrication yield of thin SU-8 microcantilevers for use in an aptasensor. *Microsystem Technologies*, 21(2):371–380.

Lissandrello, C., Inci, F., Francom, M., Paul, M. R., Demirci, U., and Ekinci, K. L. (2014). Nanomechanical motion of Escherichia coli adhered to a surface. *Applied Physics Letters*, 105(11):113701. _eprint: https://aip.scitation.org/doi/pdf/10.1063/1.4895132.

Livermore, D. (2004). The need for new antibiotics. *Clinical Microbiology and Infection*, 10(4):1–9. Symposim on Antimicrobial Therapy in the21st Century, Stockholm, SWEDEN, JUN 21, 2003.

Longo, G., Alonso-Sarduy, L., Rio, L. M., Bizzini, A., Trampuz, A., Notz, J., Dietler, G., and Kasas, S. (2013). Rapid detection of bacterial resistance to antibiotics using AFM cantilevers as nanomechanical sensors. *Nature Nanotechnology*, 8(7):522–526.

Malitson, I. H. (1965). Interspecimen comparison of the refractive index of fused silica∗,†. *J. Opt. Soc. Am.*, 55(10):1205–1209.

Mariana, S., Hamdana, G., Dickmann, J., Bertke, M., Michel, C., Meyer, J., Yulianto, N., Cagnoli, G., Peiner, E., Waag, A., Granata, M., Kroker, S., and Wasisto, H. S. (2019). Fabrication of SiO2 microcantilever arrays for mechanical loss measurements. *Materials Research Express*, 6(4):045206. Publisher: IOP Publishing.

Marinins, A., Knudde, N., and Popov, S. (2016). Air-suspended su-8 strip waveguides with high refractive index contrast. *IEEE Photonics Technology Letters*, 28(17):1862–1865.

Martham, S. K., Nan, K. K., and Shahimin, M. M. (2014). Refractive index modification of su-8 polymer based waveguide via fabrication parameters. In *2014 IEEE Student Conference on Research and Development*, pages 1–5.

Martinez, V., Behr, P., Drechsler, U., Polesel-Maris, J., Potthoff, E., Voeroes, J., and Zambelli, T. (2016a). SU-8 hollow cantilevers for AFM cell adhesion studies. *Journal of Micromechanics and Microengineering*, 26(5).

Martinez, V., Behr, P., Drechsler, U., Polesel-Maris, J., Potthoff, E., Vörös, J., and Zambelli, T. (2016b). SU-8 hollow cantilevers for AFM cell adhesion studies. *Journal of Micromechanics and Microengineering*, 26(5):055006. Publisher: IOP Publishing.

Mertens, J., Cuervo, A., and Carrascosa, J. L. (2019). Nanomechanical detection of escherichia coli infection by bacteriophage t7 using cantilever sensors. *Nanoscale*, 11:17689–17698.

Mironov, V. L. (2004).

Misiakos, K., Raptis, I., Gerardino, A., Contopanagos, H., and Kitsara, M. (2009). A monolithic photonic microcantilever device for in situ monitoring of volatile compounds. *Lab On a Chip*, 9(9):1261–1266.

Moser, Y., Forti, R., Jiguet, S., Lehnert, T., and Gijs, M. A. M. (2011). Suspended su-8 structures for monolithic microfluidic channels. *Microfluidics and Nanofluidics*, 10(1):219–224.

Ness, S. J., Anderson, R. R., Hu, W., Richards, D. C., Oxborrow, J., Gustafson, T., Tsai, B., Kim, S., Mazzeo, B., Woolley, A., and Nordin, G. P. (2013). Weak adsorption-induced surface stress for streptavidin binding to biotin tethered to silicon microcantilever arrays. *IEEE Sensors Journal*, 13(3):959–968.

Nishida, S., Kobayashi, D., Sakurada, T., Nakazawa, T., Hoshi, Y., and Kawakatsu, H. (2008). Photothermal excitation and laser doppler velocimetry of higher cantilever vibration modes for dynamic atomic force microscopy in liquid. *Review of Scientific Instruments*, 79(12):123703.

Noeth, N., Keller, S. S., and Boisen, A. (2010). Fabrication of a cantilever-based microfluidic flow meter with nL min-1resolution. *Journal of Micromechanics and Microengineering*, 21(1):015007. Publisher: IOP Publishing.

Nordström, M., Zauner, D. A., Calleja, M., Hübner, J., and Boisen, A. (2007). Integrated optical readout for miniaturization of cantilever-based sensor system. *Applied Physics Letters*, 91(10):103512.

Nordstrom, M. (2004). Fabrication of cantilever chip with complementary micro channel system in su-8 for biochemical detection. *M.Sc. Thesis*.

Nordstrom, M., Keller, S., Lillemose, M., Johansson, A., Dohn, S., Haefliger, D., Blagoi, G., Havsteen-Jakobsen, M., and Boisen, A. (2008). SU-8 cantilevers for bio/chemical sensing; Fabrication, characterisation and development of novel read-out methods. *Sensors*, 8(3):1595–1612.

Nordstrom, M., Zauner, D. A., Boisen, A., and Hubner, J. (2007). Single-mode waveguides with su-8 polymer core and cladding for moems applications. *Journal of Lightwave Technology*, 25(5):1284–1289.

Park, K., Jang, J., Irimia, D., Sturgis, J., Lee, J., Robinson, J. P., Toner, M., and Bashir, R. (2008). 'Living cantilever arrays' for characterization of mass of single live cells in fluids. *Lab On a Chip*, 8(7):1034–1041.

Perez-Cantero, A., Thomson, P., Paredes, K., Guarro, J., and Capilla, J. (2019). Antifungal susceptibility of Saccharomyces cerevisiae and therapy in a murine model of disseminated infection. *Revista Iberoamericana de Micologia*, 36(1):37–40.

Prokop, C., Irmler, N., Laegel, B., Wolff, S., Mitchell, A., and Karnutsch, C. (2017). Optofluidic refractive index sensor based on air-suspended su-8 grating couplers. *Sensors and Actuators A: Physical*, 263:439–444.

Prokop, C., Schoenhardt, S., Laegel, B., Wolff, S., Mitchell, A., and Karnutsch, C. (2016). Air-suspended su-8 polymer waveguide grating couplers. *J. Lightwave Technol.*, 34(17):3966–3971.

Pujol-Vila, F., Villa, R., and Alvarez, M. (2020). Nanomechanical Sensors as a Tool for Bacteria Detection and Antibiotic Susceptibility Testing. *Frontiers in Mechanical Engineering*, 6:44.

Ramos, D., Calleja, M., Mertens, J., Zaballos, A., and Tamayo, J. (2007). Measurement of the mass and rigidity of adsorbates on a microcantilever sensor. *Sensors*, 7(9):1834–1845.

Ransley, J. H. T., Watari, M., Sukumaran, D., McKendry, R. A., and Seshia, A. A. (2006). SU8 bio-chemical sensor microarrays. *Microelectronic Engineering*, 83(4):1621–1625.

Robin, C. J., Vishnoi, A., and Jonnalagadda, K. N. (2014). Mechanical Behavior and Anisotropy of Spin-Coated SU-8 Thin Films for MEMS. *Journal of Microelectromechanical Systems*, 23(1):168–180.

Rugar, D., Mamin, H. J., and Guethner, P. (1989). Improved fiber-optic interferometer for atomic force microscopy. *Applied Physics Letters*, 55(25):2588–2590.

Sader, J. E. (1998). Frequency response of cantilever beams immersed in viscous fluids with applications to the atomic force microscope. *Journal of Applied Physics*, 84(1):64–76.

Sader, J. E., Borgani, R., Gibson, C. T., Haviland, D. B., Higgins, M. J., Kilpatrick, J. I., Lu, J., Mulvaney, P., Shearer, C. J., Slattery, A. D., Thorén, P.-A., Tran, J., Zhang, H., Zhang, H., and Zheng, T. (2016). A virtual instrument to standardise the calibration of atomic force microscope cantilevers. *Review of Scientific Instruments*, 87(9):093711.

Stupar, P., Opota, O., Longo, G., Prod'hom, G., Dietler, G., Greub, G., and Kasas, S. (2017). Nanomechanical sensor applied to blood culture pellets: a fast approach to determine the antibiotic susceptibility against agents of bloodstream infections. *Clinical Microbiology and Infection*, 23(6):400–405.

Stupar, P., Podolski-Renić, A., Villalba, M. I., Dragoj, M., Jovanović Stojanov, S., Pešić, M., and Kasas, S. (2021). Nano-motion analysis for rapid and label free assessing of cancer cell sensitivity to chemotherapeutics. *Medicina*, 57(5).

Syal, K., Iriya, R., Yang, Y., Yu, H., Wang, S., Haydel, S. E., Chen, H.-Y., and Tao, N. (2016). Antimicrobial susceptibility test with plasmonic imaging and tracking of single bacterial motions on nanometer scale. *ACS Nano*, 10(1):845–852.

Syal, K., Shen, S., Yang, Y., Wang, S., Haydel, S. E., and Tao, N. (2017). Rapid antibiotic susceptibility testing of uropathogenic e. coli by tracking submicron scale motion of single bacterial cells. *ACS Sensors*, 2(8):1231–1239.

The IACG on Antimicrobial Resistance (2019). No time to wait: Securing the future from drug-resistant infections.

Tortonese, M., Barrett, R. C., and Quate, C. F. (1993). Atomic resolution with an atomic force microscope using piezoresistive detection. *Applied Physics Letters*, 62(8):834–836.

Wang, Y., Pai, J.-H., Lai, H.-H., Sims, C. E., Bachman, M., Li, G. P., and Allbritton, N. L. (2007). Surface graft polymerization of SU-8 for bio-MEMS applications. *Journal of Micromechanics and Microengineering*, 17(7):1371–1380.

Wiederhold, N. P. (2017). Antifungal resistance: current trends and future strategies to combat. *Infection and Drug Resistance*, 10:249–259. 28919789[pmid].

Willaert, R. G., Boer, P. V., Malovichko, A., Alioscha-Perez, M., Radotić, K., Bartolić, D., Kalauzi, A., Villalba, M. I., Sanglard, D., Dietler, G., Sahli, H., and Kasas, S. (2020). Single yeast cell nanomotions correlate with cellular activity. *Science Advances*, 6(26):eaba3139.

Wouters, K., Gijsenbergh, P., and Puers, R. (2011). Comparison of methods for the mechanical characterization of polymers for MEMS applications. *Journal of Micromechanics and Microengineering*, 21(11):115027.

Xu, T., Bachman, M., Zeng, F.-G., and Li, G.-P. (2004). Polymeric micro-cantilever array for auditory front-end processing. *Sensors and Actuators A: Physical*, 114(2):176–182. Selected papers from Transducers 03.

Xu, T., Chang, R., Bachman, M., and Li, G. (2005). Optical polymer waveguide based cantilevers for chemical and biological sensors. In *2005 IEEE SENSORS, VOLS 1 AND 2*, IEEE Sensors, pages 963–966. IEEE Sensors Council. 4th IEEE Conference on Sensors, Irvine, CA, OCT 31-NOV 03, 2005.

Xue, P., Bao, J., Chuah, Y. J., Menon, N. V., Zhang, Y., and Kang, Y. (2014). Protein covalently conjugated su-8 surface for the enhancement of mesenchymal stem cell adhesion and proliferation. *Langmuir*, 30(11):3110–3117.

Ying, Z. C., Reitsma, M. G., and Gates, R. S. (2007). Direct measurement of cantilever spring constants and correction for cantilever irregularities using an instrumented indenter. *Review of Scientific Instruments*, 78(6):063708.

Zinoviev, K., Dominguez, C., Plaza, J. A., Busto, V. J. C., and Lechuga, L. M. (2006a). A novel optical waveguide microcantilever sensor for the detection of nanomechanical forces. *Journal of Lightwave Technology*, 24(5):2132–2138.

Zinoviev, K., Dominguez, C., Plaza, J. A., Cadarso, V., and Lechuga, L. M. (2006b). Light coupling into an optical microcantilever by an embedded diffraction grating. *Appl. Opt.*, 45(2):229–234.

Zinoviev, K., Plaza, J. A., Cadarso, V., Dominguez, C., and Lechuga, L. M. (2007). Optical biosensor based on arrays of waveguide microcantilevers. In Kubby, JA and Reed, GT, editor, *Silicon Photonics II*, volume 6477 of *Proceedings of SPIE*. Conference on Silicon Photonics II, San Jose, CA, JAN 22-25, 2007.

Zinoviev, K., Plaza, J. A., Cadarso, V., Lechuga, L. M., and Dominguez, C. (2006c). Butt coupled microcantilever in sensing applications - art. no. 618607. In Urey, H and ElFatatry, A, editor, *MEMS, MOEMS, and Micromachining II*, volume 6186 of *Proceedings of the Society Of Photo-Optical Instrumentation Engineers (SPIE)*, page 18607. SPIE; Conseil Gen Bas Rhin; Communaute Urbaine Strasbourg; Reg Alsace; Alsace Dev Agcy. Conference on MEMS, MOEMS and Micromachining II, Strasbourg, FRANCE, APR 03-04, 2005.

Anton Malovichko

anton.malovichko@epfl.ch

Key skills: Microfabrication, micromechanical and electrical characterization techniques, data processing and scripting, CAD

Education

2017 – 2021 **PhD student, Microsystems and Microelectronics** • *EPFL, Switzerland*

2016 **M. Sc, Nanobiophysics** • *Biotechnology Center of the TU Dresden, Germany*

2015 **M. Sc., Electronics and Nanoelectronics** • *National Research University of Electronic Technology (MIET), Russia*

2013 **B. Sc., Nanotechnology** • *National Research University of Electronic Technology (MIET), Russia*

Professional Experience

June 2017 – October 2021

EPFL, Lausanne • Assistant-Doctorant (PhD student)

Microfabricated nanomotion detectors for ultra-rapid bacterial sensitivity tests

- Design and microfabrication of microfluidic chips for live cells imaging
- Finite element analysis of mechanical behaviour of the cantilever beams
- Design and microfabrication of the lightguide-like nanomechanical oscillators
- Assembling optical measuring setup
- Writing image analysis and signal processing scripts for precise detection of the cantilever deflection
- Conducting optomechanical measurements and characterization of the fabricated devices

Technologies: UV mask-less and mask lithography, dry and wet etching, Python scripting (numpy, pandas, seaborn, scikit-image), design of the lithography layouts and mechanical CAD, 3D printing, finite elements analysis

May 2016 – January 2017

Nanomaterial - Based Biosensors group, BioMed X, Heidelberg • Master Student

Fabrication and characterization of (nano)biosensors for blood gas analytics

- Performed I-V curves characterization of the liquid - gated field-effect transistors in the microfluidic system
- Developed platform for measuring sensor devices
- Wrote scripts for some automation of the I-V (current-voltage) curves data analysis

Technologies: Python, passive printed circuit design, I-V curves characterization, microfluidics

www.linkedin.com/in/anton-malovichko

July 2014 - August 2014

Walter Schottky Institute (Summer Research School NIM), Munich • Intern Student

• Surface functionalization of the polycrystalline diamond substrates by self-assembled monolayers (SAM), atomic force microscopy (AFM) and electrochemical (cyclic voltammetry) characterization of the samples

February 2012 – June 2014

Center "Probe Microscopy and Nanotechnology", Moscow • Research Assistant

• Operated Atomic Force Microscope, performed I-V curves measurement, micro-Raman mapping.

• Developed carbon nanotube - based gas sensors

• Taught lab course.

Technical Skills

Microfabrication	UV mask and mask-less lithography, dry and wet etching, thin films
Programming	Python (numpy, scipy, scikit-image, matplotlib, bokeh, seaborn), MATLAB, Labview; git
Engineering	Mechanical CAD (AutoCAD, Designspark Mechanical), lithography layout design (KLayout), finite elements simulations (COMSOL), 3D printing
Measurements	Field-effect transistors I-V characterization, atomic force microscopy, electrochemical measurements (cyclic voltammetry, squarewave voltammetry), scanning interferometry

Languages

English	Full working proficiency (fluent)
German	Limited working proficiency (B2)
French	Basic communication skills (A2)
Russian	Mother tongue

Interests

Engineering	Arduino prototyping
Sports	Indoor climbing, skiing, cross-country skiing
Travelling	Hiking, cycling
Other	Guitar (acoustic), Language exchange (participation in multi-lingual 'language cafe' events)

Personal information

Date of birth	27.03.1992
Marital status	Single
Nationality	Russian, Swiss permit B since 2017
Driving license	Category B, A1

www.linkedin.com/in/anton-malovichko